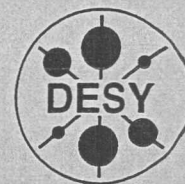


DEUTSCHES ELEKTRONEN-SYNCHROTRON
in der HELMHOLTZ-GEMEINSCHAFT



DESY-THESIS-2002-051
December 2002

Search for a Higgs Boson
in the Two Photon Decay Mode
in e^+e^- Collisions at LEP

by

DESY-Bibliothek

A. Rosca

ISSN 1435-8085

NOTKESTRASSE 85 - 22607 HAMBURG

DESY behält sich alle Rechte für den Fall der Schutzrechtserteilung und für die wirtschaftliche Verwertung der in diesem Bericht enthaltenen Informationen vor.

DESY reserves all rights for commercial use of information included in this report, especially in case of filing application for or grant of patents.

To be sure that your reports and preprints are promptly included in the
HEP literature database
send them to (if possible by air mail):

DESY
Zentralbibliothek
Notkestraße 85
22603 Hamburg
Germany

DESY
Bibliothek
Platanenallee 6
15738 Zeuthen
Germany

Search for a Higgs Boson in the Two Photon Decay
Mode in e^+e^- Collisions at LEP

D I S S E R T A T I O N

zur Erlangung des akademischen Grades
doctor rerum naturalium
(Dr. rer. nat.)
im Fach Physik

eingereicht an der
Mathematisch-Naturwissenschaftlichen Fakultät I
Humboldt-Universität zu Berlin

von
Dipl.-Phys. Aura Rosca
geboren am 6.8.1967 in Bukarest

Präsident der Humboldt-Universität zu Berlin:

Prof. Dr. Jürgen Mlynek

Dekan der Mathematisch-Naturwissenschaftlichen Fakultät I:

Prof. Dr. Michael Linscheid

Gutachter:

1. Prof. Dr. T. Hebbeker
2. Prof. Dr. H. Kolanoski
3. Dr. M. Felcini

Tag der mündlichen Prüfung: 12.07.2002

Zusammenfassung

Im Standardmodell der Elementarteilchen erhalten die W und Z Eichbosonen ihre Masse durch die spontane Brechung der Symmetrie durch ein komplexes skalares Feld. Die anderen Teilchen wechselwirken ebenfalls mit diesem Feld und erhalten Masse proportional zur Stärke der Wechselwirkung. Dieses Modell erfordert die Existenz eines skalaren Teilchens, genannt Higgs Boson, dessen Masse nicht vorhergesagt wird.

Die Higgs Kopplungen an die Eichbosonen und die Quarks und Leptonen werden jedoch im Standard Modell vorhergesagt und wir erwarten, daß das Higgs Teilchen mit kleiner Masse hauptsächlich in b-Quarks zerfällt. Da das Higgs Boson neutral ist und in erster Näherung nicht an Photonen koppelt ist das vom Standard Modell vorhergesagte Verzweungsverhältnis $BR(h \rightarrow \gamma\gamma)$ klein.

In Erweiterungen zum Standard Modell wird ein sogenanntes fermiophobisches Higgs Boson vorhergesagt, dessen Kopplungen zu allen Fermionen unterdrückt sind. Solch ein Teilchen wird für Massen unter etwa 90 GeV hauptsächlich in ein Photonenpaar zerfallen.

Diese Arbeit enthält die Ergebnisse der Suche des Zerfalls eines Higgs Bosons im Zerfallsmodus $h \rightarrow \gamma\gamma$. Die analysierten Daten wurden in e^+e^- Kollisionen mit der Schwerpunktsenergie zwischen 189 GeV und 209 GeV am Large Electron Positron Collider (LEP) aufgenommen. Die Größe des Datensatzes entspricht einer Luminosität von etwa 600 pb^{-1} .

Der Hauptproduktionsmechanismus des Higgs Bosons ist bei diesen Energien die assoziierte Produktion mit einem Z Boson, der $e^+e^- \rightarrow hZ$ Prozess. Alle möglichen Zerfallsmoden des Z Bosons wurden untersucht. Dies führt zu den Endzuständen $q\bar{q}\gamma\gamma$, $\nu\bar{\nu}\gamma\gamma$ und $\ell^+\ell^-\gamma\gamma$, mit $\ell = e, \mu, \tau$.

Keine Evidenz für den Zerfall des Higgs in zwei Photonen wurde beobachtet. Das negative Suchresultat wurde in obere Grenzen für das Verzweungsverhältnis des Higgs Zerfalls in zwei Photonen übersetzt. Die ausgeschlossenen Higgs Massenwerte werden als Funktion des $h \rightarrow \gamma\gamma$ Verzweungsverhältnisses für den Fall des fermiophobischen Higgs präsentiert. Die erhaltene Grenze für die fermiophobische Higgs Masse ist 105.4 GeV mit 95 % Konfidenz, die Monte-Carlo Simulation ergab 105.3 GeV. Dieses Ergebnis steht als die endgültige Massengrenze die bei LEP mit dem L3 Experiment erreichbar war.

Abstract

In the Standard Model of particle physics the mass generation of the W and Z gauge bosons is achieved through the spontaneous symmetry breaking of the gauge symmetry by a complex scalar field. The other particles also interact with this field and acquire mass proportional to the strength of the interaction. This model requires the existence of a scalar particle called the Higgs boson, whose mass is not predicted.

The Higgs couplings to the gauge bosons, quarks and leptons are predicted in the Standard Model and we expect that the Higgs boson will decay mostly to b-quarks for low masses. Since the Higgs boson is neutral and does not couple to photons at tree level, the branching fraction $BR(h \rightarrow \gamma\gamma)$ is predicted to be small in the Standard Model.

Extensions of the Standard Model predict a so-called fermiophobic Higgs boson whose couplings to all fermions are suppressed. Such a particle will decay predominantly into a photon pair for masses below 90 GeV.

This thesis presents the results of the search for a Higgs boson in the two photon decay mode. The data were obtained in e^+e^- interactions at centre-of-mass energies between 189 GeV to 209 GeV, at the Large Electron Positron (LEP) collider. A data set corresponding to a total integrated luminosity of about 600 pb^{-1} was analysed.

The main production mechanism of the Higgs boson at these energies is the associated production with the Z boson, the $e^+e^- \rightarrow hZ$ process. All the possible Z decay modes have been considered. This gives rise to $q\bar{q}\gamma\gamma$, $\nu\bar{\nu}\gamma\gamma$ and $\ell^+\ell^-\gamma\gamma$, with $\ell = e, \mu, \tau$, final states.

No evidence of the production of a Higgs particle decaying into two photons was observed in the analysed sample. The negative search result is translated into upper limits on the branching fraction for the Higgs boson decay to two photons. The excluded Higgs mass values as a function of the $h \rightarrow \gamma\gamma$ branching fraction are presented for the case of a fermiophobic Higgs boson. The reach in the fermiophobic Higgs mass is of 105.4 GeV at 95% confidence level, while a limit of 105.3 GeV was expected from Monte Carlo simulations of the experiment performance. This result stands as the final mass limit which could be obtained at the LEP collider with the L3 detector.

Contents

| | | |
|----------|--|-----------|
| 1 | Introduction | 3 |
| 2 | Theoretical overview | 7 |
| 2.1 | Fermi theory | 7 |
| 2.2 | Weak isospin and hypercharge | 9 |
| 2.3 | Yang-Mills theories | 11 |
| 2.4 | Higgs mechanism | 12 |
| 2.5 | Boundaries on the Higgs mass | 17 |
| 2.5.1 | Theoretical bounds | 17 |
| 2.5.2 | Unitarity constraints on the Higgs mass | 18 |
| 2.5.3 | Limits from indirect searches | 20 |
| 2.5.4 | Limits from direct searches | 24 |
| 2.6 | Extended Higgs models | 25 |
| 2.6.1 | Two Higgs Doublet Model (2HDM) | 26 |
| 2.6.2 | Bounds in Two-Doublet Models | 28 |
| 2.7 | Higgs boson decay | 29 |
| 2.7.1 | Decays of the Standard Model Higgs boson | 29 |
| 2.7.2 | Decays of fermiophobic Higgs bosons | 31 |
| 2.7.3 | Higgs decaying into two photons | 33 |
| 3 | Physics at electron-positron colliders | 39 |
| 3.1 | Standard Model processes | 39 |
| 3.1.1 | The two-fermion process | 41 |
| 3.1.2 | The two-photon process | 43 |
| 3.1.3 | The four-fermion processes | 43 |
| 3.2 | Higgs boson physics | 45 |
| 3.2.1 | Higgs boson production | 45 |
| 4 | The Experiment | 49 |
| 4.1 | The Large Electron Positron collider | 52 |

| | | |
|----------|---|------------|
| 4.1.1 | Centre-of-mass energy measurement | 53 |
| 4.1.2 | Luminosity measurement | 54 |
| 4.2 | The L3 Detector | 55 |
| 4.2.1 | The central tracking system | 57 |
| 4.2.2 | The electromagnetic calorimeter | 60 |
| 4.2.3 | EGAP | 62 |
| 4.2.4 | The Luminosity Monitor | 63 |
| 4.2.5 | The Hadron Calorimeter and the Muon Filter | 63 |
| 4.2.6 | The scintillator system | 65 |
| 4.2.7 | Muon spectrometer | 65 |
| 4.2.8 | The magnet | 66 |
| 4.3 | The L3 data acquisition system | 67 |
| 4.3.1 | Level-1 Trigger | 67 |
| 4.3.2 | Level-2 Trigger | 68 |
| 4.3.3 | Level-3 Trigger | 69 |
| 4.4 | The L3 offline software | 69 |
| 4.4.1 | Simulation; Monte Carlo generators | 69 |
| 4.4.2 | Reconstruction | 70 |
| 4.4.3 | Particle identification | 75 |
| 5 | Search for Higgs Boson decay into two photons | 79 |
| 5.1 | Photon pair selection | 80 |
| 5.2 | The $q\bar{q}\gamma\gamma$ final state | 81 |
| 5.3 | The $\nu\bar{\nu}\gamma\gamma$ final state | 84 |
| 5.4 | The $\ell^+\ell^-\gamma\gamma$ final state | 86 |
| 5.5 | Summary of the event selection | 88 |
| 5.6 | Systematic uncertainties | 89 |
| 6 | Results | 91 |
| 6.1 | Interpretation | 91 |
| 6.1.1 | Bayesian approach | 92 |
| 6.1.2 | Frequentistic approach | 93 |
| 6.2 | Results | 95 |
| 6.3 | Results of the $h \rightarrow WW^*$ channel and combination with $h \rightarrow \gamma\gamma$ | 99 |
| 7 | Outlook | 103 |
| 7.1 | ALEPH, DELPHI and OPAL | 103 |
| 7.1.1 | Other searches by DELPHI | 105 |
| 7.2 | The Tevatron at Fermilab | 106 |

| | | |
|----------|--|------------|
| 7.3 | The Large Hadron Collider at CERN | 108 |
| 8 | Conclusions | 109 |
| A | Summary of the selection cuts | 111 |
| B | Results at the centre-of-mass energy of $\sqrt{s} = 189$ GeV | 116 |
| C | Linear interpolation of histograms | 119 |
| D | Background smoothing | 121 |

List of Figures

| | | |
|------|---|----|
| 2.1 | The four-fermion Fermi interaction. | 8 |
| 2.2 | Scalar potential for $\mu^2 > 0$ | 14 |
| 2.3 | Bounds on the Standard Model Higgs boson mass. | 18 |
| 2.4 | Leading order diagrams for the WW scattering. | 19 |
| 2.5 | Leading order diagrams for the WW scattering. | 19 |
| 2.6 | Precision electroweak measurements. | 21 |
| 2.7 | The $\delta\chi^2 = \chi^2 - \chi_{\min}^2$ versus m_h | 23 |
| 2.8 | Negative log-likelihood ratio as a function of the Higgs mass. | 25 |
| 2.9 | The dominant Higgs decay mode at LEP2. | 29 |
| 2.10 | Feynman diagram for the Higgs decay into a WW pair. | 30 |
| 2.11 | Possibilities for the two photon Higgs decay. | 30 |
| 2.12 | The branching fractions of the Standard Model Higgs boson and total decay width. | 31 |
| 2.13 | The fermiophobic Higgs decay into a fermion pair. | 32 |
| 2.14 | Possibilities for a fermiophobic Higgs decay. | 32 |
| 2.15 | Branching fractions of the Standard Model Higgs boson calculated with the HDECAY program. | 33 |
| 2.16 | Branching fractions for the decay of the Higgs boson in the benchmark fermiophobic model. | 37 |
| 3.1 | Cross sections for typical standard model processes. | 40 |
| 3.2 | Diagrams contributing to the $e^+e^- \rightarrow f\bar{f}$ process. | 42 |
| 3.3 | Diagrams contributing to the $e^+e^- \rightarrow e^+e^-$ process. | 42 |
| 3.4 | Diagram contributing to the $e^+e^- \rightarrow \nu\bar{\nu}(\gamma)$ process. | 43 |
| 3.5 | Diagram contributing to the two-photon process. | 43 |
| 3.6 | Diagrams contributing to the W^+W^- process. | 44 |
| 3.7 | Diagram contributing to the ZZ process. | 44 |
| 3.8 | Diagrams contributing to the $We\nu$ process. | 44 |
| 3.9 | Diagram contributing to the Zee process. | 45 |
| 3.10 | Higgs-Strahlung. | 45 |

| | | |
|------|--|----|
| 3.11 | WW and ZZ fusion diagrams. | 46 |
| 3.12 | Higgs production cross section. | 46 |
| 3.13 | Associated pair production in the 2HDM. | 47 |
| 3.14 | Associated charged Higgs production in the 2HDM. | 48 |
| 3.15 | Production cross section for charged Higgs bosons. | 48 |
| 4.1 | LEP aerial view. | 49 |
| 4.2 | Integrated luminosity per day achieved by the LEP machine in 2000, as a function of time. | 51 |
| 4.3 | A superconducting RF cavity. | 52 |
| 4.4 | The LEP injection and acceleration chain. | 53 |
| 4.5 | The L3 Detector. | 56 |
| 4.6 | The L3 support tube. | 56 |
| 4.7 | Schematic of an ionizing particle traversing an SMD wafer. | 57 |
| 4.8 | Drawing of the wire positions in a TEC sector. | 59 |
| 4.9 | Amplification and drift regions in the TEC. | 59 |
| 4.10 | The crystal layout of the BGO electromagnetic calorimeter. | 61 |
| 4.11 | Energy resolution of the BGO. | 62 |
| 4.12 | Longitudinal view of the EGAP detector. | 63 |
| 4.13 | The hadron calorimeter. | 64 |
| 4.14 | The muon spectrometer. | 66 |
| 4.15 | Σ_1 , Σ_9 and Σ_{25} | 72 |
| 4.16 | Example of a candidate event. | 74 |
| 4.17 | Schematic view of a reconstructed electron. | 75 |
| 4.18 | Distributions of photon identification variables. | 76 |
| 4.19 | Schematic view of a reconstructed muon. | 77 |
| 4.20 | Schematic view of a $e^+e^- \rightarrow \tau\nu\tau\nu$ event. | 78 |
| 5.1 | Distribution of the polar angle of the most energetic photon. | 80 |
| 5.2 | Candidate event for $e^+e^- \rightarrow q\bar{q}\gamma\gamma$ process. | 81 |
| 5.3 | Distribution for the $q\bar{q}\gamma\gamma$ final state of the normalized visible energy. | 82 |
| 5.4 | Distributions for the $q\bar{q}\gamma\gamma$ final state. | 83 |
| 5.5 | Candidate event for $e^+e^- \rightarrow \nu\bar{\nu}\gamma\gamma$ process. | 84 |
| 5.6 | Distribution for the $\nu\bar{\nu}\gamma\gamma$ final state of the acoplanarity. | 85 |
| 5.7 | Distribution for the $\nu\bar{\nu}\gamma\gamma$ final state of the recoil mass. | 85 |
| 5.8 | Candidate events for the $e^+e^-\gamma\gamma$, $\mu^+\mu^-\gamma\gamma$, $\tau^+\tau^-\gamma\gamma$ processes. | 86 |
| 5.9 | Distributions for the $\ell^+\ell^-\gamma\gamma$ final state. | 87 |
| 6.1 | Probability density function of $-2\ln Q$ | 94 |

| | | |
|-----|--|-----|
| 6.2 | The reconstructed di-photon invariant mass. | 96 |
| 6.3 | The 95% confidence level upper limit on the di-photon branching fraction. | 98 |
| 6.4 | Distribution of $1-CL_b$ for all L3 data in the $h\gamma\gamma$ search. | 99 |
| 6.5 | 95% CL upper limits on the branching fraction $BR(h \rightarrow WW^*)$ | 100 |
| 7.1 | The distribution of the di-photon invariant mass. | 104 |
| 7.2 | 95% confidence level excluded region in the (m_h, m_A) plane. | 105 |
| 7.3 | The main production mechanism of a fermiophobic Higgs at the Tevatron. | 106 |
| 7.4 | D0 results on the fermiophobic Higgs search. | 107 |
| 7.5 | The expected Run II limits on the branching fraction $h \rightarrow \gamma\gamma$ as a function of the Higgs mass. | 108 |
| B.1 | Distribution of the reconstructed di-photon invariant mass. | 118 |
| B.2 | Excluded values of the $BR(h \rightarrow \gamma\gamma)$ | 118 |
| C.1 | Example of histogram interpolation. | 120 |
| D.1 | The performance of the smoothing program on the reconstructed Higgs mass distribution. | 121 |
| D.2 | The standard output of the KEYS program. | 122 |

List of Tables

| | | |
|-----|--|-----|
| 2.1 | The fundamental fermions of the Standard Model. | 10 |
| 3.1 | Monte Carlo event generators for e^+e^- physics. | 41 |
| 4.1 | The centre-of-mass energies and corresponding integrated luminosities by the L3 detector. | 51 |
| 5.1 | Number of events observed in data, by the $q\bar{q}\gamma\gamma$ selection, N_{Data} , compared with the Standard Model expectations, N_{Bkgd} | 83 |
| 5.2 | Number of events observed in data, by the $\ell^+\ell^-\gamma\gamma$ selection, N_{Data} , compared with the Standard Model expectations, N_{Bkgd} | 88 |
| 5.3 | Number of events observed in data, N_{Data} , compared with the Standard Model expectations, N_{Bkgd} | 88 |
| 7.1 | The observed and expected mass limits for a fermiophobic Higgs boson. | 104 |
| A.1 | Selection cuts used in the analysis. | 111 |
| A.2 | Selection cuts used in the analysis. | 112 |
| A.3 | Selection cuts used in the analysis. | 113 |
| A.4 | Selection cuts used in the analysis. | 114 |
| A.5 | Selection cuts used in the analysis. | 115 |
| B.1 | Number of events expected from Standard Model processes compared to the data events, for the $q\bar{q}\gamma\gamma$ final state. | 117 |
| B.2 | Number of events expected from the Standard Model process $e^+e^- \rightarrow \nu\bar{\nu}(\gamma)$ compared to the data events. | 117 |
| B.3 | Number of events expected from Standard Model processes compared to the data events, for the $\ell^+\ell^-\gamma\gamma$ final state. | 117 |

Chapter 1

Introduction

The discovery of the electron by J. J. Thomson, in the year 1897, can be considered as the beginning of particle physics. Many experimental and conceptual successes have been achieved since then. Our current understanding of the subject is summarized in the so-called Standard Model, which has been tested with high precision at particle physics laboratories around the world. Up to now there is no confirmed result from any experiment that contradicts the Standard Model.

The fundamental particle interactions described by the Standard Model are the electromagnetic, weak and strong nuclear forces. The electromagnetic forces between one charged particle and another are mediated by the exchange of massless photons. Electromagnetic interactions are well described by the quantum theory of electrodynamics, called QED. Meanwhile the strong nuclear interactions are described by Quantum Chromo Dynamics (QCD), and are mediated by massless bosons, called gluons. These were discovered at the DESY laboratory in Germany in 1979.

According to the unified theory of the weak and electromagnetic interactions - developed by Glashow, Weinberg and Salam in the 1960s - weak nuclear interactions such as beta decay should similarly be mediated by the exchange of charged (W^+ and W^-) and neutral (Z) massive intermediate bosons. These were discovered at CERN, the European laboratory for particle physics near Geneva in Switzerland, in 1983. Their mass is about 80 and 91 GeV, respectively. Thus all the fundamental interactions have very similar structures, but the question why only the weak bosons are massive remains open.

As already mentioned, the first elementary matter particle to be identified was the electron, which weighs about 0.5 MeV and has an intrinsic spin of one half. This was followed by the discoveries of other particles, called leptons, which do not feel the strong nuclear interactions: the unstable muon in 1936 (weighing about 100 MeV) and the tau lepton in 1975 (about 1.8 GeV). Each of these three charged leptons has its own associated uncharged neutrino, and experiments at the Large Electron Positron (LEP)

accelerator at CERN have shown that there are no more similar neutrinos. New data have also established upper limits on the possible masses of the neutrinos, which are much less than those of the corresponding charged leptons.

The strongly interacting particles, known as hadrons, that have been discovered since the 1940s are known to be composite bound states of more elementary entities called quarks. We now know that there are six different types of quarks, and that their masses range from a few MeV, for the up and down quarks that make up the conventional nuclear matter, to about 5 GeV for the bottom quark discovered in 1977. The top quark, which was discovered in 1994 in proton-antiproton collisions at Fermilab near Chicago, weighs around 174 GeV.

Although the strong nuclear forces are - as their name suggests - strong, it is known that they get weaker at high energies, which corresponds to short distances. This property of "asymptotic freedom" is a central prediction of QCD. Like the other elementary particle interactions, QCD is what we call a "gauge theory". Most particle theories have symmetries under which the properties of a particle, such as its charge and spatial coordinates, can be changed without altering the predictions of the theory. The special feature of a gauge theory is that these transformations can be made independently at each point in space and time. This is possible if the exchange particles that mediate the interactions have integer spin: in other words, if they are vector bosons. In QED, the prototype gauge theory, the photon has a spin of 1. Gauge theories provide the only consistent description of the interactions of such particles.

Particle physics has been dominated in recent years by a series of precision tests of the Standard Model, including both its strong and electroweak sectors. The asymptotic freedom of the strong interactions has been confirmed in a large number of experiments. Tests of the electroweak sector have been dominated by high energy collisions between electrons and positrons at LEP and at the Stanford Linear Collider (SLC) in California.

For the first few years of its operation, the beams at LEP were tuned such that their energies corresponded to the mass of the Z particle. At these specific energies, the rate at which the electron-positron interactions occur is enhanced, and a graph of the interaction rate versus energy shows a "resonance peak". The height and the width of the peak depend on the number of modes in which the short-lived Z particles decay. It also includes decay modes that cannot be detected directly, such as those into a pair of neutrinos. The LEP measurements tell us that there are precisely three neutrino species.

In addition to measuring the total interaction rates, LEP and the SLC have provided many other precision measurements, including the relative probabilities for the Z particle to decay into different heavy quarks, the angular distributions for particle production, and their dependencies on the particle spins.

Many of these measurements are accurate to the permille level, and none differs significantly from the Standard Model predictions. These predictions require calculations of the small quantum corrections due to virtual particles that are emitted by a particle and exist briefly before being re-absorbed. These corrections can be calculated reliably within the electroweak theory. In many quantum theories, these corrections are infinite, and it is not possible to make reliable predictions. It is one of the successes of gauge theories that these infinities can be removed, allowing finite predictions for physical quantities to be made. This was first done for QED in the 1940s. In the early 1970s 't Hooft and Veltman proved that it could also be done for the electroweak theory - an achievement for which the 1999 Nobel Prize for Physics has been awarded.

These so-called loop-calculations are sensitive to the masses of virtual particles, including those which are too heavy to be produced directly at LEP or the SLC. In particular, the various measurements from the Z decays are quite sensitive to the mass of the top quark. Particle physicists were therefore able to successfully predict the mass of the top quark before it was discovered, by confronting the Standard Model with all the measurements and determining which mass fitted best.

In its last years of operation, LEP beam energies have been raised well above the threshold for Z production such that pairs of W bosons could be created and studied in detail. According to the Standard Model, the W pairs can be produced if the electron and positron first create a photon or Z boson, or exchange a neutrino. All three contributions are required to explain the LEP data, and the measurements are in good agreement with the theoretical predictions.

There are still some key features of the theory that have not yet been tested. One of these is the origin of the particle masses. According to the Standard Model, the underlying field theory can be formulated in terms of massless particles, in a very symmetric way. However, the electroweak vacuum is believed to break this symmetry, and give different masses to different particles. The reason for this spontaneous symmetry breakdown is believed to be a scalar field, which has an associated particle called the Higgs boson. The precision electroweak data described earlier are sensitive to the mass of this particle, and currently indicate that it weighs between 115 GeV and 300 GeV.

The search for the Higgs boson has been one of the continuing objectives of the LEP experimental programme. This thesis describes the search for the Higgs boson through its decay into two photons. The structure of the work is as follows. In the beginning a short overview of the Standard Model concepts is given, and the Higgs mechanism by which the fundamental particles obtain their masses is introduced. The experimental environment, the LEP collider and the L3 detector are then presented. The following chapters describe the analysis procedure and the results obtained. More technical information can be found in the Appendices.

Chapter 2

Theoretical overview

The Standard Model is our current theory for the quantitative description of all interactions of fundamental particles except gravity. Up to now it is extremely successful: all measurements are in agreement with the Standard Model predictions.

The Standard Model is a renormalizable relativistic quantum field theory based on non-Abelian gauge symmetry [1] of the gauge group $SU(3)_C \times SU(2)_L \times U(1)_Y$. It has two sectors: Quantum Chromo Dynamics (QCD) and the Electroweak Theory. QCD is a vector gauge theory which describes the $SU(3)_C$ color interactions of quarks and gluons. The Electroweak Theory describes the electromagnetic and weak interactions of the quarks and leptons as a chiral non-Abelian isospin and an Abelian hypercharge gauge symmetry $SU(2)_L \times U(1)_Y$. The gauge bosons W^\pm and Z become massive as a result of the Higgs mechanism, while the photon remains massless. The true dynamics behind the Higgs mechanism is not yet known. The simple one doublet Higgs sector predicts the existence of a single Higgs boson with well defined properties and its experimental search has high priority.

2.1 Fermi theory

The theory of weak interactions began in 1933 with Fermi's theory of the process $n \rightarrow pe^- \bar{\nu}_e$, the β -decay of the neutron (he also suggested the name neutrino for the hypothetical particle invented by Pauli in 1930 to explain the continuous energy spectrum of the electrons in beta decay). Weak interactions were treated as pointlike interactions between four fermions, as shown in Figure 2.1.

The Fermi theory of weak interactions describes processes when electrons, neutrinos and atomic nuclei are created and annihilated. Fermi's original interaction involves two interacting vector currents in analogy with the electromagnetic interaction describing electron-electron scattering. The discovery of parity violation in 1957 [2] led to the proposal that the Lagrangian of weak interactions, for β -decay, is given by the products

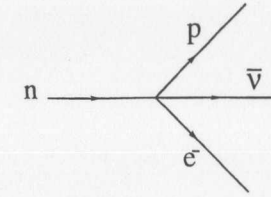


Figure 2.1: The four-fermion Fermi interaction.

of vector-axial vector (V-A) currents

$$\mathcal{L}_F(x) = \frac{G_F}{\sqrt{2}} (\bar{p}(x) \gamma^\alpha (g_V - g_A \gamma_5) n(x)) (\bar{e}(x) \gamma_\alpha (1 - \gamma_5) \nu(x)). \quad (2.1)$$

where the vector coupling, g_V , of the nucleon is slightly smaller than one and is given by the Cabbibo angle, $g_V = \cos \theta_C \approx 0.97$. Here x is a space-time coordinate, γ_α are the Dirac matrices and g_A is the axial-vector coupling.

The ratio of the axial to vector couplings of the nucleon is known from the study of beta-decay with total angular momentum transitions of $\Delta J=0$ and 1 resulting in $g_A/g_V = -1.2573 \pm 0.0028$ [3]. This Lagrangian can be used to calculate the neutron lifetime in leading order of perturbation theory in terms of the Fermi coupling constant G_F . From the experimental value of the neutron lifetime $\tau = 887.0 \pm 2.0$ s one obtains a first estimate of the value of the Fermi constant $G_F \approx (250 \text{ GeV})^{-2} = 1.6 \times 10^{-5} \text{ GeV}^{-2}$.

With the discoveries of the pion π , the muon μ and the strange hadrons the V-A structure of weak interactions has been established in a variety of experiments. Further progress has been made with the discovery that the electron and muon numbers are separately conserved and that the neutrinos associated with the muons are new particles. The data have indicated that the strength and form of the four fermion interactions between fermionic doublets (p,n) , (e,ν_e) , (μ,ν_μ) is universal. In particular the muon decay can be described by a Lagrangian written as

$$\mathcal{L}_\mu(x) = \frac{G_F}{\sqrt{2}} \bar{\nu}_\mu(x) \gamma^\alpha (1 - \gamma_5) \mu(x) \bar{e}(x) \gamma_\alpha (1 - \gamma_5) \nu_e(x).$$

The photonic corrections to this transition are finite in all orders of perturbation theory [4]. The leading corrections have been calculated 20 years ago [5] whereas the $\mathcal{O}(\frac{\alpha}{\pi})^2$ term has been obtained by van Ritbergen and Stuart only very recently [6]. The muon lifetime is thus given by the theoretical expression

$$\frac{1}{\tau_\mu} = \frac{G_F^2 m_\mu^5}{192 \pi^3} \left(1 - \frac{8m_e^2}{m_\mu^2}\right) \left[1 + 1.810 \left(\frac{\alpha}{\pi}\right) + (6.701 \pm 0.002) \left(\frac{\alpha}{\pi}\right)^2 + \dots\right].$$

This equation offers a convenient definition of the Fermi-coupling G_F by assuming that the non-photon corrections are all lumped into G_F in a way that it can be considered a physical quantity. Using the measured value of τ_μ [3] we obtain:

$$G_F = (1.16637 \pm 0.00001) \times 10^{-5} \text{ GeV}^{-2}.$$

The old Fermi theory for the weak interaction is not a renormalizable theory; its validity was limited to tree level calculations at $\sqrt{s} \ll M_W$. For a renormalizable theory, a finite number of measurements will fix the finite number of parameters, leaving us with a theory capable of predicting all further measurements. A nonrenormalizable theory has an infinite number of parameters appearing in the full quantum theory, and therefore has no predictive power beyond tree graphs.

2.2 Weak isospin and hypercharge

We know today that the interaction in Eq. (2.1) is mediated by the exchange of a W boson. The exchange of a W boson, at negligible momenta with respect to its mass, M_W , gives rise to a four-fermion interaction of the form of Eq. (2.1):

$$\mathcal{L}_I = -\frac{g}{2\sqrt{2}} W_\alpha^- J^{+\alpha} + h.c. \quad (2.2)$$

$$J_\alpha^+ = [\bar{\nu}_e(x)\gamma_\alpha(1 - \gamma_5)e(x) + \bar{p}(x)\gamma_\alpha(1 - \gamma_5)n(x)]$$

where $W^\pm = W^1 \pm iW^2$. We identify G_F with $\frac{g^2}{8M_W^2}$, and by requiring that the dimensionless coupling g does not exceed 1, we have an upper bound on the W mass of about 110 GeV, $M_W \leq 110 \text{ GeV}$.

The charged current can be considered as the charged component of the weak isospin. We can rewrite the charged current in Eq. (2.2) in the form

$$\frac{1}{2} J_\alpha^+ = \bar{N}_L(x)\gamma_\alpha T^+ N_L(x) + \bar{L}_L(x)\gamma_\alpha T^+ L_L(x)$$

where T^i are the $SU(2)$ generators, related with the Pauli spin matrices by $T^i = \sigma^i/2$, and we organized the left handed fermion fields in doublets (the charged current in Eq. (2.2) does not involve the right handed fermions):

$$N_L(x) = \mathcal{P} \begin{pmatrix} p(x) \\ n(x) \end{pmatrix}, \quad L_L(x) = \mathcal{P} \begin{pmatrix} \nu(x) \\ e(x) \end{pmatrix}, \quad \mathcal{P} = \frac{1}{2}(1 - \gamma_5).$$

The operators $T^\pm = T^1 \pm iT^2$ obey the commutation relation

$$[T^+, T^-] = 2T^3 \neq Q.$$

This defines the $SU(2)_L$ algebra, which includes apart from the charged generators T^\pm also a diagonal generator which is neutral. We know another diagonal generator, the

electrical charge Q . Q does not commute with T^\pm , but it can be written as a linear combination of T^3 and another neutral generator, the so-called hypercharge, Y :

$$Q = T^3 + Y$$

which commutes with all the T^i .

Since hadrons are made out of quarks, we have to replace the nucleons with the quarks. The $SU(2)_L \times U(1)_Y$ quantum numbers of left and right handed quarks and leptons are listed in Table (2.1). The spin one half matter fields form three quark-lepton families. Matter fields can be classified in terms of left handed Weyl-spinors.

| Name/Symbol | T_L^3 | $Y_L =$ | T_R^3 | $Y_R =$ | Q | Mass(GeV) | Year of Discovery |
|---------------------------|------------|----------------|----------------|-------------|----------------|--------------------------|-------------------|
| | | $Q - T_L^3$ | | $Q - T_R^3$ | | | |
| First family of fermions | | | | | | | |
| Electron Neutrino | ν_e | $\frac{1}{2}$ | $-\frac{1}{2}$ | 0 | 0 | $< 2.3 \cdot 10^{-9}$ | 1956 |
| Electron | e | $-\frac{1}{2}$ | $-\frac{1}{2}$ | 0 | -1 | $0.511 \cdot 10^{-3}$ | 1897 |
| Up quark | u | $\frac{1}{2}$ | $\frac{1}{6}$ | 0 | $\frac{2}{3}$ | $1 - 5 \cdot 10^{-3}$ | 1968 |
| Down quark | d | $-\frac{1}{2}$ | $\frac{1}{6}$ | 0 | $-\frac{1}{3}$ | $3 - 9 \cdot 10^{-3}$ | 1968 |
| Second family of fermions | | | | | | | |
| Muon Neutrino | ν_μ | $\frac{1}{2}$ | $-\frac{1}{2}$ | 0 | 0 | $< 0.19 \cdot 10^{-3}$ | 1962 |
| Muon | μ | $-\frac{1}{2}$ | $-\frac{1}{2}$ | 0 | -1 | 0.106 | 1937 |
| Charm quark | c | $\frac{1}{2}$ | $\frac{1}{6}$ | 0 | $\frac{2}{3}$ | 1.15 - 1.35 | 1974 |
| Strange quark | s | $-\frac{1}{2}$ | $\frac{1}{6}$ | 0 | $-\frac{1}{3}$ | $75 - 170 \cdot 10^{-3}$ | 1968 |
| Third family of fermions | | | | | | | |
| Tau Neutrino | ν_τ | $\frac{1}{2}$ | $-\frac{1}{2}$ | 0 | 0 | $< 18 \cdot 10^{-3}$ | 2000 |
| Tau | τ | $-\frac{1}{2}$ | $-\frac{1}{2}$ | 0 | -1 | 1.777 | 1975 |
| Top quark | t | $\frac{1}{2}$ | $\frac{1}{6}$ | 0 | $\frac{2}{3}$ | 174.3 ± 5.1 | 1994 |
| Bottom quark | b | $-\frac{1}{2}$ | $\frac{1}{6}$ | 0 | $-\frac{1}{3}$ | 4.0 ± 0.2 | 1977 |

Table 2.1: The fundamental fermions of the Standard Model. Most of the quark masses are from Ref. [7], where the determination of the masses for u,d,s,c,b quarks is discussed. For u,d,s the so-called current- or bare-quark masses are quoted.

The fundamental spin half particles can be grouped into a reducible multiplet of doublet fermions and singlet antifermions. One quark-lepton family is composed of

$$\Psi_L^f = (U_{cL}^f, D_{cL}^f, L_L^f, E_{cL}^f), \quad f = 1, 2, 3$$

with f being the family label. The corresponding Dirac spinors will be labeled as $\Psi_{f\chi}$ where χ runs over the values $\chi = U, D, E, N$ and

$$f_U = u, c, t, \quad f_D = d, s, b, \quad f_E = e, \mu, \tau, \quad \text{and} \quad f_N = \nu_e, \nu_\mu, \nu_\tau \quad (2.5)$$

where f_χ is the family label for a given component of the families.

2.3 Yang-Mills theories

The universality of the interactions, the weak isospin structure and the analogy with QED pointed to the Yang-Mills theory with a gauge group of $SU(2)_L \times U(1)_Y$ [8], [9]. The $SU(2)_L$ part is generated by the three components of the weak isospin, T^i , and the $U(1)_Y$ by the weak hypercharge Y . We call $W^{i,\mu}$ and B^μ the corresponding gauge bosons. In the case of the abelian gauge field B^μ associated with $U(1)_Y$, we define the field strength tensor $B^{\mu\nu}$ by

$$B^{\mu\nu} = \partial^\mu B^\nu - \partial^\nu B^\mu.$$

The field strength tensors for the three non-abelian gauge fields $W^{i,\mu}$ associated to $SU(2)_L$ are:

$$W^{i,\mu\nu} = \partial^\mu W^{i,\nu} - \partial^\nu W^{i,\mu} + g\epsilon_{ijk}W^{j,\mu}W^{k,\nu},$$

where ϵ_{ijk} is the Levi-Civita tensor.

The Lagrangian is given in terms of the two gauge coupling constants g and g'

$$\mathcal{L}_{ew} = -\frac{1}{4}W^{i,\mu\nu}W_{\mu\nu}^i - \frac{1}{4}B^{\mu\nu}B_{\mu\nu} + 2\sum_{f=1}^3\bar{\Psi}_L^f\gamma_\mu D^\mu\Psi_L^f,$$

where D^μ is the covariant derivative

$$D^\mu = \partial^\mu + igt^iW^{i,\mu} + ig'YB^\mu,$$

with t^i being the matrices representing the $SU(2)_L$ generators T^i on the fermion matter multiplets Ψ_L^f .

The neutral component of the W^i fields, W^3 , mixes with the abelian field B , to form the physical states

$$A_\mu = -\sin\theta_W W_\mu^3 + \cos\theta_W B_\mu, \\ Z_\mu = \cos\theta_W W_\mu^3 + \sin\theta_W B_\mu,$$

with

$$\tan\theta_W = \frac{g'}{g}, \quad e = g\sin\theta_W.$$

The interaction terms of the fermions are

$$\mathcal{L}_{I_f} = -\left(\frac{g}{2\sqrt{2}}J_\mu^+W^{-,\mu} + \frac{g}{2\sqrt{2}}J_\mu^-W^{+,\mu} + \frac{g}{2\cos\theta_W}J_\mu^{NC}Z_\mu + eJ_\mu^{\text{elm}}A^\mu\right)$$

with currents defined in terms of Dirac spinors

$$J_\mu^+ = \sum_{f_U, f_D} \bar{\Psi}_{f_U}\gamma_\mu(1-\gamma_5)V_{CKM}^{f_U f_D}\Psi_{f_D} + \sum_{f_E} \bar{\Psi}_{f_N}\gamma_\mu(1-\gamma_5)\Psi_{f_E}, \\ J_\mu^{NC} = \sum_{f_\chi} \bar{\Psi}_{f_\chi}\gamma_\mu(v_\chi - a_\chi\gamma_5)\Psi_{f_\chi}, \\ J_\mu^{\text{elm}} = \sum_{f_\chi} \bar{\Psi}_{f_\chi}\gamma_\mu Q_\chi\Psi_{f_\chi},$$

where the f_χ are the labels defined in Eq. (2.3), the color and spinor labels are suppressed and $V_{CKM}^{f_U f_D}$ is the Cabibbo-Kobayashi-Maskawa (CKM) matrix. The requirement of non-Abelian gauge symmetry leads to the universality of the gauge boson interactions and predicts the neutral current couplings

$$v_\chi = T_{\chi,L}^3 - 2Q_\chi\sin^2\theta_W, \quad a_\chi = T_{\chi,L}^3 \quad \chi = U, D, E, N.$$

The $SU(2)$ and gauge invariance of the Lagrangian (2.6) forbids mass terms both for the gauge bosons and the fermions. For fermions, the mass term would be $m\Psi\bar{\Psi} = m(\bar{\Psi}_L\Psi_R + \bar{\Psi}_R\Psi_L)$ which doesn't give an $SU(2)$ invariant Lagrangian. The mass terms for the gauge bosons of the form $\frac{1}{2}m_A^2 A_\mu A_\mu$ are not invariant under the gauge transformation $A \rightarrow A - \partial^\mu\chi$. Thus, adding mass terms by hand destroys gauge invariance and ruins renormalizability. Because of this in the early 1960s these theories have not been taken seriously and the successful predictions for the neutral currents were considered to be accidental. The breakthrough came with the theoretical understanding of the renormalizability of the Yang-Mills theories described in Refs. [10], [11] and the Higgs mechanism. The Higgs mechanism will be the solution that restores gauge invariance to the Lagrangian, and allows for a renormalizable model with massive W and Z bosons.

2.4 Higgs mechanism

The difficulty with the mass terms can be understood in the case of abelian theories. Massless spin one particles have only two spin degrees of freedom, the longitudinal component does not contribute to the kinetic energy and the free theory is gauge invariant. Adding a mass term, the longitudinal component of the gauge bosons becomes physical and destroys unitarity. The massive gauge bosons have three spin states. At high energies, however, the longitudinal component behaves like a scalar particle suggesting

that the gauge symmetry might be maintained if we add scalar particles to the theory. This was the crucial observation of Higgs [12], Brout and Englert [13] leading to the discovery of the Higgs mechanism. If the ground state $\langle \Phi \rangle$ of the scalar field is not equal to zero, without the requirement of local symmetry, we get spontaneous symmetry breaking with massless Goldstone bosons associated with each broken generator. In gauge theory at high energies when masses are negligible we have massless Goldstone bosons and massless gauge bosons. At low energies, however, the Goldstone bosons disappear from the theory: they provide the longitudinal component of the massive gauge bosons. This feature of gauge theories coupled to Goldstone bosons is called the Higgs mechanism.

The Standard Model is defined with the simplest realization of the Higgs mechanism [9]: one adds to the massless $SU(2) \times U(1)$ invariant Lagrangian one scalar doublet with appropriate hypercharge, $Y(\Phi)=1/2$,

$$\Phi = \begin{pmatrix} \phi^+ \\ \phi^0 \end{pmatrix},$$

with gauge kinetic energy terms and self-interactions

$$\mathcal{L}_\Phi = (D_\mu \Phi)^\dagger D^\mu \Phi - V(\Phi),$$

and with Yukawa couplings

$$\begin{aligned} \mathcal{L}_{Yukawa} = & \sum_{ff'} \lambda_{ff'}^U (\bar{Q}_{Lf} \tilde{\Phi}) u_{Rf'} + \lambda_{ff'}^D (\bar{Q}_{Lf} \Phi) d_{Rf'} \\ & + \lambda_{ff'}^E (\bar{L}_{Lf} \Phi) e_{Rf'} + h.c. \end{aligned}$$

Q_{Lf} and L_{Lf} denote the quark and lepton doublet Weyl spinors for family f and $\lambda_{ff'}^U, \lambda_{ff'}^D, \lambda_{ff'}^E$ denote complex coupling matrices in the family space. There is no Yukawa coupling for neutrinos, since it is assumed that in nature only left-handed neutrinos exist¹.

The idea is to set the bare mass squared parameter μ , of the scalar field, to a negative value, and see what happens. A convenient parameterization of the scalar potential is

$$V(\Phi) = \lambda(\Phi^2 - v^2)^2,$$

¹The existence only of left-handed neutrinos (and right-handed antineutrinos) together with the law of lepton number conservation imply that the neutrino is massless. A massive particle can be "overtaken", namely it moves in the opposite direction. It means that its momentum, but not its spin would change sign and so it would change from a left-handed particle to a right-handed one. In the case of neutrino, this means that by overtaking a neutrino we would see it as an antineutrino, which violates the law of lepton conservation. It therefore must be impossible to overtake a neutrino, meaning that it travels with the speed of light, and therefore it is massless.

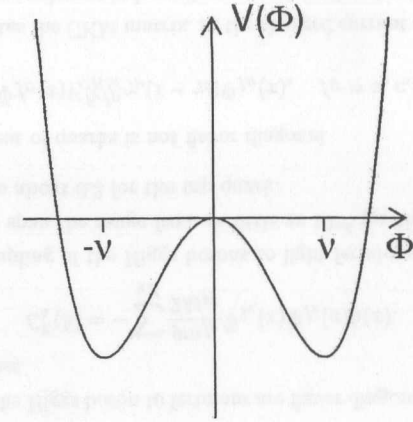


Figure 2.2: Scalar potential as a function of Φ for negative values of the mass squared parameter, $\mu^2 > 0$.

from which the mass squared parameter is given by

$$\mu^2 = \left. \frac{d^2 V}{d\Phi^2} \right|_{\Phi=0} = -4\lambda v^2.$$

The "mass" itself is purely imaginary. What happens is that the scalar potential in the Lagrangian is not minimized by an absence of the scalar field, but rather by its presence. The lowest energy state of the system is filled with virtual scalar particles. In Figure 2.2 the potential of a scalar field with negative mass squared is shown as a function of the scalar field value. For small values of this field, the negative quadratic term dominates the potential; at large field values, the positive quartic term dominates, ensuring a bound potential at infinite field value. The result is a global minimum at nonzero field value. The scalar field has acquired a vacuum expectation value $v = \langle 0 | \Phi | 0 \rangle \neq 0$. Since the scalar field is coupled to the W and Z bosons, the virtual scalars in this nontrivial vacuum will alter the inertia of a propagating W or Z; this inertia manifests itself as W and Z masses.

In quantum field theory, a set of particle states is constructed by acting on the vacuum with creation and annihilation field operators. These field operators represent physical particles and will vanish when averaged between vacuum states, because the

true vacuum contains no physical particles. Consequently, the useful field is not Φ but

$$h = \Phi - v \quad (2.10)$$

which has a vanishing vacuum expectation value.

When Φ is replaced with $h + v$ everywhere in the Lagrangian, the introduction of the parameter v , which has mass dimension, leads to the following:

- the W and Z particles acquire mass terms;
- the Goldstone bosons disappear;
- a massive scalar, called Higgs particle, appears.

Because the number of degrees of freedom are unaltered, the three Goldstone bosons, two charged and one neutral, which have disappeared have in fact emerged as the physical, longitudinal components of the W and Z.

Since at least three scalar field degrees of freedom are required to provide the longitudinal W^\pm and Z modes, and the scalar field must enter the Lagrangian in a gauge invariant manner, the minimal $SU(2)$ representation for the scalars is a complex doublet. For this reason, the Standard Model with a single Higgs doublet is called the "minimal model".

The complex doublet contains four degrees of freedom, and therefore one real scalar field is left over as a particle appearing in the physical spectrum: the scalar sector has left behind an experimental signature.

Rewriting the Lagrangian in terms of h and v we obtain mass terms for the gauge bosons

$$\mathcal{L}_m = |D_\mu \langle \Phi \rangle|^2 = \frac{v^2}{4} \left[g^2 W_\mu^+ W^{-\mu} + \frac{1}{2} (W_\mu^3, B_\mu) \begin{pmatrix} g^2 & gg' \\ gg' & g'^2 \end{pmatrix} \begin{pmatrix} W^{3\mu} \\ B^\mu \end{pmatrix} \right].$$

In terms of the A_μ and Z_μ fields the mass matrix of the neutral gauge bosons becomes diagonal and one gets

$$M_W = \frac{1}{2} g v, \quad M_Z = \frac{v}{2} \sqrt{g^2 + g'^2} = \frac{M_W}{\cos \theta_W}, \quad M_\gamma = 0,$$

where g is the $SU(2)$ gauge coupling and $\cos \theta_W$ is the weak mixing angle. The three parameters v , g and $\cos \theta_W$ are constrained by the data, for example by the fine structure constant α , the Fermi constant G_F , the W and Z masses, charged and neutral current neutrino cross sections, etc.

For the mass of the Higgs boson we obtain

$$m_h^2 = 2\lambda v^2. \quad (2.13)$$

Therefore the strength of the self-interaction of the Higgs boson can be expressed in terms of the Higgs and gauge boson masses and the gauge coupling:

$$\lambda = \frac{m_h^2}{8M_W^2} g^2.$$

The gauge symmetry uniquely defines the coupling of the gauge bosons to the Higgs boson allowing to predict for example the value of the partial-width of the Higgs boson

$$\Gamma(h \rightarrow W^+ W^-) = \frac{g^2 m_h^2}{64\pi M_W^2} \sqrt{1 - 4x_h} (1 - 4x_h + 12x_h^2), \quad x_h = \frac{M_W^2}{m_h^2}.$$

With increasing m_h the coupling grows as m_h^3 . In particular for $m_h \approx 1$ TeV we obtain $\Gamma(h) \approx m_h$. This indicates the difficulty with the validity of perturbative unitarity in case of a heavy Higgs boson.

Something else "happens": fermions, whose masses are forbidden by the gauge symmetry, also acquire a mass: substituting the shifted field (2.4) in the Yukawa coupling of Φ to fermions we get the mass matrices of the fermions and their couplings to the Higgs boson. The physical fermion states are obtained by diagonalizing the mass matrices with the help of two unitary matrices,

$$\frac{v}{\sqrt{2}} U(\chi)_L^\dagger \lambda^\chi U(\chi)_R = \mathcal{M}_{\text{diag}}^\chi, \quad \chi = U, D, E,$$

where λ is the fermion mass matrix, U_L, U_R are unitary matrices and $\mathcal{M}_{\text{diag}}$ is diagonal with real diagonal elements. $\chi = N$ does not occur since it is assumed that right handed neutrinos do not exist. The diagonal element of $\mathcal{M}_{\text{diag},ff'}^\chi$ gives the mass values and f runs over the three families. This diagonalization produces three important physical results.

1. The couplings of the Higgs boson to fermions are flavor diagonal and proportional to the fermion mass

$$\mathcal{L}_h^Y(h) = - \sum_{\chi, f} \frac{g m_{f\chi}}{2M_W} \bar{\Psi}_{f\chi}(x) \Psi_{f\chi}(x) h(x). \quad (2.17)$$

Therefore, the coupling of the Higgs bosons to light fermions is very weak. The Yukawa couplings span the range from as little as 10^{-6} for the electron, to 10^{-2} for the b quark, to about 0.3 for the top quark.

2. The charged current of quarks is not flavor diagonal

$$J_\mu^-(x) = \sum_{f_U, f_D} \bar{\Psi}_{f_U}(x) V_{CKM}^{f_U f_D} \gamma_\mu (1 - \gamma_5) \Psi_{f_D}(x), \quad f_U = u, c, t, \quad f_D = d, s, b$$

where V_{CKM} denotes the CKM matrix. In the charged current of quarks, six fields with five physically irrelevant independent phases are involved (with one relevant phase for $U(1)_Y$), therefore four phases of unitary CKM matrix can be rotated away and $3^2 - 5 = 4$ physically relevant parameters result.

- After the Higgs mechanism the neutral current remains flavor diagonal (GIM mechanism [14]), therefore in leading order there are no flavor changing neutral current transitions. In higher order, as a result of virtual flavor changing charged current exchanges, flavor changing neutral current transitions are allowed but suppressed strongly because of the smallness of the Fermi coupling.

2.5 Boundaries on the Higgs mass

The Standard Model does not give a precise prediction for the mass of the Higgs boson. We can, however, use arguments of self-consistency to place lower and upper bounds on the mass of the Higgs particle in the Standard Model.

2.5.1 Theoretical bounds

We have obtained the Higgs boson mass $m_h = \sqrt{2\lambda}v$ (Eq. 2.5) as a function of the vacuum expectation value of the Higgs field and the quartic coupling λ . The quartic coupling is a free parameter, and therefore is the Higgs mass. The bounds on the Higgs mass follow from the behavior of the quartic coupling which satisfies the following renormalization group equation describing its change as a function of the scale [15]:

$$\frac{d\lambda}{dt} = \frac{1}{16\pi^2}(6\lambda^2 + 6\lambda h_t^2 - 6h_t^4 + \text{gauge terms}), \quad (2.19)$$

where $t = \ln(Q^2/\mu^2)$. Here h_t is the top-quark Yukawa coupling. The quartic coupling grows with rising energy indefinitely, thus an upper bound on m_h follows from the requirement that the theory is valid up to the Planck scale M_{Planck} or up to a given cut-off scale Λ below M_{Planck} [15]. The upper bound on m_h depends mildly on the top-quark mass through the impact of the top-quark Yukawa coupling on the running of the quartic coupling λ .

On the other hand, the requirement of vacuum stability in the Standard Model (positivity of λ) imposes a lower bound on the Higgs boson mass, which crucially depends on the top-quark mass as well as on the cut-off parameter Λ [15], [16]. The dependence of this lower bound on m_t is due to the effect of the top-quark Yukawa coupling on the quartic coupling in Eq. (2.7), which drives λ to negative values at large scales, thus destabilizing the standard electroweak vacuum.

Figure 2.3 from Ref. [17] shows the perturbativity and stability bounds on the Higgs boson mass of the Standard Model for different values of the cut-off parameter Λ at which new physics is expected and for $m_t \approx 174$ GeV. We see that the discovery of a Higgs particle at LEP2 would imply that the Standard Model breaks down at a scale Λ well below the scale for Grand Unified Theories, M_{GUT} , or the Planck scale M_{Planck} .

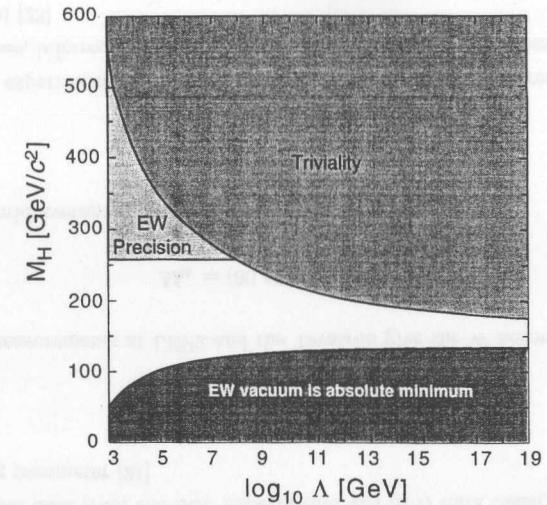


Figure 2.3: Bounds on the Standard Model Higgs boson mass. Λ denotes the energy scale up to which the Standard Model is valid. (From Ref. [17])

Actually, if the Standard Model is valid up to $\Lambda \approx M_{\text{GUT}}$ or M_{Planck} , for $m_t \approx 174$ GeV only a small range of values is allowed: $134 \text{ GeV} < m_h < \approx 200 \text{ GeV}$. For $m_t = 174$ GeV and $m_h = 115$ GeV new physics should appear below the scale $\Lambda = 10^6$ GeV [18].

The relation between m_h and the Higgs quartic coupling allows us to say the following:

- the Higgs particle has a mass below a TeV, or some new physics must occur below a scale of a few TeV,
- or,
- there is no Higgs below a few TeV and the theory is nonperturbative at high energy; the Higgs coupling λ is large and the longitudinal modes of the W and Z become strongly interacting.

2.5.2 Unitarity constraints on the Higgs mass

The connection between unitarity and an upper limit on the Higgs mass was described in Ref. [19].

In a renormalizable theory amplitudes must not grow indefinitely as a function of energy. The Standard Model including the Higgs boson is renormalizable, and amplitudes behave as they should. Suppose we compute the scattering amplitude for $W^+W^- \rightarrow W^+W^-$ but omitting all diagrams involving the Higgs boson. At the leading order level there are γ and Z exchanges in the s and t channels and a contact term, see the diagrams of Figure 2.4.

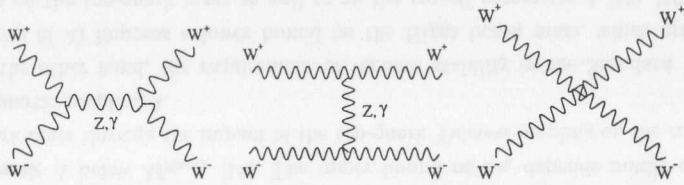


Figure 2.4: Leading order diagrams for the WW scattering.

The energy behavior of the amplitude for longitudinally polarized W bosons is written as,

$$A^{\gamma,Z}(W_L W_L \rightarrow W_L W_L) \propto \frac{G_F}{\sqrt{s}} s(1 + \cos \theta).$$

It grows indefinitely with s . The angle θ is the scattering angle in the centre-of-mass system. This linear divergence is canceled by the contributions of Higgs boson exchanges in the s and t channels, see Figure 2.5.

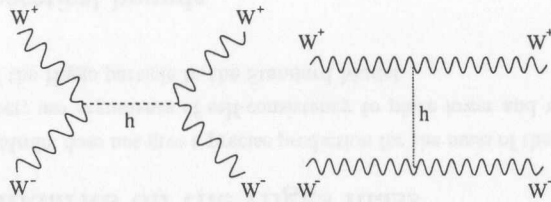


Figure 2.5: Higgs boson contributions to the WW scattering.

The resulting amplitude is

$$A \propto \left(-\frac{G_F}{4\pi\sqrt{2}}\right) m_h^2,$$

at high energies $s \rightarrow \infty$.

Partial wave unitarity requires that

$$|a^J| \leq 1,$$

for the J th partial wave amplitude. Applying this condition to the $J=0$ amplitude defined through

$$A = 8\pi \sum_{J=0}^{\infty} (2J+1) a^J P_J(\cos \theta),$$

yields

$$m_h^2 \leq 2\pi\sqrt{2}/G_F \propto (850 \text{ GeV})^2.$$

For $m_h > (2\pi\sqrt{2}/G_F)^{1/2}$ the partial wave unitarity bound $|a^{J=0}| \leq 1$ is violated for energy \sqrt{s} greater than m_h .

2.5.3 Limits from indirect searches

The Higgs boson influences the observed electroweak reactions through higher order processes beyond the tree level. Hence, if an electroweak observable is precisely measured, it is possible to determine the Higgs boson mass via radiative corrections. The measured electroweak observables are in agreement with the predictions of the Standard Model at the level of 0.1% [20], [21]. The degree of agreement can be seen in Figure 2.6.

The Z-pole data from the LEP experiments and SLD data taken together yield a weak mixing parameter [21]

$$\sin^2 \theta_W^{\text{eff}} = 0.23136 \pm 0.00014.$$

Direct measurements at LEP2 and the Tevatron give the W boson mass [21]

$$M_W = (80.451 \pm 0.033) \text{ GeV},$$

while the world average top-quark mass from CDF and D0 is [22]

$$m_t = (174.3 \pm 5.1) \text{ GeV}.$$

The NuTeV experiment at Fermilab has reported a competitive indirect determination of the W mass, inferred from measurements of the $\nu_\mu N$ and $\bar{\nu}_\mu N$ cross sections.

They find [23]

$$M_W = (80.26 \pm 0.11) \text{ GeV}.$$

Summer 2001

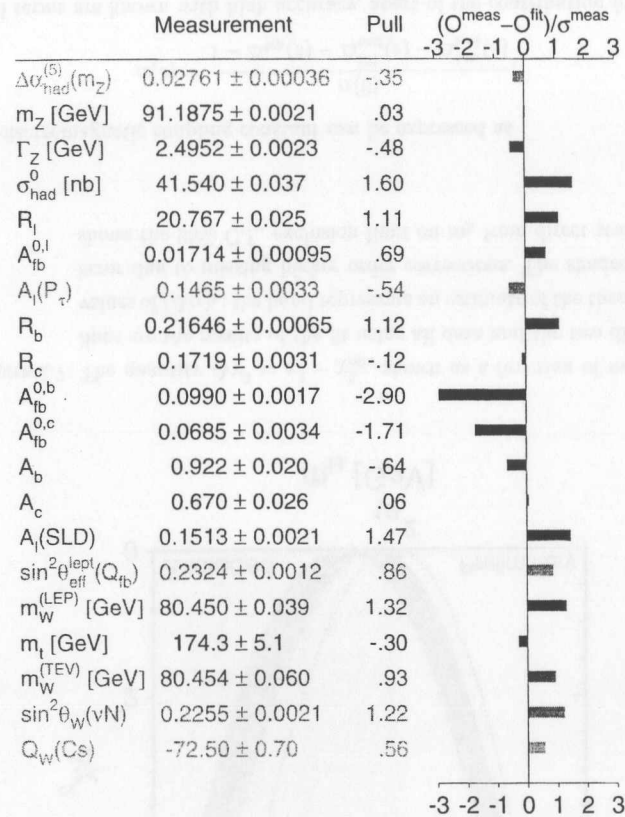


Figure 2.6: Compilation of the world's electroweak data as of summer 2001, and the deviation (in number of standard deviations) of each measurement from the Standard Model fit (from Ref. [21]). The values of the input parameters (including m_h) are allowed to vary and the overall χ^2 is minimized. Note the high level of precision of the measurements of the various observables, many being at the 0.1% level.

A new evaluation of the finite part of the $\mathcal{O}(\alpha^2)$ corrections to the muon lifetime [24], leads to a value for the Fermi constant measured in muon decay,

$$G_F = (1.16637 \pm 0.00001) \times 10^{-5} \text{GeV}^{-2}.$$

From the wealth of particle searches and cross section measurements at LEP2, no anomalies have been observed in the reactions $e^+e^- \rightarrow W^+W^-$, ZZ and $f\bar{f}$.

Similarly, the overall conclusion from HERA is that the neutral-current and charged-current cross sections measured in e^+p collisions have the expected shape and reproduce the known values of W and Z boson masses.

The success of the electroweak theory allows us to use standard model fits to the electroweak observables to determine best values for the parameters that are not yet directly constrained by experiment. Over the past ten years, the greatest sensitivity has been to the value of the top quark mass, and fits to the electroweak observables gave early indications for the large mass of the top quark [25]. Now when the top quark mass is known rather well from the Tevatron experiments we can use the Standard Model fits to estimate the mass of the Higgs boson. To do this a series of fits with fixed m_h values is performed. The difference in the χ^2 values is shown in Figure 2.7. The consensus of the fit is that, within the standard electroweak theory, the Higgs boson should be light.

In the global fit of Ref. [21] the best fit value for the mass of the Standard Model Higgs boson, using $(\Delta\alpha)_{\text{had}}^{(5)} = 0.02761 \pm 0.00036$ [26], is

$$m_h = 88_{-35}^{+53} \text{GeV}; \quad \log(m_h/\text{GeV}) = 1.94_{-0.22}^{+0.21},$$

which at the 95% confidence level leads to the upper bound of 196 GeV. The radiative correction terms depend on $\log(m_h)$, therefore the constraints on the Higgs mass are not very strong.

As mentioned already, the QED running coupling constant evaluated at the Z pole, $\alpha(M_Z^2)$, plays an important role in the prediction of the mass of the Higgs particle, m_h . Among the input parameters generally used in global fits to electroweak data, $\alpha(M_Z^2)$, has the largest experimental uncertainty and is the limiting quantity on the precision of the Standard Model calculations of the Higgs mass. The dominant uncertainties on $\alpha(M_Z^2)$ are due to the effects of hadronic vacuum polarization, which cannot yet be reliably calculated. In order to determine the vacuum polarization, measured (or calculated in perturbative QCD) R values are used, where R is the cross section for $e^+e^- \rightarrow \gamma^* \rightarrow \text{hadrons}$, in units of the QED cross section for $e^+e^- \rightarrow \mu^+\mu^-$ process, namely

$$R = \frac{e^+e^- \rightarrow \text{hadrons}}{e^+e^- \rightarrow \mu^+\mu^-}.$$

where $e^+e^- \rightarrow \mu^+\mu^- = \sigma_{\mu\mu}^0 = \frac{3\pi\alpha^2(0)}{3s}$. The uncertainties in $\alpha(M_Z^2)$ are dominated by the errors in the values of R in the centre-of-mass energy range below 5 GeV.

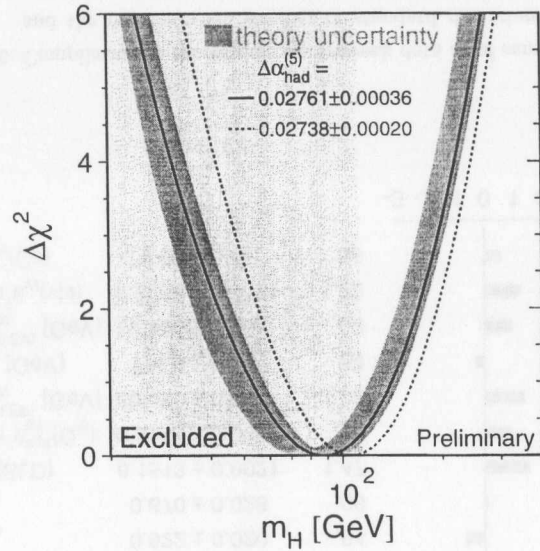


Figure 2.7: The quantity $\Delta\chi^2 = \chi^2 - \chi_{\min}^2$ shown as a function of m_h . The lines are the results of the fit using all data and the two different values of $(\Delta\alpha)_h$; the band represents an estimate of the theoretical error due to missing higher order corrections. The shaded band shows the 95% C.L. exclusion limit on m_h from direct searches.

The electromagnetic coupling constant can be expressed as

$$\alpha(s) = \frac{\alpha(0)}{1 - \Delta_{\text{lep}}(s) - \Delta_{\text{had}}^{(5)}(s) - \Delta_{\text{had}}^{\text{top}}(s)},$$

where all terms are known with high accuracy, apart of the contribution from the five light quark flavours, $\Delta_{\text{had}}^{(5)}(s)$. The value of $\Delta_{\text{had}}^{(5)}(s)$ is obtained by integrating the R distribution,

$$\Delta_{\text{had}}^{(5)}(s) \propto \int_{4m_\pi^2}^{\infty} \frac{R(s')ds'}{s'(s' - s)}.$$

The error on $\Delta_{\text{had}}^{(5)}(s)$ is further reduced when relying on perturbative QCD. Using the value $\Delta_{\text{had}}^{(5)}(s) = 0.02738 \pm 0.00020$ [28] which includes the recent results obtained at the BES experiment [27] we obtain:

$$m_h = 106_{-38}^{+57} \text{ GeV}; \quad \log(m_h/\text{GeV}) = 2.03 \pm 0.19,$$

corresponding to an upper limit on the Higgs mass of 222 GeV at 95% confidence level.

In conclusion, the central value depends strongly on the top quark mass and the value of $\Delta_{\text{had}}^{(5)}(s)$ used. Depending on the value of $\Delta_{\text{had}}^{(5)}(s)$, upper limits on the Higgs boson mass of 196 - 222 GeV are obtained at 95% confidence level. These results are compatible with the results from direct searches for the Higgs boson, which exclude Higgs masses up to $m_h = 114.1$ GeV at 95% confidence level.

2.5.4 Limits from direct searches

Direct searches for the Standard Model Higgs boson (other extensions of the Standard Model are discussed later) have been performed at LEP2 [29].

In e^+e^- collisions the Standard Model Higgs boson is expected to be produced mainly by the Higgs-Strahlung mechanism and to a lesser extent by the WW fusion process. Its dominant decay mode is into $b\bar{b}$ pair in the mass range accessible at LEP with a branching fraction of 74% at $m_h=115$ GeV. The second most important decay mode is to tau pairs, with a branching fraction of about 7%, and the WW decays take 8%. Efficient and pure b-tagging is therefore important to search for the Higgs boson at LEP. Four search topologies arise from the decays of the accompanying Z boson: 4-jet final state ($h \rightarrow b\bar{b}, Z \rightarrow q\bar{q}$), the missing energy channel ($h \rightarrow b\bar{b}, Z \rightarrow \nu\bar{\nu}$), the tau final states ($h \rightarrow b\bar{b}, Z \rightarrow \tau^+\tau^-$ and $h \rightarrow \tau^+\tau^-, Z \rightarrow q\bar{q}$) and the lepton final states ($h \rightarrow b\bar{b}, Z \rightarrow e^+e^-$ or $\mu^+\mu^-$).

The distribution of the reconstructed mass of the Higgs boson for all experiments together is shown in Figure 2.8 (left). This distribution is summed over different search channels, at different centre-of-mass energies. Therefore candidates in clean channels are included in the same bins as signal and background from other channels with less performance. Also, the reconstructed mass resolutions can differ, and depend on how close m_h is to the kinematic limit, which changes with \sqrt{s} . The information contained in this distribution can therefore be misleading.

However, there is no loss of sensitivity in the confidence level calculations when combining all bins, of all histograms in all variables (as reconstructed mass, b-tag, or combinations of these, etc.) with the method described in section 6.1.

The experimental data for the Standard Model Higgs search show an excess of 2.1σ (see section 6.1) significance, or $(1-\text{CL}_b)=0.034$ at $m_h \sim 115$ GeV. The maximum likelihood occurs at $m_h=115.6$ GeV. The distribution of the log-likelihood ratio (see

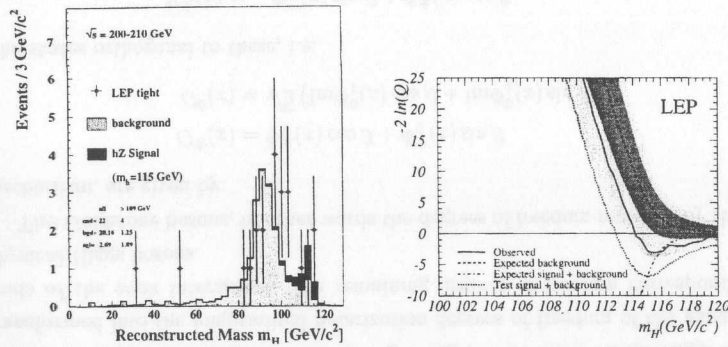


Figure 2.8: (Left) Reconstructed Higgs mass; (Right) Negative log-likelihood ratio as a function of Higgs mass for the combined LEP data and energies up to 209 GeV (from Ref. [29]).

section 6.1), $-2\ln Q$, is shown in Figure 2.8 (right) as a function of m_h , for the combined LEP data and energies up to 209 GeV. The value of $m_h = 115.6$ GeV corresponds to the position where $-2\ln Q$ has its minimum value.

The lower limit on the Higgs mass is $m_h > 114.1$ GeV at 95% confidence level, with a median expected limit of 115.4 GeV.

2.6 Extended Higgs models

We recall that in the minimal (one Higgs doublet) Standard Model there is a single parameter in the Higgs sector: λ , or equivalently $m_h = \sqrt{2\lambda}v$. However, this minimal choice is arbitrary and one should investigate the implications of more complicated Higgs models.

A model having as base a different or extended Higgs sector can not be considered to be an alternative to the Standard Model if its predictions are contradicted by experimental results. The two most important experimental results that impose constraints on the structure of the Higgs sector are:

1. the ρ parameter, defined as

$$\rho \equiv \frac{M_{W^\pm}^2}{M_Z^2 \cos^2 \theta_W},$$

with a value very close to one.

2. the observation that the existence of flavor changing neutral currents, i.e. couplings between a neutral boson field and two fermion fields with different flavors, are very small.

In the Standard Model ρ equals one, and there are no flavor changing neutral currents. In extended models this is not necessarily the case.

2.6.1 Two Higgs Doublet Model (2HDM)

In the two Higgs doublet model (2HDM) the Higgs sector consists of two complex Higgs doublet fields with hypercharge $Y_k = \frac{1}{2}$,

$$\Phi_1(x) = \begin{pmatrix} \phi_1^+(x) \\ \phi_1^0(x) \end{pmatrix}, \quad \Phi_2(x) = \begin{pmatrix} \phi_2^+(x) \\ \phi_2^0(x) \end{pmatrix}.$$

The most general re-normalizable and gauge invariant Higgs potential has fourteen independent real parameters and is given in Refs. [30], [31] as:

$$\begin{aligned} V(\Phi_1, \Phi_2) = & \mu_1^2 \Phi_1^\dagger \Phi_1 + \mu_2^2 \Phi_2^\dagger \Phi_2 + \left(\mu_\Delta^2 \Phi_1^\dagger \Phi_2 + h.c. \right) \\ & + \lambda_A \left(\Phi_1^\dagger \Phi_1 \right)^2 + \lambda_B \left(\Phi_2^\dagger \Phi_2 \right)^2 \\ & + \lambda_C \left(\Phi_1^\dagger \Phi_1 \right) \left(\Phi_2^\dagger \Phi_2 \right) + \lambda_D \left(\Phi_1^\dagger \Phi_2 \right) \left(\Phi_2^\dagger \Phi_1 \right) \\ & + \frac{1}{2} \left(\left(\Phi_1^\dagger \Phi_2 \right) \left(\lambda_E \Phi_1^\dagger \Phi_2 + \lambda_F \Phi_1^\dagger \Phi_1 + \lambda_G \Phi_2^\dagger \Phi_2 \right) + h.c. \right), \end{aligned}$$

where μ_1^2 , μ_2^2 , λ_A , λ_B , λ_C and λ_D are real parameters while μ_Δ^2 , λ_E , λ_F and λ_G may be complex. If one requires the potential to be invariant under the CP symmetry, all parameters must be real and there are two different possibilities to restrict the potential [32]².

One possible way to satisfy the experimental limits on flavor changing neutral currents is to allow all fermion fields of the same type to couple to only one of the Higgs doublet fields in the model [33]. This condition can be enforced by requiring invariance of the Lagrangian density under the discrete symmetry

$$\begin{aligned} \Phi_1(x) & \longrightarrow \Phi_1(x), \quad \Phi_2(x) \longrightarrow -\Phi_2(x), \\ \Psi_L^F(x) & \longrightarrow \Psi_L^F(x), \quad \Psi_R^F(x) \longrightarrow \pm \Psi_R^F(x), \end{aligned}$$

²The major difference of the potentials is in the Higgs self-couplings. This leads to a different phenomenology in the cases where the Higgs particles interact among themselves, or when loop effects play an important role. However, the potentials are equivalent in what concerns the Higgs couplings to gauge bosons and fermions.

where the plus sign applies to fermion fields that couple to $\Phi_1(x)$ and the minus sign to fermion fields that couple to $\Phi_2(x)$. If the Higgs potential is allowed to break this symmetry only softly, i.e. in the lowest order terms, λ_F and λ_G must be zero.

The resulting potential, which is known as 'Potential A', can then be parameterised as [34]:

$$\begin{aligned} V(\Phi_1, \Phi_2) = & \lambda_1 \left(\Phi_1^\dagger \Phi_1 - \frac{v_1^2}{2} \right)^2 + \lambda_2 \left(\Phi_2^\dagger \Phi_2 - \frac{v_2^2}{2} \right)^2 \\ & + \lambda_3 \left(\left(\Phi_1^\dagger \Phi_1 - \frac{v_1^2}{2} \right) + \left(\Phi_2^\dagger \Phi_2 - \frac{v_2^2}{2} \right) \right)^2 \\ & + \lambda_4 \left(\Phi_1^\dagger \Phi_1 \Phi_2^\dagger \Phi_2 - \Phi_1^\dagger \Phi_2 \Phi_2^\dagger \Phi_1 \right) \\ & + \lambda_5 \left(\text{Re} \left(\Phi_1^\dagger \Phi_2 \right) - \frac{v_1 v_2}{2} \right)^2 \\ & + \lambda_6 \left(\text{Im} \left(\Phi_1^\dagger \Phi_2 \right) \right)^2, \end{aligned}$$

where the λ 's are real parameters. If all the λ 's are non-negative the minimum of the potential is given for the vacuum expectation values

$$\Phi_1^{(0)}(x) = \frac{1}{\sqrt{2}} \begin{pmatrix} 0 \\ v_1 \end{pmatrix}, \quad \Phi_2^{(0)}(x) = \frac{1}{\sqrt{2}} \begin{pmatrix} 0 \\ v_2 \end{pmatrix}.$$

Since the sum of the squares of the two vacuum expectation values are related to the mass of the W^\pm boson,

$$m_{W^\pm}^2 = \frac{g^2}{4} (v_1^2 + v_2^2),$$

only the ratio between them is important for the predictions of the model. This ratio is usually referred to as $\tan \beta$:

$$\tan \beta = \frac{v_1}{v_2}.$$

Due to the Higgs mechanism three of the eight degrees of freedom of the Higgs fields are transformed into the longitudinal polarization degrees of freedom of the gauge boson fields of the weak interaction. The remaining degrees of freedom correspond to the physical Higgs bosons.

The Goldstone bosons, in other words the degrees of freedom removed by the Higgs mechanism, are given by

$$\begin{aligned} G^\pm(x) &= \Phi_1^\pm(x) \cos \beta + \Phi_2^\pm(x) \sin \beta \\ G^0(x) &= \sqrt{2} \left(\text{Im} \Phi_1^0(x) \cos \beta + \text{Im} \Phi_2^0(x) \sin \beta \right). \end{aligned}$$

The states orthogonal to these, i.e.

$$\begin{aligned} H^\pm(x) &= -\Phi_1^\pm(x) \sin \beta + \Phi_2^\pm(x) \cos \beta \\ A^0(x) &= \sqrt{2} \left(-\text{Im} \Phi_1^0(x) \sin \beta + \text{Im} \Phi_2^0(x) \cos \beta \right), \end{aligned}$$

correspond to a pair of charged Higgs bosons H^\pm and a CP -odd neutral Higgs boson A^0 with masses

$$\begin{aligned} m_{H^\pm}^2 &= \frac{\lambda_4}{2} (v_1^2 + v_2^2) \\ m_{A^0}^2 &= \frac{\lambda_6}{2} (v_1^2 + v_2^2). \end{aligned}$$

The remaining degrees of freedom correspond to two CP -even neutral Higgs bosons:

$$\begin{aligned} H^0(x) &= \sqrt{2} \left((\text{Re} \Phi_1^0(x) - v_1) \cos \alpha \right. \\ &\quad \left. + (\text{Re} \Phi_2^0(x) - v_2) \sin \alpha \right) \\ h^0(x) &= \sqrt{2} \left(-(\text{Re} \Phi_1^0(x) - v_1) \sin \alpha \right. \\ &\quad \left. + (\text{Re} \Phi_2^0(x) - v_2) \cos \alpha \right), \end{aligned}$$

where the Higgs mixing angle α and the masses can be derived by diagonalizing the mass squared matrix

$$M = \begin{pmatrix} 2(\lambda_1 + \lambda_3)v_1^2 + \frac{\lambda_5 v_2^2}{2} & (2\lambda_3 + \frac{\lambda_5}{2})v_1 v_2 \\ (2\lambda_3 + \frac{\lambda_5}{2})v_1 v_2 & 2(\lambda_2 + \lambda_3)v_2^2 + \frac{\lambda_5 v_1^2}{2} \end{pmatrix}.$$

This results in

$$\tan \beta = \frac{2M_{12}}{M_{11} - M_{22}}$$

and

$$m_{H^0, h^0}^2 = \frac{1}{2} \left(M_{11} + M_{22} \pm \sqrt{(M_{11} - M_{22})^2 + 4M_{12}^2} \right).$$

To summarize, this model possesses five physical Higgs bosons: two neutral CP -even scalars (h^0 and H^0 , where, by convention, $m_{H^0} > m_{h^0}$), a neutral CP -odd scalar (A^0) and a charged pair (H^\pm). Instead of the one free parameter as in the Standard Model, this model has six free parameters: four Higgs masses, the ratio of vacuum expectation values, $\tan \beta$, and a Higgs mixing angle, α . The value $v_1^2 + v_2^2$ is fixed by the W mass $M_W^2 = g^2(v_1^2 + v_2^2)/2$.

A general two doublet model has less predictive power. Only a few general statements can be made [35]: there are no tree level $H^\pm W^\mp Z$, $H^\pm W^\mp \gamma$, $A^0 Z Z$ or $A^0 W^+ W^-$ vertices; in a CP -conserving theory, there are no hhZ , HHZ , AAZ or hHZ couplings.

2.6.2 Bounds in Two-Doublet Models

In 2HDMs there are many more parameters, and thus a simple Figure as 2.3 cannot be drawn. The presence of extra field directions causes many more ways in which the vacuum can become unstable. The allowed parameter space is severely restricted. If the light neutral Higgs scalar is over about 140 GeV in mass, then the allowed range of the charged Higgs mass is below about 95 GeV. Even if the light neutral scalar is very

light, neither the charged scalars nor the pseudoscalar can be much heavier than about 150 GeV. However, these constraints are relaxed significantly if one assumes that the model breaks down before the unification scale [36].

Direct limits on the Higgs masses predicted by the general 2HDM, have been obtained at LEP2 [37]. Values of $1 \text{ GeV} \leq m_h \leq 58 \text{ GeV}$ and $10 \text{ GeV} \leq m_A \leq 65 \text{ GeV}$ are excluded at 95% confidence level for $-\pi/2 \leq \alpha \leq \pi/2$ and $0.4 \leq \tan \beta \leq 58.0$.

2.7 Higgs boson decay

2.7.1 Decays of the Standard Model Higgs boson

According to Eq. (2.6), the preferred decay mode of a standard Higgs is to the heaviest fermion or gauge boson pair kinematically allowed. Graphically this is denoted in Figure 2.9.

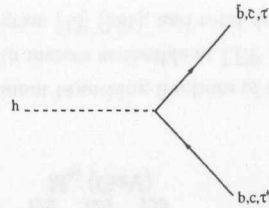


Figure 2.9: The dominant Higgs decay mode at LEP2.

The partial width of the Higgs decay into a fermion pair is described as [38], [39]:

$$\Gamma_{h \rightarrow f\bar{f}} = \frac{N_C G_F}{4\sqrt{2}\pi} m_f^2(m_h^2) m_h,$$

where $m_f(m_h^2)$ is the running quark mass. The QCD radiative corrections are absorbed into the scale dependence of the quark mass, evaluated at the Higgs boson mass. Near threshold the partial width is suppressed by an additional factor β_f^3 , where $\beta_f = (1 - 4m_f^2/m_h^2)^{1/2}$ is the fermion velocity.

If the mass of the standard Higgs increases towards the two vector boson threshold, the Higgs will decay dominantly to WW^* pairs, as shown in Figure 2.10, and ZZ^* pairs, one of the two gauge bosons being virtual below the threshold [40]. The partial width is denoted by:

$$\Gamma_{h \rightarrow VV^*} = \frac{3G_F^2 M_V^4}{16\pi^3} m_h R_V(M_V^2/m_h^2), \quad (V = W, Z),$$

where R_V is a function which depends on the ratio M_V^2/m_h^2 .

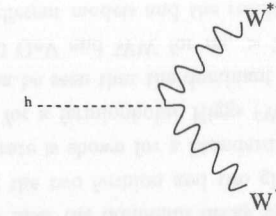


Figure 2.10: Feynman diagram for the Higgs decay into a WW pair.

The decay into ZZ^* is suppressed by an additional factor due to the mass of the Z boson and the reduced neutral current couplings with respect to the charged couplings.

Above the WW and ZZ decay thresholds, the partial width for these channels are written as:

$$\Gamma_{h \rightarrow VV} = \delta_V \frac{\sqrt{2}G_F}{32\pi} m_h^3 \left(1 - 4 \frac{M_V^2}{m_h^2} + 12 \frac{M_V^4}{m_h^4} \right) \cdot \beta_V,$$

with $\delta_V=2$ and 1 for $V=W$ and Z , respectively.

Decays into massless gluons or photons are not possible at tree level. These decays proceed at one loop level. We shall focus on the decay into two photons. The standard Higgs will couple to a photon pair via loops, as shown in Figure 2.11.

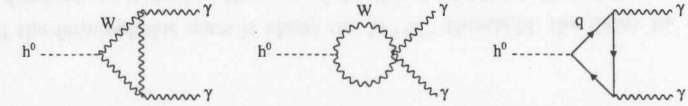


Figure 2.11: The two photon Higgs decay.

The vector boson loops dominate and contribute with opposite sign to the fermion loops. One-loop corrections are small [41] and the tree level width can be written as [42]:

$$\Gamma_{h^0 \rightarrow \gamma\gamma} = \frac{G_F \alpha^2 m_h^3}{128\sqrt{2}\pi^3} \left| \sum_f N_c Q_f^2 A_f(\tau_f) + A_W(\tau_W) \right|^2,$$

where N_c is the color factor, Q_f is the electric charge of the fermion, and the τ variables are defined by

$$\tau_f = \frac{m_h^2}{4m_f^2} \quad \text{and} \quad \tau_W = \frac{m_h^2}{4M_W^2}.$$

The above equations imply that the dominant fermion loop is that of the top-quark (i.e. $f=t$). The amplitudes A are real and vary from $A_W = -7$ (-12) for $\tau = 0$ (1), $A_t = 4/3$ (2) for $\tau = 0$ (1). Hence the W loops are dominant. For the Standard Model Higgs

boson the branching fraction has values $\text{BR}(h \rightarrow \gamma\gamma) \approx 0.1\% - 0.2\%$ for values of m_h between 80 and 130 GeV.

A graphical representation of the branching fractions for the Higgs boson as a function of its mass is shown in Figure 2.12 (left).

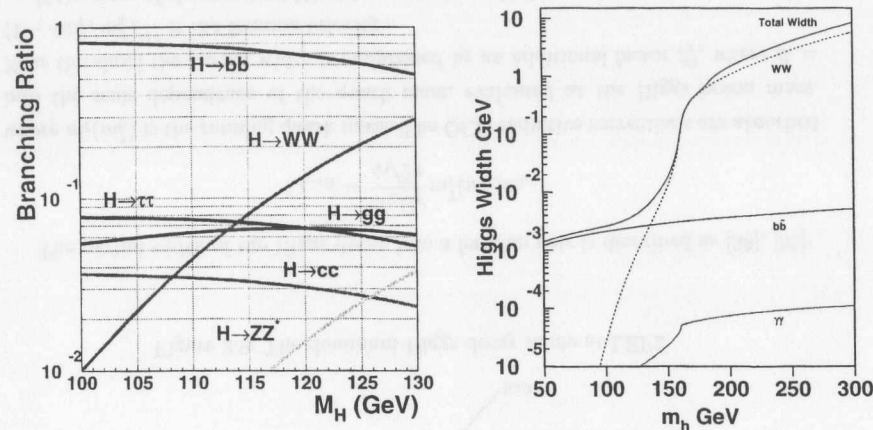


Figure 2.12: The dominant branching fractions of the Standard Model Higgs boson with masses accessible at LEP calculated with the HDECAY program [43] (left), and total decay width (right).

By adding up all possible decay channels, we obtain the total Higgs decay width shown in Figure 2.12 (right) for a top quark mass of 175 GeV. Up to masses of 140 GeV, the Higgs particle is very narrow, the width being predicted to be smaller than 10 MeV. After the opening of the gauge boson channels, virtual or real, the state becomes wider, reaching about 1 GeV at the ZZ threshold. Such a width cannot be measured directly in this mass range. Only above $m_h > 200$ GeV it becomes wide enough to be resolved experimentally.

2.7.2 Decays of fermiophobic Higgs bosons

Suppose the masses of the gauge bosons and fermions do not arise from the same Higgs doublet, then there may be scalar doublets which have standard strength couplings to the W and Z bosons, but suppressed couplings to fermions. Such scalars are called fermiophobic Higgs particles and are denoted h_F in the following.

The implementation of the fermiophobic Higgs mechanism changes the signatures expected for the Higgs bosons.

A fermiophobic Higgs model can be constructed requiring a $\Phi_F = -\Phi_F$ discrete symmetry in order to remove the Yukawa terms $\Phi_F \bar{\Psi}_L \Psi_R$ from the Lagrangian [44]. Other Higgs doublets can couple to the fermions and give rise to their masses.

A neutral fermiophobic Higgs will couple to a fermion pair through the processes shown in Figure 2.13,

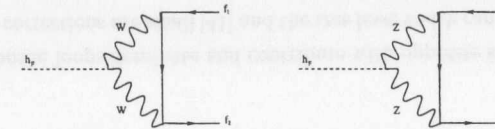


Figure 2.13: The fermiophobic Higgs decay into a fermion pair.

If the fermiophobic mass is above the W^+W^- threshold, the decay $h_F \rightarrow W^+W^-$ will dominate as it does in the case of the Standard Model. But if the mass is below $2M_W$, the dominant decay modes are unusual. In addition to the loop induced $f\bar{f}$ mode just pictured, there are the modes $h_F \rightarrow \gamma\gamma$ and γZ , generated by the loop graphs shown in Figure 2.14.

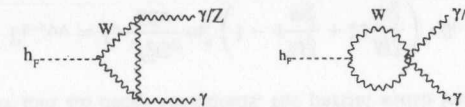


Figure 2.14: Possibilities for a fermiophobic Higgs decay.

Several branching fractions of the Standard Model Higgs are shown in Figure 2.15. From the figure one may infer the dominant decay modes of a neutral fermiophobic Higgs boson by omitting the two fermion and two gluon modes. For the purpose of comparison, the $h \rightarrow \gamma\gamma$ rate is shown for a Standard Model Higgs (fermions and W bosons in the loop) and for a fermiophobic Higgs (W loop only). Ignoring the loop induced $h \rightarrow f\bar{f}$ rate, it can be seen that the dominant decay mode for a fermiophobic Higgs is $\gamma\gamma$ for $m_h < 80$ GeV and WW for $m_h > 2M_W$. The induced $h \rightarrow f\bar{f}$ rate has been calculated in different models and the resulting branching fractions will be presented later for the 2HDM of type I.

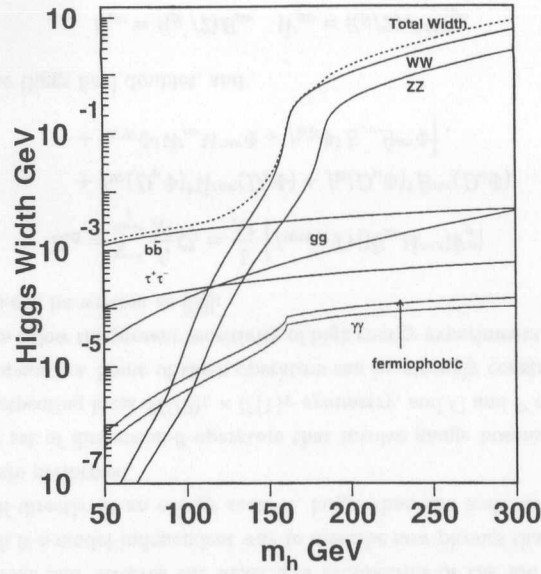


Figure 2.15: Branching fractions of the Standard Model Higgs boson calculated with the HDECAY program. For the purpose of comparison, the $h \rightarrow \gamma\gamma$ rate is shown for a Standard Model Higgs (fermions and W bosons in the loop) and for a fermiophobic Higgs (W loop only).

2.7.3 Higgs decaying into two photons

Since the Higgs boson is neutral and does not couple to photons at tree level the branching fraction is predicted to be small in the Standard Model. The single Higgs boson can decay into two photons via a quark- or W-boson loop. Therefore the rate is too small for observation at existing accelerators, even for a kinematically accessible Higgs boson. However, other theoretical models can accommodate large $h \rightarrow \gamma\gamma$ branching fractions. The list of theories having enhanced di-photon rates includes the fermiophobic Higgs models [44], [45], [46], Higgs triplet models [47], [48], top-quark condensate models [49], models with extra-dimensions [50], models with anomalous couplings [51] and many more. The most popular models will be briefly discussed in the following sections.

Fermiophobic Higgs bosons of the 2HDMs of type I

The extension of the Standard Model with two Higgs doublets has been discussed in section (2.6.1). The Yukawa coupling of the Higgs particles with the fermions can be chosen in two ways, usually denoted as models I and II. The most common choice is the structure assumed in the Minimal SuperSymmetric Model (MSSM): one of the Higgs doublets couples both to up type quarks and to leptons, and the other doublet couples to down type quarks. In this section a model of the so called type I is explored, namely only one of the Higgs doublets is allowed to couple to fermions. For this type of model the couplings hZZ and hWW are proportional to $\sin \delta$ where $\delta = \beta - \alpha$. We shall consider in the following only the high δ region. Moreover, if the mixing angle takes the value $\alpha = \pi/2$, then there is no mixing among H and h, and h interacts only with the gauge bosons, with the coupling proportional to $\sin(\beta - \pi/2) = -\cos \beta$.

The dominant decays of h in the mass range $m_h > 2M_Z$ are into WW- and ZZ pairs; whereas for the intermediate mass range ($80 \text{ GeV} < m_h < 2M_Z$) the allowed decays are into $\gamma\gamma$, $Z\gamma$, WW^* , ZZ^* , which will compete with the decays into fermion pairs generated at the 1-loop level.

The decay width into photon pairs can be written as:

$$\Gamma(h \rightarrow \gamma\gamma) = \cos^2 \beta \cdot \Gamma_{\text{SM}}^{\text{W}}(h \rightarrow \gamma\gamma),$$

where $\Gamma_{\text{SM}}^{\text{W}}$ denotes the W-loop contribution to the decay width of the Standard Model Higgs boson; the decay width for $h \rightarrow Z + \gamma$ has also the same form, and its value will be lower than for $h \rightarrow \gamma\gamma$, as in the Standard Model case. Similarly, we find that the decays into WW^* and ZZ^* can be written in the same form, namely [52]

$$\Gamma(h \rightarrow VV^*) = \cos^2 \beta \cdot \Gamma(\phi_{\text{SM}}^0 \rightarrow VV^*).$$

Finally, the expression for the decay width into fermion pairs ($h \rightarrow f\bar{f}$), resulting from the evaluation of the 1-loop amplitude is:

$$\Gamma(h \rightarrow f\bar{f}) = \frac{G_F \alpha^2 \pi}{2\sqrt{2} \sin^4 \theta_W} m_h m_f^2 \cos^2 \beta F(m_h, m_f, M_W),$$

where m_f is the mass of the fermion that enters in the loop, and $F(m_h, m_f, M_W)$ is a function that arises from the loop integration [53]. From this expression one notices that the width is again proportional to m_f^2 , which will suppress the width. Thus only the heaviest fermions will contribute significantly.

Fermiophobic Higgs bosons of the Higgs triplet models

It is possible that a non-minimal Higgs sector incorporates triplet fields. Particles formed exclusively from such fields are fermiophobic. The minimal Higgs Triplet model

[54] requires the inclusion of two triplet fields in order to have the ρ -parameter near unity. The model has ten Higgs bosons in the form of a fiveplet (H_5), a triplet (H_3), and two singlets (H_1). The H_5^0 and one of the singlets, H_1^0 , are formed from the triplet field, apart from possible mixing with the doublet components. Akeroyd [48] has shown that measurements constrain the mixing parameters such that H_1^0 is almost entirely fermiophobic, and therefore could be interpreted as the Higgs boson searched for in this thesis. The process $e^+e^- \rightarrow H_1^0 Z$ occurs at the Standard Model hZ rate modified by the factor $\frac{3}{8} \sin \theta_H$, where the angle θ_H is a parameter of the model describing the mixing of the doublet and triplet fields.

Other Higgs Triplet Models [55] predicts that one of the neutral scalars could have a large branching fraction $\text{BR}(h \rightarrow \gamma\gamma)$ and could be produced at LEP with rates comparable to the Standard Model ones through the $e^+e^- \rightarrow Zh$ mechanism.

Anomalous Higgs couplings

The Standard Model can be extended by a linear representation of the $SU(2)_L \times U(1)_Y$ symmetry breaking mechanism [56]. Although the specific theory which will supersede the Standard Model is not known, its effects can be parameterized by the means of an effective Lagrangian [57]. The effective Lagrangian contains operators with dimension higher than four and involves the fields and symmetries of the low energy theory. This approach is a model-independent way to describe new physics that is expected to manifest itself directly at an energy scale Λ , larger than the scale where the current experiments are performed.

A general set of dimension-6 operators that involve gauge bosons and the Higgs scalar field, respecting local $SU(2)_L \times U(1)_Y$ symmetry, and C and P conserving, contains eleven operators. Some of these operators can be strongly constrained from low energy physics below the present sensitivity of high energy experiments. The remaining five operators can be written as [58]:

$$\begin{aligned} \mathcal{L}_{\text{eff}} = \sum_i \frac{f_i}{\Lambda^2} \mathcal{O}_i = \frac{1}{\Lambda^2} & \left[f_{\text{WWW}} \text{Tr}[\hat{W}_{\mu\nu} \hat{W}^{\nu\rho} \hat{W}_\rho^\mu] \right. \\ & + f_{\text{W}} (D_\mu \Phi)^\dagger \hat{W}^{\mu\nu} (D_\nu \Phi) + f_{\text{B}} (D_\mu \Phi)^\dagger \hat{B}^{\mu\nu} (D_\nu \Phi) \\ & \left. + f_{\text{WW}} \Phi^\dagger \hat{W}_{\mu\nu} \hat{W}^{\mu\nu} \Phi + f_{\text{BB}} \Phi^\dagger \hat{B}_{\mu\nu} \hat{B}^{\mu\nu} \Phi \right], \end{aligned} \quad (2.41)$$

where Φ is the Higgs field doublet, and

$$\hat{B}_{\mu\nu} = i(g'/2)B_{\mu\nu} \quad \hat{W}_{\mu\nu} = i(g/2)\sigma^a W_{\mu\nu}^a,$$

with $B_{\mu\nu}$ and $W_{\mu\nu}^a$ being the field strength tensors of the U(1) and SU(2) gauge fields respectively.

Anomalous $H\gamma\gamma$, $HZ\gamma$, HZZ and HWW couplings are generated by (2.8), which, in the unitarity gauge, are given by

$$\begin{aligned} \mathcal{L}_{\text{eff}}^{\text{H}} = & g_{H\gamma\gamma} H A_{\mu\nu} A^{\mu\nu} + g_{HZ\gamma}^{(1)} A_{\mu\nu} Z^\mu \partial^\nu H \\ & + g_{HZ\gamma}^{(2)} H A_{\mu\nu} Z^{\mu\nu} + g_{HZZ}^{(1)} Z_{\mu\nu} Z^\mu \partial^\nu H \\ & + g_{HZZ}^{(2)} H Z_{\mu\nu} Z^{\mu\nu} + g_{HWW}^{(2)} H W_{\mu\nu}^+ W_{\nu\mu}^- \\ & + g_{HWW}^{(1)} (W_{\mu\nu}^+ W_{\nu\mu}^- \partial^\nu H + h.c.), \end{aligned} \quad (2.42)$$

where $A(Z)_{\mu\nu} = \partial_\mu A(Z)_\nu - \partial_\nu A(Z)_\mu$. The effective couplings $g_{H\gamma\gamma}$ and $g_{HZ\gamma}^{(1,2)}$ are related to the coefficients of the operators appearing in (2.9) through

$$\begin{aligned} g_{H\gamma\gamma} = & -\frac{gM_W \sin^2 \theta_W}{2} \left(\frac{f_{\text{WW}}}{\Lambda^2} + \frac{f_{\text{BB}}}{\Lambda^2} \right), \\ g_{HZ\gamma}^{(1)} = & \frac{gM_W \sin^2 \theta_W}{2 \cos \theta_W} \left(\frac{f_{\text{W}}}{\Lambda^2} - \frac{f_{\text{B}}}{\Lambda^2} \right), \\ g_{HZ\gamma}^{(2)} = & \frac{gM_W \sin^2 \theta_W}{\cos \theta_W} \left(\sin^2 \theta_W \frac{f_{\text{BB}}}{\Lambda^2} - \cos^2 \theta_W \frac{f_{\text{WW}}}{\Lambda^2} \right), \end{aligned}$$

where g is the SU(2)_L coupling constant and θ_W is the Weinberg angle.

A typical anomalous signature would be the observation of large $h \rightarrow \gamma\gamma$ and $h \rightarrow Z\gamma$ branching fractions which are zero in the Standard Model at the tree level. The existence of the new interactions (2.8) can enhance these widths in a significant way.

Anomalous Higgs boson couplings have been studied in Higgs and Z boson decays [59], and in e^+e^- [60], $p\bar{p}$ [61] and $\gamma\gamma$ [62] colliders. Recent analyses from L3 presented a good agreement with the expectations from the Standard Model [63]. These negative experimental results can be used to constrain new anomalous couplings in the bosonic sector of the Standard Model.

Other models

Another example having suppressed couplings to the fermions is an electroweak Higgs boson h_{ew}^0 added to top-quark condensate models [64]. In this approach, the top and bottom quarks are assumed to obtain their masses through a strongly coupled group that condenses top quark pairs [65]. All the remaining fermions and vector bosons obtain mass mainly through the vacuum expectation value of the h_{ew}^0 . A good approximation in studying the phenomenology of a light h_{ew}^0 is to assume that it couples like the Standard Model Higgs to all particles except the top quark and bottom quark, to which it has zero couplings.

The benchmark fermiophobic model

As mentioned above, the fermiophobic models are parameter dependent, but a large class of the models has a near-Standard Model production strength and di-photon branching fractions well approximated by the Standard Model ones with fermionic couplings set to zero. This defines the so-called benchmark fermiophobic model.

All the LEP experiments are using the simulation program HZHA [66] to model the Higgs boson production. The branching fractions for the Higgs decays into boson pairs can also be calculated with the HDECAY program [43]. This program results in slightly lower di-photon branching fractions than HZHA. To be conservative we use the HDECAY branching fractions throughout this thesis. The branching fractions, calculated in the benchmark model, are shown in Figure 2.16.

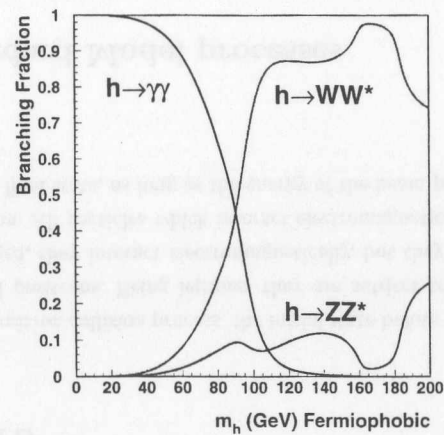


Figure 2.16: Branching fractions for the decay of the Higgs boson in the benchmark fermiophobic model: $h \rightarrow \gamma\gamma$ solid line, $h \rightarrow WW^*$ dashed line, $h \rightarrow ZZ^*$ dotted line. Calculations are done using the HDECAY program [43], with the fermionic couplings set to zero.

Chapter 3

Physics at electron-positron colliders

In an electron-positron collision process, the initial state before the interaction consists of electrons and positrons. Being leptons, they are subject to the weak interaction; being also charged, they interact electromagnetically, but they are not subject to the strong interaction. All particles which interact electromagnetically and weakly can be produced in the final state, as long as the energy of the beam particles which collide is sufficiently high.

3.1 Standard Model processes

Quark and lepton pair production are among the dominant processes at LEP2, which operated at centre-of-mass energies above 161 GeV. Fermion pairs can be produced in s-channel γ and Z exchanges. In an electron-positron electromagnetic annihilation, a virtual photon is produced, which immediately decays into a fermion anti-fermion pair. In the case of a weak interaction, the exchanged particle is the heavy vector boson Z^0 . The leading-order Feynman diagrams for fermion-pair production are presented in Section 3.1.1.

Pair production of charged bosons W^\pm proceeds through both the charged-current t-channel and the neutral-current s-channel. Pairs of the neutral bosons γ and Z can also be produced in e^+e^- interactions, via neutral-current t- and u-channel interactions. Each of the vector bosons can decay to a fermion anti-fermion pair, $f\bar{f}$, thus leading to a four-fermion final state.

The cross sections for some typical standard model processes as a function of the centre-of-mass energy are presented in Figure 3.1. The Z boson resonance leads to a sharp enhancement of the cross section, up to 30 nb at the pole $\sqrt{s} = M_Z$.

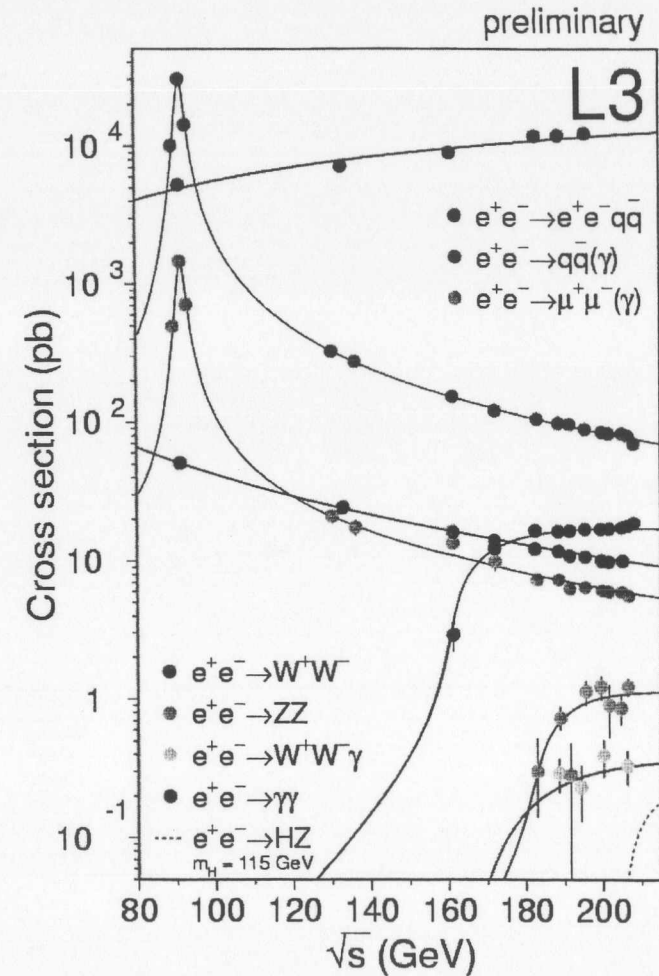


Figure 3.1: Cross sections for typical standard model processes as a function of centre-of-mass energy.

The production of Z-pairs and W-pairs occurs with a much smaller cross section, of the order of 1 pb and 20 pb, respectively. The energy dependence shows the expected

threshold behavior at $\sqrt{s} = 2M_W$ and $\sqrt{s} = 2M_Z$. Some of these processes can be considered as potential backgrounds for the Higgs boson search. Therefore it is very important to know as precisely as possible the expected yield for these reactions. A list of Monte Carlo event generators which are used in the simulation of the standard model processes is given in Table 3.1.

| Simulated process | MC-event generator | Cross section at $\sqrt{s}=206.6$ GeV (pb) |
|--|--------------------------------|--|
| $e^+e^- \rightarrow W^+W^- \rightarrow f\bar{f}\bar{f}$ | KORALW [67], YFSWW3 [69] | 17.5 |
| $e^+e^- \rightarrow f\bar{f}\bar{f}$ | EXCALIBUR [68] | 0.3 |
| $e^+e^- \rightarrow \nu\nu\gamma(n\gamma)$ | NUNUGPV, [70],[71] KORALZ [72] | 54.6 |
| $e^+e^- \rightarrow q\bar{q}(\gamma)$ | KK2F [73], PYTHIA [74] | 81.0 |
| $e^+e^- \rightarrow Z^0/\gamma Z^0/\gamma \rightarrow f\bar{f}\bar{f}$ | PYTHIA [72] | 1.33 |
| $e^+e^- \rightarrow \gamma\gamma \rightarrow eeq\bar{q}$ | PHOJET [75] | 16410. |
| $e^+e^- \rightarrow \gamma\gamma \rightarrow ee\ell^+\ell^-$ | DIAG [76] | 705. |
| $e^+e^- \rightarrow \gamma\gamma \rightarrow ee\tau^+\tau^-$ | LEP4F [77] | 435. |
| $e^+e^- \rightarrow e^+e^-(n\gamma)$ | BHWIDE [78] | 1284.8 |
| $e^+e^- \rightarrow e^+e^-(n\gamma)$ | TEEGG [79] | 31.9 |
| $e^+e^- \rightarrow \mu^+\mu^-(n\gamma), \tau^+\tau^-(n\gamma)$ | KK2F [73], KORALZ [72] | 6.3 |
| $e^+e^- \rightarrow (n\gamma)$ | GGG [80] | 18.3 |

Table 3.1: Monte Carlo event generators for e^+e^- physics.

3.1.1 The two-fermion process

Two-fermion processes are the production of an electron-, muon-, tau- and a quark anti-quark pair from a Z or virtual photon, for example: $e^+e^- \rightarrow Z^*/\gamma^* \rightarrow q\bar{q}(\gamma)$. The γ denotes any initial-state-radiation (ISR) photons from the electron or positron. The lowest order diagrams contributing to this process are shown in Figure 3.2. The additional Feynman diagrams for the case of t-channel γ and Z exchanges or W exchange are shown in Figure 3.3.

Two-fermion reactions were the dominant physics processes at LEP1 with a large cross section (up to 30 nb for the hadronic final state) due to the centre-of-mass energies being close to M_Z . As the centre-of-mass energy increases towards the LEP2 region, this cross section decreases rapidly. At a centre-of-mass energy of 206.6 GeV, the magnitude of the cross sections, apart from the Bhabha process and the $e^+e^- \rightarrow e^+e^-\bar{f}\bar{f}$, varies

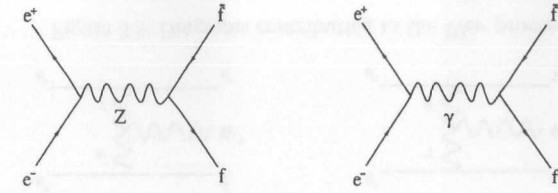


Figure 3.2: Diagrams contributing to the $e^+e^- \rightarrow Z^*/\gamma^* \rightarrow f\bar{f}$ process.

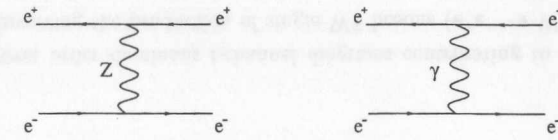


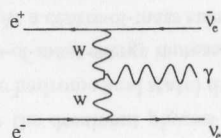
Figure 3.3: Diagrams contributing to the $e^+e^- \rightarrow e^+e^-$ process.

between 10 and 100 pb. The e^+e^- cross section is about 4 nb for the electron positron scattering angle in the interval between 5° and 175° . Roughly 65% of the $e^+e^- \rightarrow Z^*/\gamma^* \rightarrow q\bar{q}(\gamma)$ process consists of radiative returns to the Z. This refers to the case when a hard ISR photon from the electron or positron boosts the effective centre-of-mass energy of the colliding system back, close to M_Z (denoted $q\bar{q}(\gamma)$). The ISR photon typically has low transverse momentum; it can escape undetected along the beam pipe traversing the experimental setup and the resulting event will have missing energy; or, it could be detected as an isolated energy deposit in a detector and the resulting event will have little missing energy. In the case no ISR photon is emitted the visible mass of the event is near the centre-of-mass energy.

Radiative $e^+e^-(\gamma)$, $\mu^+\mu^-(\gamma)$ and $\tau^+\tau^-(\gamma)$ events are backgrounds to the Higgs boson search in the low multiplicity $hZ \rightarrow \gamma\gamma\ell^+\ell^-$ channel, with $\ell = e, \mu, \tau$. The $q\bar{q}(\gamma)$ events contaminate the hadronic $hZ \rightarrow \gamma\gamma q\bar{q}$ event topology.

The radiative neutrino standard model process constitutes an irreducible background for the search in the $hZ \rightarrow \gamma\gamma\nu\bar{\nu}$ final state. A diagram contributing to the neutrino pair production in association with a photon is shown in Figure 3.4.

The two-fermion process and the measurements based upon it are described in detail elsewhere [81].

Figure 3.4: Diagram contributing to the $e^+e^- \rightarrow \nu\bar{\nu}(\gamma)$ process.

3.1.2 The two-photon process

The process in which virtual photons from the incoming electron and positron form a fermion anti-fermion pair is referred to as the two-photon or $\gamma\gamma$ process, although it is actually a four-fermion process. A lowest-order diagram contributing to this process is shown in Figure 3.5.

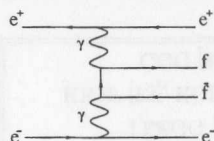


Figure 3.5: Diagram contributing to the two-photon process.

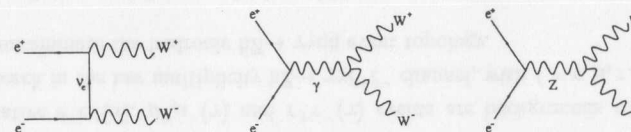
We call a $\gamma\gamma$ event un-tagged if both the electron and positron escape along the beam pipe undetected. The majority of the $\gamma\gamma$ events are un-tagged. The hadronic cross section is highly dependent on the assumed kinematic features; it is about 10 nb when the invariant mass of the hadronic system is greater than 2.5 GeV. Although the cross section is large, these events are characterized by extremely low visible energy and particle multiplicity. Hence they are easily eliminated at early stages of the event selection procedure designed to search for the Higgs boson, and they do not constitute a significant source of background events.

The two-photon processes and related measurements are described in Ref. [82] in more detail.

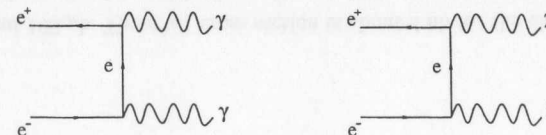
3.1.3 The four-fermion processes

The pair production of W^\pm bosons has a cross section of 17 pb at a centre-of-mass energy of 206.6 GeV. This process has two s -channel (γ and Z exchanges) and one t -channel (ν_e exchange) production mechanisms. Figure 3.6. shows diagrams contributing

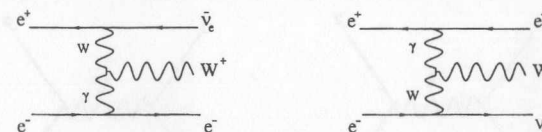
to these reactions. At energies near the $2M_W$ threshold, the t -channel diagram dominates. This process and measurements associated with it are described in detail in Ref. [83].

Figure 3.6: Diagrams contributing to the W^+W^- process.

The four-fermion process involving the pair production of Z bosons includes the processes $e^+e^- \rightarrow \gamma\gamma$ and ZZ (shown in Figure 3.7), and $e^+e^- \rightarrow Z\gamma$. Below $2M_Z$, this process results in only one on-shell Z ; thus it can resemble the two-fermion $q\bar{q}(\gamma)$ process. Details can be found in Ref. [84].

Figure 3.7: Diagram contributing to the ZZ process.

The lowest order dominant t -channel diagrams contributing to the four-fermion processes involving the production of single W^\pm bosons ($e^+e^- \rightarrow W^\pm e\nu_e$, denoted as $We\nu$) and single Z bosons ($e^+e^- \rightarrow Ze^+e^-$, denoted as Zee) are shown in Figure 3.8 and 3.9, respectively. The cross sections at 206.6 GeV are 3 and 3.6 pb for $We\nu$ and Zee respectively. The $We\nu$ process is discussed in Ref. [85].

Figure 3.8: Diagrams contributing to the $We\nu$ process.

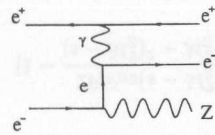


Figure 3.9: Diagram contributing to the Zee process.

Both of these last processes contain events which are characterized by a spectator electron or positron escaping undetected along the beam pipe. Hence, these events will have a large component of missing momentum in the z direction.

3.2 Higgs boson physics

3.2.1 Higgs boson production

The main production process of the Standard Model Higgs Boson at LEP energies is the so called Higgs-Strahlung, Figure 3.10 [86], [87]. In this reaction the electron and the positron annihilate into a virtual Z boson which then emits a Higgs boson. The cross section of this process is given by:

$$\sigma(e^+e^- \rightarrow Zh) = \frac{G_F^2 M_Z^4}{96\pi s} (\nu_e^2 + a_e^2) \lambda^{\frac{1}{2}} \frac{\lambda + 12M_Z^2/s}{(1 - M_Z^2/s)^2},$$

where \sqrt{s} is the centre-of-mass energy, $\nu_e = -1 + 4 \sin^2 \theta_W$ and $a_e = -1$ are the neutral current couplings of the electron and $\lambda = (1 - m_h^2/s - M_Z^2/s)^2 - 4m_h^2 M_Z^2/s^2$ is the two particle phase space function.

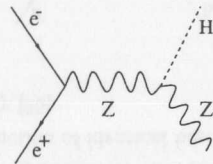


Figure 3.10: Higgs-Strahlung: The Higgs Boson is produced together with a Z Boson.

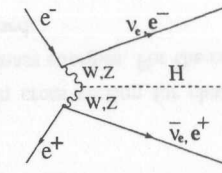


Figure 3.11: WW and ZZ fusion diagrams. They are suppressed by an additional power of the electroweak coupling constant with respect to the Higgs-Strahlung process.

Going to higher centre-of-mass energies, two more diagrams start to contribute: the WW and the ZZ fusion diagrams, Figure 3.11 [88], [89], [90], [91]. The cross sections for the Higgs-Strahlung and the fusion processes are shown as a function of the Higgs mass at $\sqrt{s} = 206.6$ GeV in Figure 3.12.

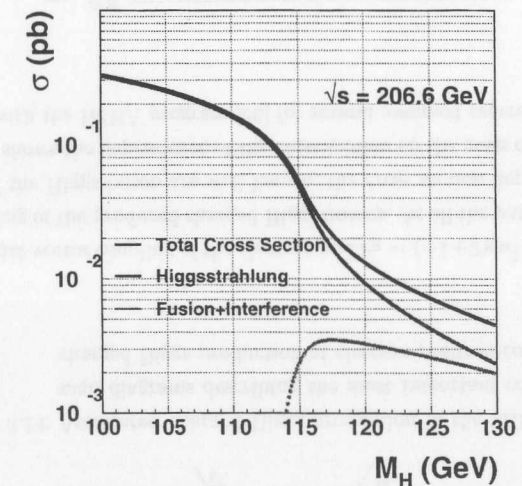


Figure 3.12: Higgs production cross section at $\sqrt{s} = 206.6$ GeV. The main production process is the Higgs-Strahlung $e^+e^- \rightarrow Zh$.

In Two Higgs Doublet Models, the Higgs-Strahlung process is complemented by

the associated pair production $e^+e^- \rightarrow Z \rightarrow hA$, Figure 3.13. The CP-odd Higgs boson A cannot be produced in Higgs-Strahlung at tree level because of C-invariance which forbids the ZZA coupling (however, this coupling can be generated through fermion loops) [42]. The production of identical bosons via the vertices hhZ and AAZ is forbidden by Bose symmetry [35].

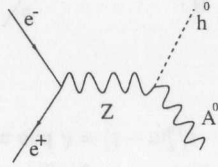


Figure 3.13: Associated pair production in the 2HDM. The CP-even Higgs boson h is produced together with the CP-odd Higgs boson A.

The production cross sections for the Higgs-Strahlung and the associated pair production can be parameterized in the following way [92]:

$$\begin{aligned}\sigma_{hZ} &= \sin^2(\beta - \alpha) \sigma_{hZ}^{\text{SM}}, \\ \sigma_{hA} &= \cos^2(\beta - \alpha) \bar{\lambda} \sigma_{hZ}^{\text{SM}},\end{aligned}$$

where σ_{hZ}^{SM} is the cross section for the Higgs-Strahlung in the Standard Model. The kinematic factor $\bar{\lambda}$ depends on m_h , m_A and \sqrt{s} .

Associated HZ production can kinematically occur only in a tiny corner of the parameter space for moderate to large $\tan\beta$ values and with a cross section which can be parameterized as following:

$$\sigma_{HZ} = \cos^2(\beta - \alpha) \sigma_{hZ}^{\text{SM}}.$$

The production of charged Higgs bosons at LEP is possible through s-channel Z and γ exchange, Figure 3.14. The production cross section at tree level is given by the following Eq. [93]:

$$\sigma(e^+e^- \rightarrow H^+H^-) = \frac{\pi\alpha^2}{3s} \left[1 - \frac{2\hat{\nu}_e\hat{\nu}_H s(s - M_Z^2)}{(s - M_Z^2)^2 + M_Z^2\Gamma_Z^2} + \frac{(\hat{a}_e^2 + \hat{\nu}_e^2)\hat{\nu}_H^2 s^2}{(s - M_Z^2)^2 + M_Z^2\Gamma_Z^2} \right] \hat{\beta}^3,$$

with $\hat{\beta} = (1 - 4m_{H^\pm}^2/s)^{1/2}$ being the velocity of the produced Higgs bosons, $\hat{\nu}_e = (1 - 4\sin^2\theta_W)/4\sin\theta_W\cos\theta_W$ is the vector coupling of the electron, $\hat{a}_e = -1/4\sin\theta_W\cos\theta_W$

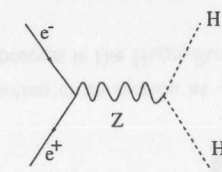


Figure 3.14: Associated charged Higgs production in the 2HDM. The Feynman diagrams describing the most important contributions to charged Higgs production at electron positron colliders.

is the axial-vector coupling of the electron and $\hat{\nu}_H = (-1 + 2\sin^2\theta_W)/2\sin\theta_W\cos\theta_W$ is the coupling of the produced charged Higgs bosons. As all the parameters apart from the mass of the Higgs boson are well known, the cross section depends only on m_{H^\pm} . Figure 3.15 shows the dependence of the cross section on the mass of the charged Higgs calculated with the HZHA program [66] for several assumed centre-of-mass energies.

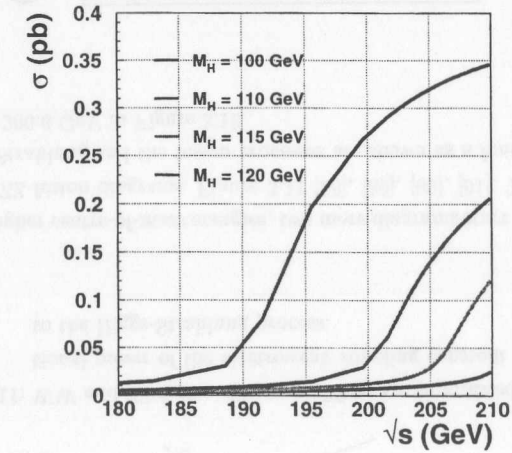


Figure 3.15: Production cross section for charged Higgs bosons at various centre-of-mass energies. For the calculation the program HZHA [66] was used.

Chapter 4

The Experiment

The Large Electron Positron (LEP) collider [94], the largest synchrotron storage ring with a circumference of 27 kilometers, is located at the CERN laboratory near Geneva, Switzerland (see Figure 4.1 for an aerial view).

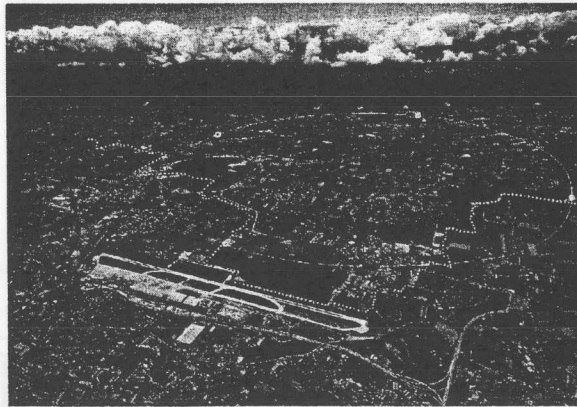


Figure 4.1: Aerial view of the foothills along the French Jura mountains, close to Geneva. This is the site of the Large Electron Positron collider (LEP).

Its main physics objective was the detailed study of the electroweak interaction, by performing precision measurements of the relevant physical quantities and by searching for unexpected features.

Free electrons and positrons can be produced rather easily. They can be accelerated, stored and made to collide in circular accelerators. Groups of electron and positrons, approximately 10^{12} in number, called bunches, circulate with the same energy, but

in opposite directions around the ring and are colliding head-on in the centre of four detectors, ALEPH, DELPHI, L3 and OPAL. In this kind of collisions all the beam energy is available in the centre-of-mass, $\sqrt{s} = 2E_{\text{beam}}$. The particle bunches define a luminous region called the beam spot.

The beam spot is squeezed in transverse plane by magnets near the detector to enhance the luminosity in the interaction region. It also provides a very precise transverse reference point for the origin of the annihilation event in x and y directions. Usually it has a Gaussian profile with the horizontal and vertical standard deviations $\sigma_x = 200 \mu\text{m}$ and $\sigma_y = 20 \mu\text{m}$, and a bunch length $\sigma_z = 1 \text{ cm}$.

The LEP research program started in August 1989 and continued until the year 2000. During its first phase, from 1989 to 1995, the machine operated at centre-of-mass energies close to the Z mass, $|\sqrt{s} - M_Z| < 3 \text{ GeV}$, in order to scan the Z resonance. During this phase each experiment collected about 160 pb^{-1} of integrated luminosity while peak luminosities of $10^{31} \text{ cm}^{-2}\text{s}^{-1}$ were reached. The second phase of the LEP program began in 1995, when the centre-of-mass energy was increased above the Z resonance to 130-140 GeV. Until the year 2000, the centre-of-mass energy increased gradually from the threshold of W-pair production, 161 GeV, to the maximum of 209 GeV, beyond the machine design specifications. To boost the energy of LEP's particles, from 1996 on, the machine was equipped with 288 superconducting radio-frequency cavities to accelerate the beams. At LEP2, peak luminosities of $10^{32} \text{ cm}^{-2}\text{s}^{-1}$ were reached and a total integrated luminosity of about 500 pb^{-1} was collected at each of the four experiments. The averaged integrated luminosity that LEP delivered to the experiments in the year 2000, its final year of running, is shown in Figure 4.2, while the integrated luminosities collected by the L3 experiment during the LEP2 phase are summarized in Table 4.1.

LEP was scheduled to be closed in September 2000 and dismantled to obtain space for the LHC proton collider to be built in the same tunnel. However, due to indications of the Higgs particle appearing as data started to accumulate above 206 GeV, the experimental program was extended by six weeks. In the combined results of the four LEP experiments the significance of the Higgs signal had reached 2.9σ , still below the level needed to claim a physics discovery.

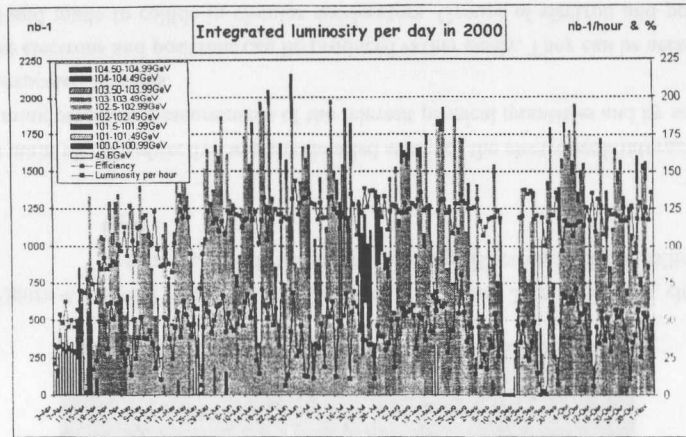


Figure 4.2: Integrated luminosity per day achieved by the LEP machine in 2000, as a function of time.

| Year | \sqrt{s} (GeV) | \mathcal{L}_{L3} (pb^{-1}) |
|------|------------------|----------------------------------|
| 1996 | 161 - 172 | 21 |
| 1997 | 183 | 55 |
| 1998 | 189 | 176 |
| 1999 | 192 | 29 |
| | 196 | 84 |
| | 200 | 83 |
| | 202 | 37 |
| 2000 | 204 | 8 |
| | 205 | 68 |
| | 206 | 67 |
| | 207 | 64 |
| | 208 | 8 |
| | 209 | 0.1 |

Table 4.1: The centre-of-mass energies and corresponding integrated luminosities collected by the L3 detector.

4.1 The Large Electron Positron collider

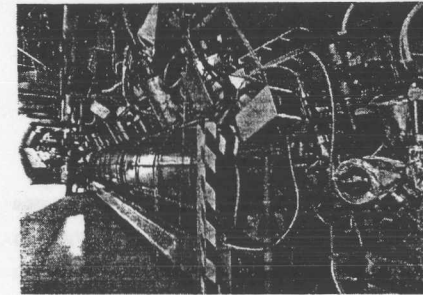


Figure 4.3: A superconducting RF cavity.

The Large Electron Positron machine [94] is situated about 100 m under the surface. It is formed by eight straight sections connected by curved sections to form a ring of 27 km circumference. The energy lost by synchrotron radiation in the curved sectors is proportional to E^4/R and, thus, determined by the energy and the curvature. The shape of the accelerator constitutes a balance between the amount of energy radiated in the curved sectors and its high construction cost.

The design energy of an accelerator is mainly determined by the physics goals. At LEP these were:

- high production rate of the Z bosons in its phase I;
- the production of W pairs in a second phase;
- the exploration of the highest possible energy regions, in the search for new physics.

The acceleration of electrons and positrons to beam energies of about 100 GeV requires a complex chain that uses the other accelerators available at CERN. The LEP accelerator chain is shown in Figure 4.4. The positrons are produced by the collision of 200 MeV electrons with a tungsten target. Electrons and positrons are then accelerated to 600 MeV at the LIL (Linear Injector LEP) and accumulated in the storage ring EPA (Electron Positron Accumulator). When the currents reach a certain value the beams are injected in the PS (Proton Synchrotron) where they are accelerated to a maximum energy of 3.5 GeV. Then they are transferred to the SPS (Super Proton Synchrotron) where they reach an energy of about 20 GeV. They are finally injected in the LEP and accelerated to the desired energy for the experimental program.

The acceleration is done in the straight sections of the tunnel using radio frequency cavities (see Figure 4.3 for a picture of a LEP superconducting radio-frequency cavity), while dipole magnets guide the beams through the curved sections. Once the final energy is reached the beams are focused in order to decrease their transverse size in the interaction regions. The focusing is performed by superconducting quadrupole and sextupole magnets located a few meters away from the interaction points.

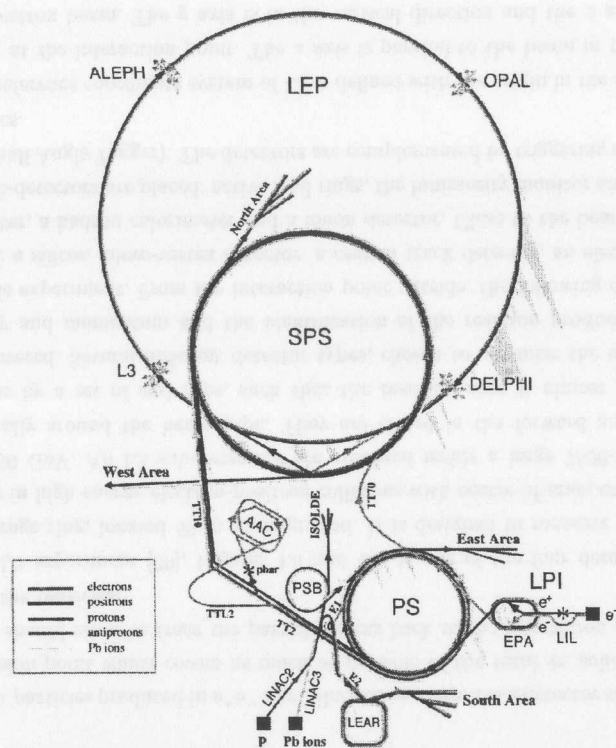


Figure 4.4: The LEP injection and acceleration chain, using several CERN accelerators.

4.1.1 Centre-of-mass energy measurement

The energy of the LEP beam is monitored and calibrated to very high accuracy [95]. Special calibration runs using a technique of resonant depolarization of a partially polarized electron beam can determine its energy to ± 0.6 MeV. The energy of a circulating particle is proportional to the precession frequency of its spin [96]. In the magnetic field of a storage ring the electron and positron spins polarize spontaneously due to synchrotron radiation in the transverse plane (Sokolov-Ternov effect [97]). The number of spin precessions per revolution around the storage ring, the spin-tune ν_s , is

given by

$$\nu_s = \frac{g_e - 2}{2m_e} E_{\text{beam}}$$

where g_e denotes the anomalous magnetic moment of the electron, m_e its mass and E_{beam} the beam energy, so it is directly proportional to the beam energy. The number of spin precessions per turn, the spin tune, is obtained by dividing the spin precession frequency by the revolution frequency. The spin tune is determined with the resonant depolarization technique. A kicker magnet generates a periodic perturbation to the beam and its spin, rotating the spin of the particles by a small amount of $140 \mu\text{rad}$ per revolution [98]. If the perturbation is in resonance with the spin precession a depolarization (sharp decrease or even reversal of the beam polarization) of the beam is observed.

The energy may vary over time, as external effects can influence either the dipole field or the beam position as it passes through the focusing quadrupoles. The dipole field strength and the beam position in the quadrupoles are monitored by a nuclear magnetic resonance (NMR) probe in a test dipole placed outside the tunnel but electrically in series with the LEP magnets, and by a beam orbit monitoring system. These systems have revealed beam energy fluctuations (at the 10 MeV level) due to both the gravitational pull of the moon and the water level of lake Geneva.

4.1.2 Luminosity measurement

Another important parameter in a collider experiment is the luminosity. The luminosity is defined as:

$$\mathcal{L} = f \cdot b \cdot \frac{n_e^2}{4\pi\sigma_x\sigma_y},$$

where n_e is the number of particles per bunch in the beams, b is the number of bunches, f is the revolution frequency and $\sigma_x\sigma_y$ is the beam size.

The total integrated luminosity can be computed according to the relation

$$\mathcal{L} = \frac{N_{\text{events}}}{\epsilon\sigma},$$

where σ is the cross section of a specific luminosity reaction, N_{events} is the measured number of events and ϵ is the selection efficiency. It is advantageous to use a well-known interaction with a high cross section, to keep both the theoretical errors on the calculation of σ and the statistical error of the luminosity measurement as small as possible. At e^+e^- colliders, the reaction typically used is Bhabha scattering, $e^+e^- \rightarrow e^+e^-(\gamma)$ at small polar scattering angles θ . In this region of phase space the Bhabha cross section is dominated by the t-channel exchange of a photon. The total cross

section in the polar angular range $0 < \theta_{\min} < \theta < \theta_{\max}$ is:

$$\begin{aligned}\sigma(\theta_{\min} < \theta < \theta_{\max}) &= \frac{16\pi\alpha_{em}^2}{s} \left(\frac{1}{\theta_{\min}^2} - \frac{1}{\theta_{\max}^2} \right) \text{ for } \theta_{\max} \ll 1 \text{ rad} \\ &= 0.125 \frac{M_Z^2}{s} \left(\frac{1}{\theta_{\min}^2} - \frac{1}{\theta_{\max}^2} \right) \text{ nb.}\end{aligned}$$

An error on the fiducial volume in polar angle translates into an error on the Bhabha cross section and thus on luminosity.

The experiments are equipped with dedicated luminosity detectors located at low polar angles, covering the angular range of $25 \text{ mrad} < \theta, \pi - \theta < 60 \text{ mrad}$. The accepted cross section of small angle Bhabha scattering for the luminosity measurement is of the order of 100 nb.

4.2 The L3 Detector

To detect particles produced in e^+e^- annihilations one requires a detector set up around the collision point which covers as much as possible of the total 4π solid angle. The detector should allow to trace the particle tracks back to the interaction point and to identify the particles.

The L3 experiment [99], Figures 4.5 and 4.6, is one of the four detectors at the LEP storage ring, located 50 m underground. It is designed to measure the reaction products in high energy electron-positron collisions with centre-of-mass energies up to about 200 GeV. All L3 sub-detectors are mounted inside a large 7800-ton magnet, cylindrically around the beam pipe. They are closed in the forward and backward directions by a set of end caps, such that the reaction zone is almost hermetically (99%) covered. Several different detector types, chosen to optimize the measurement of energy and momentum and the identification of the reaction products, make up the whole experiment. From the interaction point outside, the following detectors are installed: a silicon micro-vertex detector, a central track detector, an electromagnetic calorimeter, a hadron calorimeter and a muon detector. Close to the beam pipe three other sub-detectors are placed: active lead rings, the luminosity monitor and the VSAT (Very Small Angle Tagger). The detectors are complemented by triggering and read-out electronics.

The reference coordinate system of L3 is defined with the origin in the centre of the detector, at the interaction point. The z axis is parallel to the beam in the direction of the electron beam. The y axis is in the vertical direction and the x axis is in the horizontal direction pointing toward the centre of LEP. The entire apparatus has a cylindrical symmetry with respect to the beam axis.

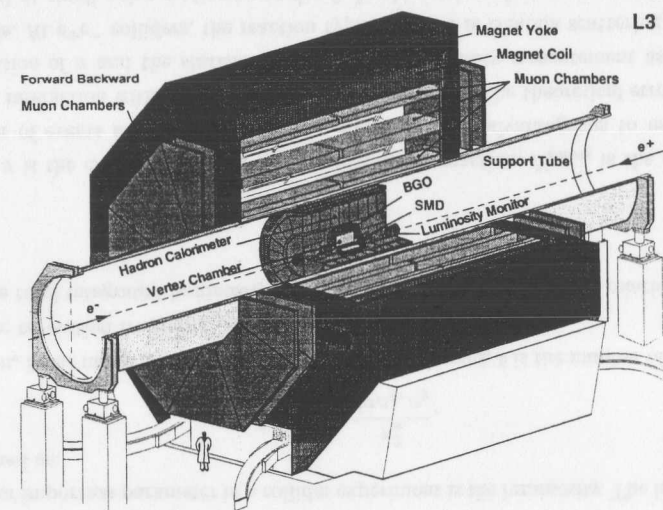


Figure 4.5: The L3 Detector. The detector is entirely inside the solenoidal magnet which produces a magnetic field of 0.5 T along the beam direction. Charged particles are detected in the vertex detector, mostly composed of silicon micro-strip counters, and in the drift chamber. The curvature of the tracks in the magnetic field allows for a momentum measurement. Photons and electrons are detected as shower formations in the electromagnetic calorimeter, while the hadrons are measured in the hadron calorimeter. Muons are seen in the exterior muon chambers.

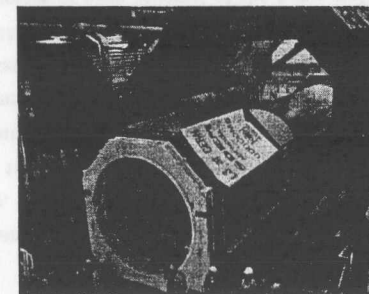


Figure 4.6: The L3 support tube, 32 m long and 4.45 m in diameter, containing the calorimeters and the inner tracking chamber.

The cylindrical coordinates are defined by the angle θ , the polar angle with respect to the z axis and the azimuthal angle ϕ in the $x-y$ plane (also called $r-\phi$ plane), measured starting from the positive x axis.

4.2.1 The central tracking system

The central tracking system consists of a Silicon Microvertex Detector (SMD), a Time Expansion Chamber (TEC) which provides tracking in the $r-\phi$ plane, a Z-chamber which measures the track z coordinate and Forward Tracking Chambers (FTC) in the endcap regions.

The Silicon Microvertex Detector (SMD)

The SMD [100] was installed in the L3 detector in the year 1993, to improve the track reconstruction capability. It is made of two layers of double-sided silicon micro-strips with a length of 35.5 cm. For a track produced by a charged particle, two points are measured, each with a coordinate in the $r-\phi$ plane and in the $r-z$ plane with a resolution of $7\ \mu\text{m}$ and of $14\ \mu\text{m}$, respectively. This improves by a factor of two the momentum resolution of the inner tracking system, because of the longer lever arm. The impact parameter can be improved by a factor of 5 if the alignment of the SMD with respect to the TEC is controlled with a precision of $10\ \mu\text{m}$. A resolution of $\sigma(1/p_t) = 0.011\ \text{GeV}^{-1}$ is achieved on the transverse momentum and of $30\ \mu\text{m}$ on the impact parameter. This detector is hermetic in ϕ and covers the θ angular region between 22° and 158° .

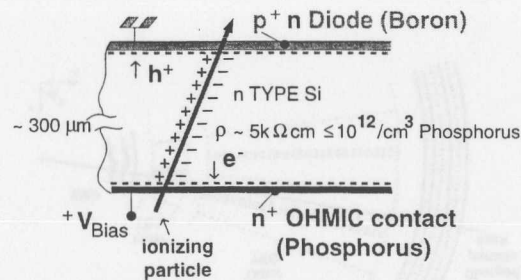


Figure 4.7: Schematic of an ionizing particle traversing an SMD wafer.

The basic detector element is shaped like a ladder and consists of four wafers. Each wafer is 70 mm long, 40 mm wide and made of $300\ \mu\text{m}$ thick n-type silicon. A schematic cross section through one of the wafers is shown in Figure 4.7. On one side (the junction side) are p-type (boron doped) implantation strips every $25\ \mu\text{m}$. The inner ladders have these strips parallel to the z axis, while the strips on the outer ladders are set at a 2° angle to the z axis to provide for the stereo reconstruction of the tracks. The p-type strips are used to measure the hit position in the $r-\phi$ plane. On the other side (the ohmic side) there are n⁺ (phosphorus doped) implantation strips perpendicular to the junction side strips. This side of the wafer measures the z coordinate.

A reverse bias voltage is applied to the wafer, with the n⁺ strips typically held at +50 V and the p strips at the ground potential, sufficiently for the n-type layer to be completely depleted. The residual dark current in the depleted wafer is less than $1\ \mu\text{A}$. If a charged particle passes through the silicon, it will interact and create electron/hole pairs as shown in Figure 4.7. After their creation the electrons and holes will drift under the applied electric field to the n⁺ and p strips, respectively. The position of the incident particle can then be determined by calculating a charge centre-of-gravity for neighboring strips where a non-zero charge has been measured.

The Time Expansion Chamber (TEC)

The Time Expansion Chamber [101] has been constructed to detect the charged particles and to measure the spatial coordinates of their trajectory in the magnetic field. It measures the transverse momentum and the sign of the charged particles with an energy up to 50 GeV and it reconstructs the interaction vertex, as well as the impact point and the direction of the charged particles at the beginning of the electromagnetic calorimeter.

The TEC has a cylindrical symmetry with a radius of about 50 cm and a length of 1 m. Due to size constraints imposed by the electromagnetic calorimeter, the TEC has a lever arm of only 37 cm available for the transverse momentum measurement. Since the L3 magnetic field is relatively low an excellent spatial resolution in order to achieve the design goal of charge identification for 50 GeV particles at 95% confidence level is necessary. A drift chamber design operating in the time expansion mode was the solution chosen. In this design the drift space is divided into two regions: the drift region with a low electric field and the amplification region with a high electric field, as illustrated in Figure 4.8. The TEC works with a gas mixture of CO₂ (80%) and C₄H₁₀ (20%) at a pressure of 1.2 bar, which guarantees a slow drift velocity of $6\ \mu\text{m}/\text{ns}$ and has a negligible Lorentz angle.

In Figure 4.9 the position of the wires in one TEC sector is shown. The inner chamber is divided in 12 sectors each of them containing 8 anode wires parallel to

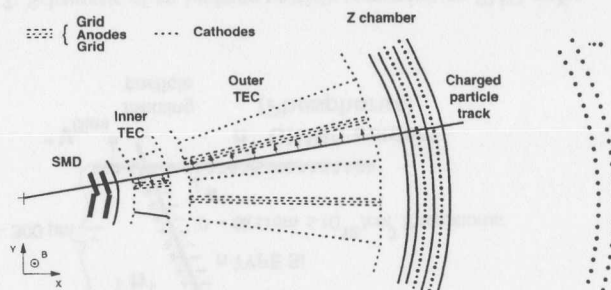


Figure 4.8: Drawing of the wire positions in a TEC sector.

the beam axis, to measure the $r - \phi$ coordinate to a precision of about $60 \mu\text{m}$. Two of the anode wires have charge division readout to determine the z coordinate to a precision of 2.5 cm . The outer chamber is divided in 24 sectors with 54 anode wires which measure the track coordinate with a resolution per single track of $50 \mu\text{m}$. The two track separation power is $450 \mu\text{m}$.

The TEC is completed by two cylindrical proportional chambers [102], with a cathode strip readout to measure the z coordinate in the angular range of $42^\circ \leq \theta \leq 138^\circ$. The cathode strips are oriented at 90° , 70.1° , -70.1° and 0° with respect to the beam direction. The resolution of the z measurement varies between $200 \mu\text{m}$ and 1 mm from the centre to the edges of the chamber.

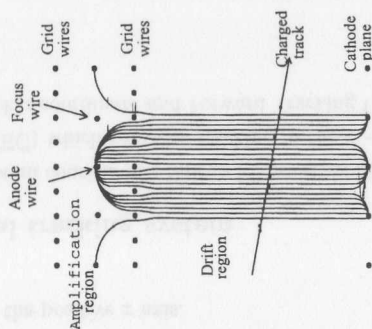


Figure 4.9: Amplification and drift regions in the TEC.

In front of the two endcaps are two tracking chambers (Forward Tracking Chambers) [103] to measure the position and the direction of charged particles at low angle. They have a spatial resolution smaller than $200 \mu\text{m}$.

Since the TEC has been made longer with respect to the original design, the FTC and the endcap BGO calorimeter are moved backwards, leaving an open region of about 5° between the barrel and the endcap calorimeters. This hole has been covered in 1995 with a new calorimeter called EGAP, which will be described later.

4.2.2 The electromagnetic calorimeter

The electromagnetic calorimeter (BGO) [104], shown in Figure 4.10, was designed to achieve good energy and spatial resolution for photons and electrons with energy between 100 MeV and 100 GeV . The calorimeter is made of bismuth germanate crystals ($\text{Bi}_4\text{Ge}_3\text{O}_{12}$) which are intrinsic scintillators with a small radiation length of 1.12 cm . Therefore an electromagnetic shower, even of 50 GeV of energy, is contained in a compact detector. The small transverse development of electromagnetic showers implies a high granularity for the detector, which is achieved with a small Molière radius material. The chosen geometry with $2 \times 2 \text{ cm}^2$ crystal front faces, allows for a good angular separation of nearby particles. The hadronic component of the event interacts rarely in the electromagnetic calorimeter because the BGO has only one interaction length. This allows a good π/e separation. The light yield of the crystals depends on their temperature, which must be kept at $18^\circ \pm 0.1^\circ$ with the help of a special cooling system. A map of the temperature is provided by sensors attached on the front and the rear crystal surface. This allows for the registration of the temperature of one crystal out of 12 and for a possible correction of the energy according to the observed variation.

The detector surrounds the central tracking system and it is divided in two parts: the **barrel**, which covers the angular region of $42.3^\circ \leq \theta \leq 137.7^\circ$ (corresponding to 74% of the total solid angle), and two **endcaps**, which the polar angle coverage of 10.6° to 36.7° in the forward and 142° to 168.4° in the backward direction. The crystals in the barrel point to the interaction region. They have the form of a truncated pyramid with a front surface of $2 \times 2 \text{ cm}^2$ and the back surface of $3 \times 3 \text{ cm}^2$. The crystals are 24 cm long corresponding to about 22 radiation lengths, and are fixed inside a support structure which makes two symmetric half barrels, each containing 3840 crystals - 160 crystals in ϕ and 24 in θ . In the endcaps, a number of 3070 crystals are distributed in 17 rings in θ , with a variable number of crystals per ring. Each endcap is subdivided in 16 sectors in ϕ . All the crystals in the calorimeter are supported by a carbon fiber structure which creates a very thin separation between the crystals ($200\text{-}250 \mu\text{m}$).

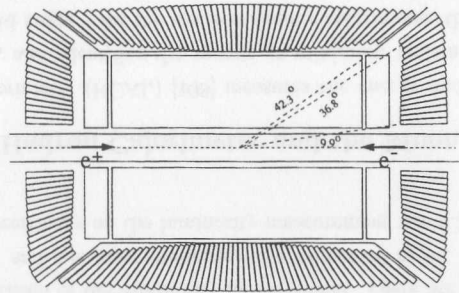


Figure 4.10: Schematic drawing of the crystal layout of the BGO electromagnetic calorimeter.

The scintillation light is collected by two photodiodes glued on the rear surface of each crystal. These Hamamatsu photodiodes have a quantum efficiency of roughly 70% around the emission peak (480 nm) of the BGO crystals. The photodiode produces a signal of 0.2 fC (1200 electrons) per MeV of deposited energy. This light is only a fraction of the total produced light, which is reflected many times on the sides of the crystal before reaching the photodiodes. A uniform light collection is obtained by modifying the reflecting properties of the crystal surface applying a layer of white paint with high diffusion power. The signal coming from the photodiodes is amplified by a preamplifier, glued on the rear crystal. The output signal has an amplitude of 50 $\mu\text{V}/\text{MeV}$, proportional to the collected charge (and therefore to the deposited energy), with a rise time of 300 ns and a decaying time of 800 μs . The first level of the electronics consists of analog-to-digital converters, near the crystals. The analog signal of the preamplifier passes through a shaping circuit which reduces the exponential tail from 800 μs to 1.2 μs . All information is here contained in the height of the signal.

The intrinsic resolution of the calorimeter is related to the poissonian fluctuations of the number of the particles which compose the shower. Since the number of produced particles is proportional to the energy of the incoming particle the intrinsic resolution is:

$$\frac{\sigma(E)}{E} = \frac{1.57\%}{\sqrt{E(\text{GeV})}} \oplus 0.35\%, \quad (4.2)$$

where \oplus signifies addition of the terms in quadrature.

Figure 4.11 shows the energy resolution of the BGO as a function of the energy.

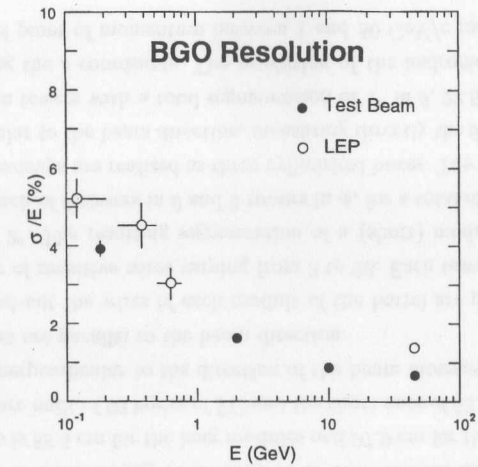


Figure 4.11: Energy resolution of the BGO barrel as a function of the energy, as measured during the test beam and at LEP.

The asymptotic behavior at high energy is represented by the constant term in Eq. 4.1, which also accounts for the calibration uncertainty [105]. The impact point resolution of an electromagnetic shower can be obtained by comparing the impact point measured in the BGO with the one measured with the TEC in the $r-\phi$ plane. At high energy the ϕ resolution σ_ϕ is 1.2 mrad (0.7 mm).

4.2.3 EGAP

The EGAP [106] detector is made of a lead structure filled with scintillating fibers (Figure 4.12). There are two rings, one for each gap, of 24 modules of trapezoidal form. The light is collected using two lucite light guides per module plus two photo-triodes. Some space is left between modules due to the presence of cables routed through EGAP from the TEC. To reduce the inefficiencies caused by this dead space the modules are not pointing to the interaction point. The length of the calorimeter is 0.72 cm which ensure a good shower containment (21 radiation lengths).

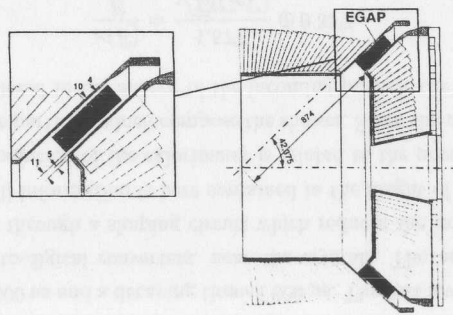


Figure 4.12: Longitudinal view of the EGAP detector.

4.2.4 The Luminosity Monitor

The luminosity monitor [107] is designed to measure the small angle Bhabha scattering events with an accuracy of the order of one permille. It consists of two BGO calorimeters and a silicon strip tracker. The calorimeters are situated symmetrically on each side of the interaction region at $z = \pm 2.7$ m, around the beam pipe and cover a polar angle region of $1.4^\circ \leq \theta \leq 3.9^\circ$ and $176.1^\circ \leq \theta \leq 178.6^\circ$, and the full ϕ angle. During unstable beam conditions, as during the LEP machine filling, the calorimeters are removed horizontally from the beam pipe to avoid radiation damage.

In 1993 a silicon strip tracker was mounted in front of the calorimeters in order to increase the precision of the luminosity measurement. There are two layers measuring the polar angle, and one layer measuring the azimuthal angle. In the year 2000 the experimental uncertainty on the luminosity measurement was 0.3 %.

4.2.5 The Hadron Calorimeter and the Muon Filter

The hadron calorimeter (HCAL) [108] measures the energy and the direction of the hadron showers, and identifies the muons as minimum ionizing particles. It covers 99.6% of the solid angle. Like the electromagnetic calorimeter, the hadron calorimeter (Figure 4.13) is divided into a barrel part, in the angular region $36^\circ \leq \theta \leq 144^\circ$, and two endcaps which cover the $5^\circ \leq \theta \leq 36^\circ$ and $144^\circ \leq \theta \leq 175^\circ$ polar angles.

The HCAL is a sampling calorimeter made of layers of depleted Uranium, as absorber, and proportional chambers (PC), operating with a mixture of Argon (80%) and

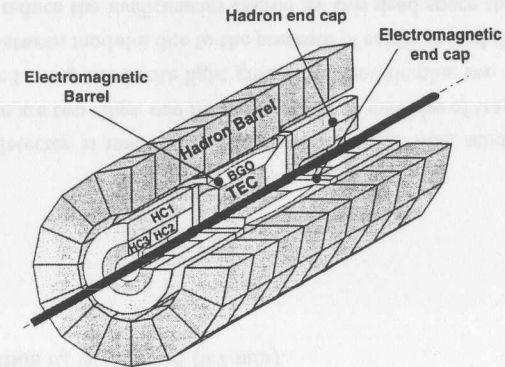


Figure 4.13: Schematic drawing of the hadron calorimeter.

CO_2 (20%), as detectors. They are calibrated with cosmic rays and with γ rays emitted by the uranium. The uranium was chosen because it has a small interaction length (≈ 10.5 cm), thus allowing for a very compact calorimeter. The signal of the chambers is proportional to the number of the charged tracks of a hadronic shower, which is, in turn, proportional to the energy of the incoming particle. The barrel is made of 9 rings (along z) each of them having 16 modules in ϕ . The external radius is 179.5 cm. The internal radius is 88.5 cm for the long modules and 97.9 cm for the short modules. The long modules are built of 60 layers of PC and the short ones of 53. Z chambers in which the wires are perpendicular to the direction of the beam alternate with ϕ chambers in which the wires are parallel to the beam direction.

For the read-out the wires of each module of the barrel are put together in towers with a number of sensitive wires varying from 3 to 28. Each tower covers a solid angle of about $2^\circ \times 2^\circ$. The resulting segmentation of a (short) module is of (8) 10 radial layers, made each of 9 towers in θ and 9 towers in ϕ , for a total of (114) 180 towers per module. The endcaps are realized as three cylindrical boxes. The wires of the chambers are perpendicular to the beam direction, measuring directly the θ coordinate. They are also grouped in towers with a total segmentation of 1° in θ , 22.5° in ϕ and 7 layers of chambers along the z coordinate. The resolution of the hadronic calorimeter, studied with a beam of pions of momentum between 1 and 50 GeV/c can be written as:

$$\frac{\sigma}{E} = \frac{55\%}{\sqrt{E}(\text{GeV})} \oplus 5\%.$$

The energy resolution of a $Z \rightarrow$ hadrons event, using only the electromagnetic and hadronic calorimeter information, is about 10%. The hadronic calorimeter is completed by a muon filter, in the space between the barrel calorimeter and the support tube. It is divided in octants. Each octant is made of 6 layers of brass absorber with a length of 1 cm, alternated with 5 proportional chambers of 1.5 cm. The filter adds one interaction length to the 4 of the hadronic calorimeter and to the one of the electromagnetic calorimeter making up a total of 6 interaction lengths. It is used to identify hadrons which do not interact in the electromagnetic calorimeter and which can fake a muon (the so-called punch-through).

4.2.6 The scintillator system

An array of 30 scintillators [109] is placed in the barrel between the electromagnetic calorimeter and the hadronic calorimeter to measure the time of flight of the particles. They cover the angular region of $25^\circ \leq \theta \leq 155^\circ$. The detectors are made of plastic scintillator bars with a thickness of 1 cm and a length of 2.9 m. The read out is done with phototubes. The time resolution is 1 ns, thus allowing to distinguish a cosmic muon passing near the interaction point from a muon produced in the events, as for $e^+e^- \rightarrow \mu^+\mu^-$. (A cosmic muon takes 5.8 ns to traverse the distance between two opposite counters).

4.2.7 Muon spectrometer

An important feature of the L3 detector is its muon spectrometer [110]. The entire central muon spectrometer is embedded in the solenoidal magnetic field.

The muon spectrometer has an octagonal shape and encloses the barrel hadron calorimeter. Each octant (an $r - \phi$ section is shown in Figure 4.14) consists of five drift chambers arranged in three layers: an inner layer (MI), an intermediate layer (MM) and an outer layer (MO). All three layers contain precision chambers, so-called "P-chambers", to measure the track coordinates in the $r - \phi$ plane.

The intermediate layer is made of two chambers which sample the track of the muon 24 times in the $r - \phi$ plane, while the inner and outer layers sample the track only 16 times. The inner and outer layers are surrounded by additional "Z-chambers", with the wires perpendicular to the beam direction to measure the z coordinate.

The spectrometer is built to measure the momentum of a 50 GeV muon with a resolution $\sigma(p)/p$ of 2%, which corresponds to a resolution of 1.4% on the reconstruction of the invariant mass of muon pairs from Z decays. The chambers have a single wire resolution of $200 \mu\text{m}$. The alignment of the chambers is controlled with a precise optomechanical system.

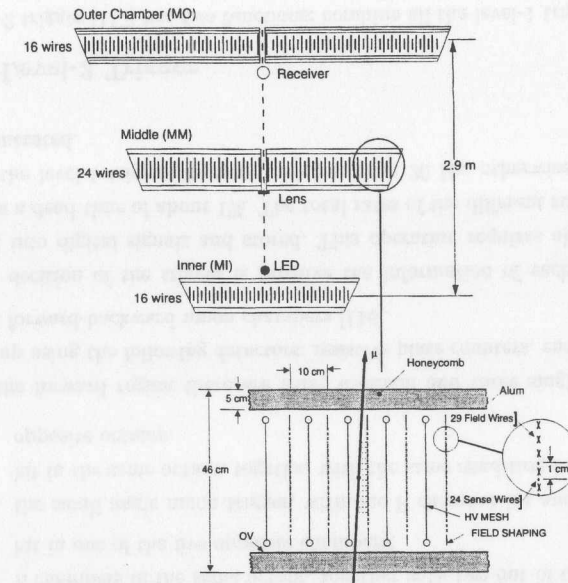


Figure 4.14: Drawing of the muon spectrometer.

Since 1995, the L3 experiment is equipped with forward-backward muon chambers in order to improve the momentum resolution in the angular region $36^\circ \leq \theta \leq 44^\circ$, and to allow the muon momentum resolution measurement down to 24° in θ . They are made of 96 drift chambers, divided into 16 sectors with three layers each on both sides of the detector [111].

4.2.8 The magnet

All sub-detectors are installed inside a large solenoid magnet made from welded aluminum plates with an inner radius of 6 m and a total length of 14 m. A 0.5 T field parallel with the z axis is provided by a 30 kA current carried by the coil.

The relatively low field compared to other experiments is balanced by a large field volume available for the momentum measurement. This solution was chosen to optimize the muon momentum resolution which improves linearly with the field and quadratically with the lever arm.

4.3 The L3 data acquisition system

The entire L3 detector consists of about 150000 read out channels. For each event their signals have to be digitized, the obtained data compressed and written to tape. The whole procedure takes about 500 μ s [112]. During the event processing, the read out channels are blocked and the detectors cannot record any new events. A trigger system is necessary to separate the physics events from the background events, allowing the acquisition of interesting data with a low dead time. The L3 trigger is divided in three different levels:

4.3.1 Level-1 Trigger

The level-1 trigger has less than the time gap between two bunch crossings of LEP to reject or accept an event. In case an event is rejected, the read out is stopped and all counters are reset to be ready for the next event. There are four sub-triggers which use special analog signals to reject an event:

- **The energy trigger** [113] combines signals from the electromagnetic and the hadronic calorimeters. It has an output rate of about 1-2 Hz. The 7680 crystals of the BGO barrel are put together in groups of 30 (5 in ϕ and 6 in θ) to have 256 analog signals. The endcaps, divided into 4 polar and 32 azimuthal segments, produce another 128 trigger signals each. To simplify the operations of the processor, the azimuthal segmentation is almost constant, therefore the grouping in θ and ϕ of the crystals in the endcaps is not uniform. For the hadronic calorimeter the trigger gets two signals per module, one corresponds to the chambers in the first interaction length, and the other for the remaining chambers.

Good events have to fulfil at least one of the following conditions:

1. the cluster trigger searches for energy depositions which form clusters in different detector layers. The threshold is 7 GeV if there is no TEC track and 3 GeV in the presence of a TEC track.
2. the total energy trigger requires at least 10 GeV in the BGO barrel alone or 15 GeV in the BGO and HCAL barrels, or 20 GeV in all the calorimeters including the endcaps;
3. the single photon trigger with a single isolated energy cluster in the BGO barrel greater than 2 GeV;
4. the hit counting trigger requires a minimum number of hits in the calorimeters, two trigger cells with more than 5 GeV;

5. the Bhabha trigger requires two back-to-back energy depositions larger than 15 GeV in two opposite luminosity detectors.

- **The TEC trigger** [114] reads 14 anode wires for each of the 24 sectors of the outer TEC chamber. Each sector is divided in 4 intervals in ϕ . The $r - \phi$ plane is therefore divided in 96 intervals in ϕ . An event is registered in a matrix of 96×14 bits. Software programmable masks recognize the tracks and count them. As the background rate peaks at low transverse momentum, p_t , the minimum p_t threshold is about 150 MeV. This trigger has a rate of about 2-6 Hz.
- **The scintillator multiplicity trigger** [109] requires that at least 5 pairs of scintillators to have a hit within ± 15 ns of the bunch crossing.
- **The muon trigger** [115] accepts events with a transverse momentum seen in the muon chambers larger than 1 GeV. It has a rate around 2-3 Hz, which does not change with the luminosity because it is dominated by cosmic events. It consists of three sub-triggers:

1. the single muon trigger, when two out of three P chambers and three out of four Z chambers in the same octant in the angular region $44^\circ \leq \theta \leq 136^\circ$ are hit;
2. the di-muon trigger, when two out of three P chambers are hit and one of the Z chambers in the same octant, together with two out of three P chambers hit in one of the five opposite chambers;
3. the small angle muon trigger, with one P chamber hit and one Z chamber hit in the same octant, together with the same condition in one of the three opposite octants.

In the forward region there are three di-muon and three single muon triggers set-up using the following detectors: resistive plate counters, endcap scintillators and forward-backward muon chambers [116].

If the decision of the trigger is positive the information of each sub-detector is converted into digital signals and stored. This operation requires about 500 μ s and introduces a dead time of about 1%. The total rates of the different sub-triggers which compose the level-1 trigger, have to be lower than 20 Hz, otherwise too much dead time is generated.

4.3.2 Level-2 Trigger

The level-2 trigger [117] has two functions: combine all the level-1 trigger information and reject the background events selected by only one level-1 trigger. Events accepted

by only one level-1 sub-trigger are more precisely analysed. During the level-2 processing, new information from the sub-triggers is available. The following algorithms are employed: the energy algorithm is based on a more precise energy estimation and rejects events with energy smaller than a predefined threshold. The TEC algorithm rejects electronic noise, beam gas events and events with tracks not pointing to the interaction point. The muon algorithm rejects muon events with a small number of hits in the vertex chambers and with no scintillator in time. If the event does not pass these requirements, the data transfer is stopped and the event is rejected. One rejected event out of 20 is kept in the data acquisition chain, to control the level-2 efficiency off-line. The level-2 trigger reduces the rate of the accepted events by a factor of about 10.

4.3.3 Level-3 Trigger

The fully digitized detector output is available for the level-3 trigger [118]. Before writing the event on tape the level-3 algorithm checks whether it is a good physical event or not. A further reduction factor of 10 on the number of accepted events is introduced by the level-3 trigger, by using several methods. Refined algorithms with tighter cuts are now used to reduce the event rate. The energy algorithm reconstructs energy in the electromagnetic and hadronic calorimeters using all the BGO crystals and HCAL information. As the calculations are based on a fine digitization, the thresholds are more precise with respect to the level-2 decision. The muon algorithm requires a muon track to have a scintillator hit within a time of ± 10 ns with respect to the beam crossing. The TEC algorithm reconstructs the TEC tracks and checks if they originate from the vertex. It controls also whether the tracks in the transverse plane are correlated with some energy deposit in the calorimeters or with hits in the scintillator counters. If an event passes the level-3 trigger (or at least two level-1 sub-triggers) it is written to tape.

4.4 The L3 offline software

4.4.1 Simulation; Monte Carlo generators

Monte Carlo event generators simulate e^+e^- interactions for various final states, distributed in phase space according to the Standard Model expectations or following another theoretical model.

The generated final-state particles are propagated through the detector simulation. The L3 experiment models the response of the detector with the detector simulation program GEANT [119], which includes the effect of energy loss, multiple scattering

and showering in the detector materials and in the beam pipe. Hadronic showers are simulated with the GHEISHA [121] program.

The response of the detector is accurately simulated with the program SIL3. SIL3 is based on the GEANT toolkit which tracks the particles generated by a Monte Carlo event generator from the interaction vertex through all detector materials in small steps. The structure of SIL3 can be described by its three phases:

1. the initialization consists mainly in the description of the geometry and of the materials of the L3 detector.
2. the tracking of a particle is done integrating the equations of motion step by step. The particle is propagated according to the properties of the material encountered determining with random numbers if and which interaction process is present at each step. When the energy of a particle becomes smaller than a predefined value the tracking is stopped. The value of this cut is chosen as a function of the requested accuracy, and of the available computing time.
3. the digitization phase, when the response of each part of the detector is calculated, introducing all details, for example the saturation of the electronics, the fluctuations of the pedestals, the radioactivity of the uranium. To achieve such a detailed description, a good knowledge of the behavior of the detector is necessary, obtained by a continuous comparison with real data.

4.4.2 Reconstruction

The event reconstruction [122] transforms the digitized raw data, i.e. the ADC and TDC signals, into higher level objects as for example tracks, energy deposits or jets. Analyses take place by comparing simulated and real events in terms of these high-level objects, in order to extract information about the underlying physics processes. In the following some standard quantities within the L3 reconstruction context are listed. Specific criteria used in selecting or counting these quantities are also given.

The first time the events are reconstructed, in the so called PASS1, the measured calibration constants are applied. Information from different sub-detectors are combined together to form a final reconstructed particle or a group of particles (jets). The events have to fulfil some selection criteria (PASS1 selection) in order to classify them in different physics categories or streams defined by the different analysis groups. The cuts applied in the first step are very loose to make sure that no interesting physics events are lost. The data after PASS1 are used to produce more precise calibrations and to check the consistency of the data. Final physics analyses are done after a PASS2 reconstruction, where final calibrations are applied.

The L3 database, where static and time dependent information about the detector is stored, has seven sections, one for each sub-detector. The information comes from different sources: general setups like the geometry of the detector, which are updated every year, and when new sub-detectors are added; data coming from the online monitoring system, as for example BGO temperatures and pedestals, or TEC high voltage, etc; off-line information, as for example calibration constants like TEC calibration of drift velocity and Lorentz angle, BGO energy calibration and dead crystals.

Tracks

Tracks are constructed out of hit wires in the central tracking chamber TEC. A fit is performed in order to extract from the coordinates of the hits the parameters of each track, including the curvature $1/R$ ($R \propto p_{\perp}$), distance of closest approach (DCA) of the track to the vertex, and angles ϕ and θ of the track at the vertex. The principal track parameters typically considered are: number of hits on the track, span (track length), DCA of the track, momentum of the track and the χ^2 of the track fit. In the context of this analysis a TEC track must satisfy all the following requirements in order to be accepted: at least 20 hits on the track, a span in radial direction of at least 30 wires, at most a DCA of 10 mm, and a minimal transverse momentum of 100 MeV.

Bumps

The map of crystals of the BGO calorimeter in θ and ϕ is searched for local maxima of at least 40 MeV in energy depositions, which form the seeds for constructing the so-called bumps. In an iterative procedure, crystals with energy greater than 10 MeV are assigned to the nearest bump, whenever they are geometrically connected to it and are not closer to any other bump. For each bump formed this way, the centre of gravity and the following quantities are constructed: sum of one, Σ_1 , defined as the energy of the central crystal, which is the most energetic one; sum of nine, Σ_9 , obtained adding the sum of the energy of the central crystal to the energies of the 8 crystals in the ring around it; sum of twenty-five, Σ_{25} , obtained adding to Σ_9 the energies of the 16 crystals in the ring around it (an electromagnetic particle, as an electron or a photon, delivers 91% of its energy in a 3×3 crystal matrix and 97% in a 5×5 crystal matrix).

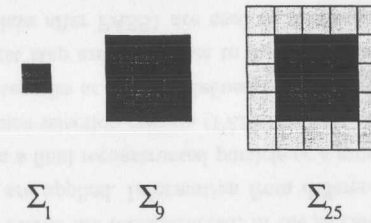


Figure 4.15: Σ_1 , Σ_9 and Σ_{25} . More details are given in the text.

A schematic drawing of these three objects is shown in Figure 4.15.

These sums are corrected for the lateral energy loss (leakage) in the following way:

$$\Sigma_9 \rightarrow \frac{\Sigma_9}{a_1 \cdot \frac{\Sigma_9}{\Sigma_1} + a_2}$$

$$\Sigma_{25} \rightarrow \frac{\Sigma_{25}}{b_1 \cdot \frac{\Sigma_{25}}{\Sigma_1} + b_2},$$

where a_1 , a_2 , b_1 and b_2 are correction constants.

The ratio Σ_9/Σ_{25} is then calculated, which represents an important variable to discriminate electromagnetic from hadronic particles. Another variable to evaluate the electromagnetic properties of the bump is χ_{em}^2 ; it is the result of the comparison between the energy distribution deposited in a 3×3 crystal matrix and the expected one for an electromagnetic particle.

Clusters

Matching bumps with geometrically connected hits in the hadron calorimeter located behind the BGO bumps leads to a formation of calorimetric clusters. Typical quantities to be considered are: all of the bump quantities listed above, energy (BGO, hadronic or total) and shower shape of the hadronic part. In the context of this analysis a cluster must satisfy the following requirement in order to be counted: BGO energy larger than 100 MeV and hadron calorimeter energy larger than 0.9 GeV.

Muons

Tracks reconstructed in the muon chambers, having at least two segments reconstructed in the precision chamber layers, such that a momentum measurement is possible, are called muon candidates, although there is some probability that these tracks might have been created by punch-through. Relevant track parameters are: number

of segments on the track (P or Z chamber), momentum of the track (transverse or total), distance-of-closest-approach after tracking and time of flight measured by the associated scintillator.

Jets

A jet can be defined as a collection of hadrons moving in approximately the same direction, originating from the decay fragmentation of a hard parton. When high energetic quarks or gluons tend to separate from each other the increasing strength of the color field polarizes the vacuum and creates a succession of quark-antiquark pairs, which combine into a narrow jet of hadrons around the original parton direction. The sum of the four momenta of the hadrons is generally referred to as the four momentum of the jet, which is then considered to be a pseudo-particle representing the original parton. Jets are reconstructed using algorithms joining together the reconstructed objects in the detector in an iterative procedure: first a set of objects in the event and a function or metric y_{ij} have to be chosen; then for each object pair ij the y_{ij} metric is calculated and the pair ij with the smallest value of y_{ij} is combined into a pseudo-particle which replaces the two objects. The iterative process continues until either the desired number of jets is reached, or the minimum metric y_{ij} between all pairs of jets is larger than a preset cut-off y_{cut} . The different methods used to determine which objects to combine together, all assume that objects separated by small angles or having low momentum with respect to each other belong to the same original parton. The most commonly used algorithms are: JADE [123], LUCLUS [124] and DURHAM [125].

In the analysis described in this thesis the events were clustered into jets using the Durham jet algorithm. In the Durham algorithm the distance

$$y_{ij} = 2\min(E_i^2, E_j^2)/E_{vis}^2 \cdot (1 - \cos \alpha_{ij})$$

is computed for all pairs of particles (i, j) . $E_{i,j}$ are the energies of the particles, α_{ij} is the opening angle and E_{vis} is the visible energy in the event.

Another jet clustering algorithm, which is better suited for the reconstruction of jets originating from tau decay, is the geometrical cone algorithm [126]. In this method objects are clustered simply according to their angular separation, which must be less than a given cone opening angle.

Characterizing quantities are: energy of the jet (total, calorimetric or muon), thrust [127] of the jet, invariant mass of the jet and multiplicity of the jet (cluster, track or muon). The general reconstruction program calculates all these quantities and selectively many more, thus providing a flexible framework for the data analysis.

The reconstruction program REL3 has a graphical event presentation, as shown in Figure 4.16 for a $e^+e^- \rightarrow q\bar{q}e\nu$ event, where the tracks are represented by lines, the

energy deposits by towers in the BGO and the squares in the HCAL; the dimension of the towers and squares is proportional to the energy deposited. In this figure the isolated electron is represented by a track in the TEC matched with a bump in the BGO, and the two jets are constituted by narrow bundles of hadronic particles pointing to the same direction.

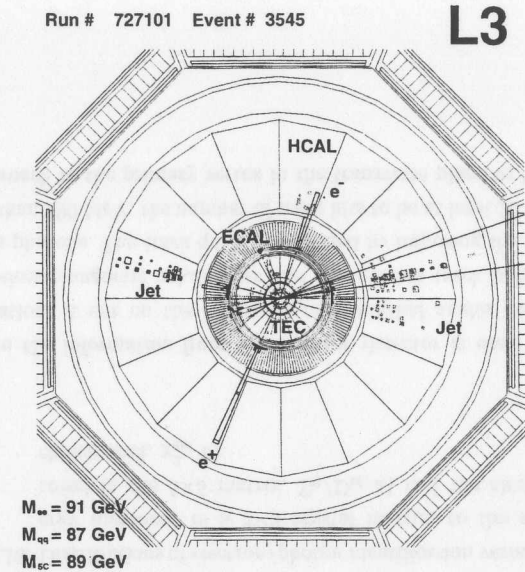


Figure 4.16: Example of a candidate event.

The tracks are represented by lines, the energy deposits by towers in the BGO and the squares in the HCAL; the dimension of the towers and squares is proportional to the energy deposited. In this figure the isolated electron is represented by a track in the TEC matched with a bump in the BGO, and the two jets are constituted by (narrow) track bundles of hadronic particles pointing into the same direction.

4.4.3 Particle identification

The mass and the charge of a particle generally suffice to identify it. The sign of a particle's charge can be read off from its deflection in a magnetic field. A direct measurement of the mass is in most of the cases impossible. There is therefore no general particle identification recipe and many different methods are available. In the following, the methods used in L3 for particle identification are listed. Short lived particles can be identified from their decay products with the help of the invariant mass method. The presence of neutrinos can be inferred from the momentum balance: the deficit of energy or momentum in the reaction is ascribed to the neutrino.

Electron and photon identification

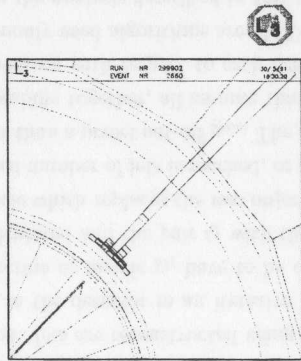


Figure 4.17: Schematic view of a reconstructed electron, showing one track in the central tracking chamber matched with energy deposition in the electromagnetic calorimeter; the leakage in the hadron calorimeter behind the bump is also visible .

Electrons and photons are recognized through their characteristic electromagnetic showers in the calorimeters (a schematic view is shown in Figure 4.17). We can distinguish between them with the help of the tracking detector in front of the calorimeter; only the electron will leave an ionization trail.

To distinguish electrons traversing the L3 detector from hadrons the characteristics of their interaction in the BGO are used. For a few particles which escape detection in the BGO (because they pass through the calorimeter in between the BGO crystals in the carbon fiber support structure), the energy deposition in the HCAL is also considered for identification. Signals in the muon filter and muon chambers are used as an electron veto. As mentioned before, a cluster in the electromagnetic calorimeter is characterized by its shape using the ratio Σ_9/Σ_{25} and the electromagnetic chi-squared χ_{em}^2 .

For an electromagnetic particle, Σ_9/Σ_{25} , after correction, peaks at 1 and it is cut at 0.95. Typical distributions for the Σ_9/Σ_{25} and χ_{em}^2 quantities are shown in Figure 4.18.

The energy measured in the hadron calorimeter behind the electromagnetic bump should not exceed 20% of the measured in the electromagnetic calorimeter.

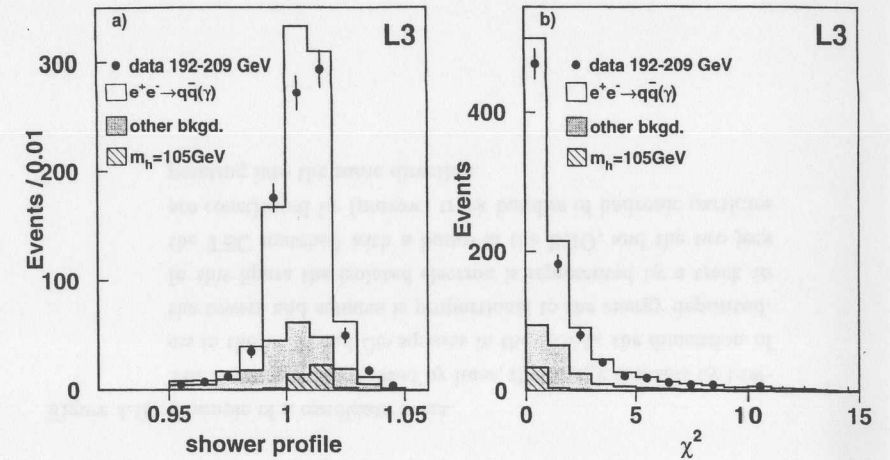


Figure 4.18: Distributions of electron/photon identification variables, the energy measured in a 3×3 crystal matrix, to the energy measured in the 5×5 matrix, Σ_9/Σ_{25} a) and the electromagnetic chi-squared, χ_{em}^2 b).

In addition the information from the tracking detector is used for the electron-photon separation. A cut on the difference of azimuthal angles between the bump in the BGO electromagnetic calorimeter and the nearest track helps to disentangle electrons from photons. The track quality is insured by imposing the track momentum to be greater than 100 MeV, the number of track hits to be at least 20 and the distance-of-closest-approach to the primary vertex in the transverse plane to be below 10 mm.

Muon identification

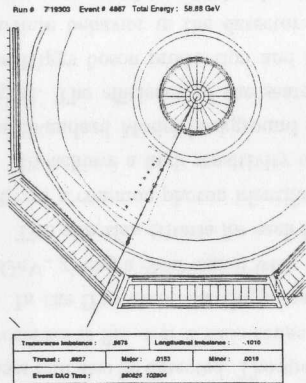


Figure 4.19: Schematic view of a reconstructed muon.

Muons are identified by their exceptional penetrative power. They primarily lose energy by ionization and can be detected with the help of the muon chambers placed outside where no other charged particle reaches. Therefore muons are identified by the presence of a track in the muon chambers (Figure 4.19).

To identify muons information from all sub-detectors is used. There are two ways of identifying muons in L3:

- one method uses only on the muon chamber information and accepts all particles, if there is a muon chamber track. The track has to point to the vertex. Muons from cosmic showers or hadronic punch-through do not usually point to the vertex. The muon track must have hits in at least two out of the three layers of the muon chamber. The muon identification requires some quality criteria to be satisfied for the muon momentum, the distance-of-closest-approach to the interaction vertex (DCA) and for the reconstructed time-of-flight with the scintillators: the muon momentum must be greater than 3 GeV, the track DCA in the plane perpendicular to the beam pipe should be less than 300 mm and along the beam pipe less than 400 mm. To ensure that the muons were created during the beam collision the time-of-flight must be within a 5 ns time interval around the bunch crossing time.
- in detection regions which are not covered by the muon chambers, the muon selection requires only one track per hemisphere detected by the TEC, and then uses the characteristics of the energy deposition of the minimum ionizing particle in the calorimeters. Muon candidates are required to have less than 5 BGO crystals associated with its track. In the hadron calorimeter the energy of the tower which was hit by a particle and its direct neighbors, E_{obs} , is added and compared with the expected energy for a minimum ionizing particle, E_{mip} , in these HCAL towers. Since one expects almost all energy deposited in the central tower for a muon, this distribution peaks at zero. Additionally one can cut on the remaining energy of the HCAL cluster, E_{rem} , which is not contained in E_{obs} . This energy must be less than 1 GeV for a muon candidate. Another useful criterion to select

muons is the difference between the total energy in both calorimeters normalized to the track momentum measured in the tracking chamber, which should be lower than 0.4.

Tau identification

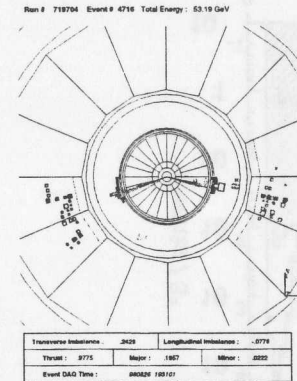


Figure 4.20: Schematic view of a $e^+e^- \rightarrow \tau^+\tau^-$ event, showing two hadronic tau decays with tracks reconstructed in the central tracking chamber and energy depositions in the calorimeters.

Due to the short lifetime of the tau leptons only their decay products are observed in the detector. These decay products are electrons and muons, for the leptonic decay modes, and charged and neutral mesons, for the hadronic decay modes of the tau lepton. All decays are accompanied by neutrinos, which escape detection. Therefore, the total energy of all detectable decay particles is distributed over a wide energy range. Furthermore, a tau decay is characterized by a single charged track or a low multiplicity jet with less than or equal to 5 charged tracks, Figure 4.20. Approximately 85% of the tau decays go to one charged particle accompanied by neutral decay products (one-prong decay), including $\tau \rightarrow e\nu\nu$ and $\tau \rightarrow \mu\nu\nu$ with a branching ratio of 18% each, and approximately 15% of decays go to three charged particles (three-prong decay).

The probability that the tau decays into five charged tracks (five-prong decay) is $(1.11 \pm 0.24) \cdot 10^{-3}$. The seven-prong branching fraction is less than $1.9 \cdot 10^{-4}$ [7]. Taus are reconstructed as hadronic jets which have between 1 and 3 tracks, using the cone clustering algorithm.

Chapter 5

Search for Higgs Boson decay into two photons

This analysis aims to select hZ events characterized by two photons and a Z boson in various decay modes. This gives rise to $q\bar{q}\gamma\gamma$, $\nu\bar{\nu}\gamma\gamma$ and $\ell^+\ell^-\gamma\gamma$, with $\ell = e, \mu, \tau$, final states, with the di-photon spectrum peaking at the Higgs boson mass.

Standard Model final states originating from Z decay are dominated by a pair of leptons or jets. These processes can be accompanied by energetic photons emitted by an initial- or final-state particle, producing acollinear leptons or jets in the final state. Such photons tend to have low energy and to lie close to the emitting particle, so that for final-state radiation they are frequently observed in the detector. A photon from initial-state radiation normally remains unobserved close to the beam axis, but in some cases can also be detected. The spectrum of the photons coming from these background processes is flat over a wide range of invariant masses.

In the $f\bar{f}\gamma\gamma$ event the Higgs mass can be reconstructed with a precision better than 2 GeV, giving a clear signal with very little background.

The selection criteria for each final state are described in the following sections and rely on a common photon identification.

To achieve a high sensitivity of the search it is necessary to eliminate as much of the Standard Model background as possible, while keeping a high efficiency for the signal. The efficiency of the search is calculated using a Monte Carlo generator for the Higgs boson production and decay, followed by the simulation of the final state particle behavior in the detector. The signal and background Monte Carlo samples must correspond to a higher luminosity than the data by at least a factor of three in order to ensure small statistical errors due to the Monte Carlo. Signal Monte Carlo samples comprise between 500 and 2000 events, depending on the search channel. The number of simulated events for the most important background channels is at least 100 times higher than the corresponding number of expected events in the data.

5.1 Photon pair selection

Photons are identified as clusters in the BGO electromagnetic calorimeter as described in section 4.4.3. Only clusters in the polar angle range $25^\circ < \theta < 35^\circ$, $45^\circ < \theta < 135^\circ$ and $145^\circ < \theta < 155^\circ$ are considered, well within the coverage of the barrel and end-cap regions of the BGO electromagnetic calorimeter. The gaps in the crystal coverage, where the EGAP detector is placed, are therefore excluded for this search. The distribution of the polar angle of the most energetic photon is shown in Figure 5.1. Forward-backward peaking, characteristic of initial state radiation, is observed. The cut on the photon polar angle reduces the background associated to initial state radiation, while keeping a large efficiency for the Higgs signal.

In the following selections we require at least two photons. To ensure that the pair of photons arise from the decay of a heavy resonance we require the energy of the most energetic photon to be larger than 10 GeV and the energy of the second most energetic photon to be larger than 6 GeV.

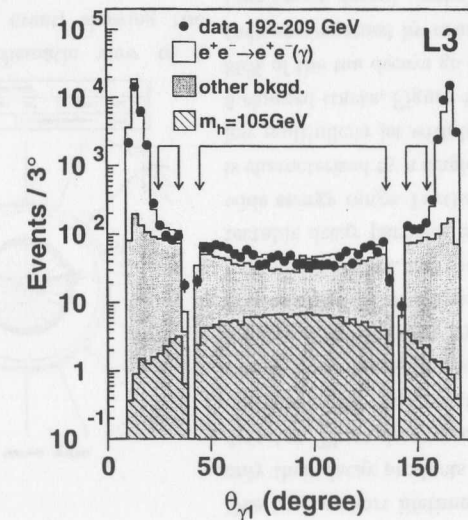


Figure 5.1: Distribution of the polar angle of the most energetic photon in data, background and for a Higgs boson signal with mass $m_h=105$ GeV, for all Z final states combined. The signal is superimposed with an arbitrary normalization. The selected θ regions are marked.

5.2 The $q\bar{q}\gamma\gamma$ final state

Run # 852001 Event # 2299 Total Energy : 230.38 GeV

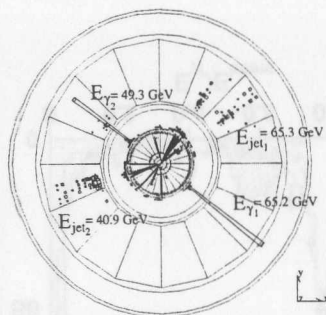


Figure 5.2: Candidate event for $e^+e^- \rightarrow q\bar{q}\gamma\gamma$ recorded by L3, showing two hadronic jets and two energy depositions in the electromagnetic calorimeter.

The signature for the $q\bar{q}\gamma\gamma$ final state is a pair of isolated photons accompanied by two jets. To select these events, we first apply a hadronic preselection requiring high multiplicity events. Events are accepted if

$$\begin{aligned} N_{\text{track}} &> 6 \\ N_{\text{cluster}} &> 12, \end{aligned} \quad (5.1)$$

where N_{track} is the number of reconstructed tracks which satisfy the requirements defined in section 4.4.2 and N_{cluster} is the number of calorimetric clusters with energy greater than 100 MeV.

The visible energy normalized to the centre-of-mass energy is required to be larger than 0.5 and the energy imbalances parallel and perpendicular to the

beam direction, normalized to the visible energy, are required to be below 0.4. In order to reduce the background from two-photon interaction events, we require the energy in a 30° cone around the beam pipe to be less than half of the visible energy. After these selection requirements, 17719 events remain in the data, while 17739.1 events are expected from Standard Model processes. The yield of this preselection is reported in Table 5.1. Figure 5.3 shows the comparison between data and Monte Carlo expectations for the distribution of the normalized visible energy, $E_{\text{vis}}/E_{\text{cm}}$, of the preselected events.

From this sample we select those events which contain at least two photons as described in section 5.1. All other particles are clustered in two jets using the DURHAM jet algorithm [125]. To reject photons coming from neutral hadron decays we require them to be isolated. This means the energy in a 10° cone around the photon direction must be less than 1.5 GeV, and in a 20° cone less than 4.5 GeV. The number of charged tracks and calorimeter clusters in a 20° cone around the photon direction must be below four. The opening angle between the photons must be larger than 50° and the angle between the photon direction and the nearest jet must exceed 25° .

The energy spectrum of the most energetic photon, normalized to the beam energy, before any cut is applied on the photon energies is presented in Figure 5.4 a). The

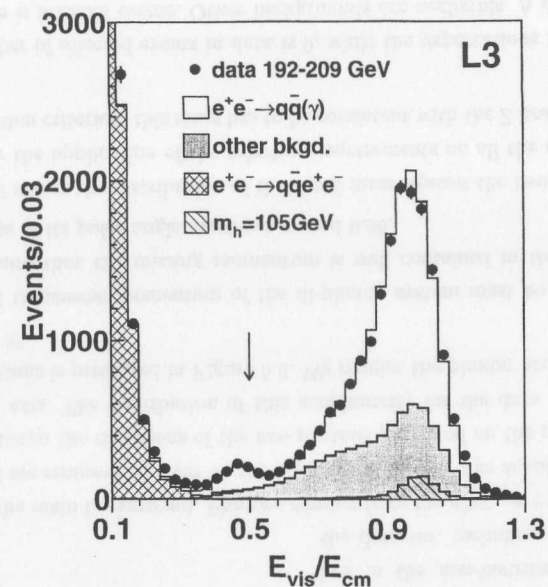


Figure 5.3: Distribution for the $q\bar{q}\gamma\gamma$ final state of the normalized visible energy after the hadronic preselection, in data, background and for a Higgs boson signal with mass $M_h = 105$ GeV. The signal is superimposed with an arbitrary normalization. The arrow indicates the value of the cut.

radiative return to the Z peak, produced by the on-shell production of the Z boson in the s-channel, is clearly visible at

$$E_\gamma = \frac{s - M_Z^2}{2\sqrt{s}}.$$

Figure 5.4 b) shows the distribution of the recoil mass against the di-photon system after the selection requirements on the photon energies.

Finally, the recoil mass against the di-photon system is required to be consistent with the Z mass, $|M_{\text{recoil}} - M_Z| < 15$ GeV. This requirement reduces the background from the $e^+e^- \rightarrow q\bar{q}(\gamma)$ process where either a neutral hadron from the Z decay mimics a photon or a photon in the final state is emitted; in both cases the recoil mass against the photons would be smaller than the Z mass.

The event having the highest value of the di-photon invariant mass is shown in Figure 5.2. It was collected at $\sqrt{s} = 205.1$ GeV and its di-photon invariant mass is 111.8 ± 1.0 GeV while the recoil mass against the di-photon system is 87.4 ± 0.8 GeV.

28 events are observed in the data, to be compared with 31 ± 0.6 expected background events, mainly from the $e^+e^- \rightarrow q\bar{q}(\gamma)$ process. Smaller contributions come from WW (0.2 events), ZZ (0.2 events) and Zee (0.1 events) processes. The signal efficiency is 40% for a Higgs boson mass of 100 GeV produced at $\sqrt{s} = 192$ GeV and 47% for a Higgs boson mass of 110 GeV at $\sqrt{s} = 208$ GeV. The number of selected data and background events are presented in Table 5.1.

| | N_{Data} | N_{Bkgd} | $q\bar{q}(\gamma)$ | WW | Ze^+e^- | ZZ |
|--------------|-------------------|-------------------|--------------------|--------|-----------|-------|
| Preselection | 17719 | 17739.1 | 11364.2 | 5876.7 | 139.4 | 358.9 |
| Selection | 28 | 31.0 ± 0.6 | 30.5 | 0.2 | 0.1 | 0.2 |

Table 5.1: Number of events observed in data, by the $q\bar{q}\gamma\gamma$ selection, N_{Data} , compared with the Standard Model expectations, N_{Bkgd} . The breakdown in different processes is presented.

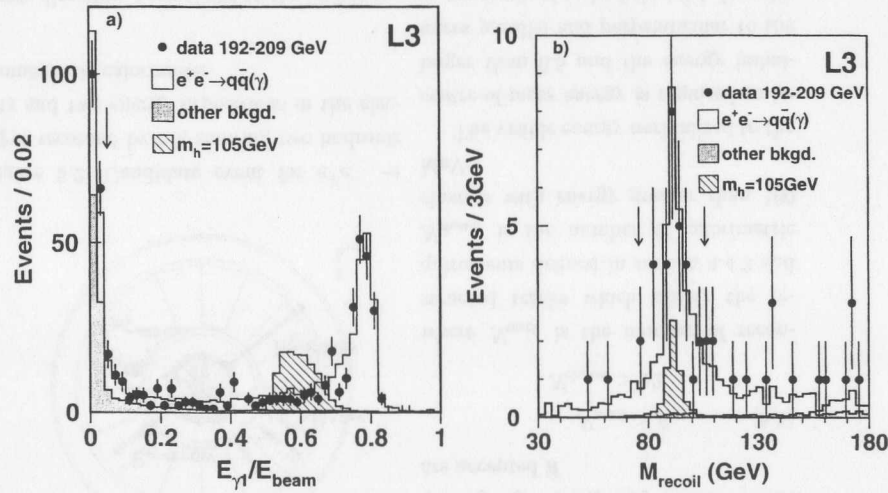


Figure 5.4: Distributions for the $q\bar{q}\gamma\gamma$ final state of a) the energy of the most energetic photon normalized to the beam energy and b) the recoil mass against the di-photon system in data, background and for a 105 GeV Higgs boson signal with arbitrary normalization. The arrows indicate the value of the cuts.

5.3 The $\nu\bar{\nu}\gamma\gamma$ final state

The $\nu\bar{\nu}\gamma\gamma$ final state is characterized by the presence of two photons and two invisible neutrinos in the event. Therefore, the selection keeps events with significant missing energy. Events containing a photon pair described in section 5.1. are selected. All detector components are required to measure no further energy depositions or charged tracks, apart from what is identified as photons. There must be no charged tracks and the energy not assigned to identified photons must be smaller than 10 GeV. Cuts on the energy depositions measured in the hadron calorimeter, in the luminosity monitor and in the EGAP

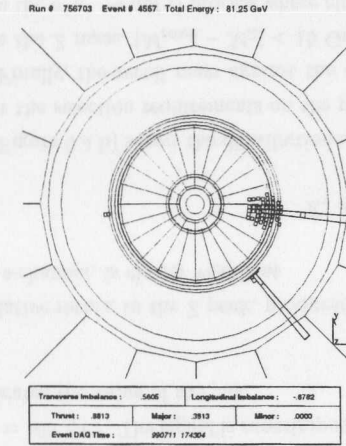


Figure 5.5: Candidate event for $e^+e^- \rightarrow \nu\bar{\nu}\gamma\gamma$ process.

are imposed. Events with missing energy, either from neutrinos or particles lost in the non-instrumented parts of the detector, including initial-state radiation, are the main background. Photons coming from the $e^+e^- \rightarrow \gamma\gamma(\gamma)$ process are coplanar and are removed by a cut on the acoplanarity angle. The acoplanarity angle is the angle between the directions of the two photons projected on the plane transverse to the beam axis. The distribution of this acoplanarity for the data and the Monte Carlo predictions is presented in Figure 5.6. We require the photon acoplanarity to be greater than 3° .

The total transverse momentum of the di-photon system must be greater than 2 GeV. To ensure that the missing momentum is well contained in the detector, the absolute value of its polar angle must not exceed 0.96.

Figure 5.7 shows the distribution of the recoil mass against the two most energetic photons after the application of the selection requirements on all the other variables. As final selection criterion, this mass has to be consistent with the Z boson mass within 15 GeV.

The number of selected events in data is 9, while the expectations for the $e^+e^- \rightarrow \nu\bar{\nu}(\gamma)$ process is 9.2 ± 0.3 events. Other backgrounds are negligible. A candidate event is displayed in Figure 5.5.

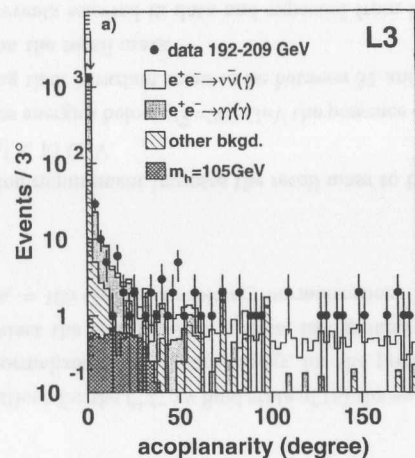


Figure 5.6: Distribution for the $\nu\bar{\nu}\gamma\gamma$ final state of the acoplanarity of the $\gamma\gamma$ system, in data, background and for a Higgs boson signal with the mass $M_h = 105$ GeV. The signal is superimposed with arbitrary normalization. The arrow indicates the value of the cut.

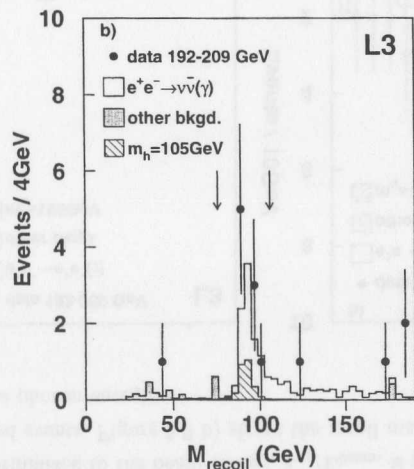


Figure 5.7: Distribution for the $\nu\bar{\nu}\gamma\gamma$ final state of the recoil mass against the two photons in data, background and for a Higgs boson signal with the mass $M_h = 105$ GeV. The signal is superimposed with arbitrary normalization. The arrows indicate the values of the cuts.

The signal efficiency is 47% for a Higgs boson mass of 100 GeV at $\sqrt{s} = 192$ GeV and 50% for a Higgs boson of 105 GeV mass at $\sqrt{s} = 208$ GeV.

5.4 The $\ell^+\ell^-\gamma\gamma$ final state

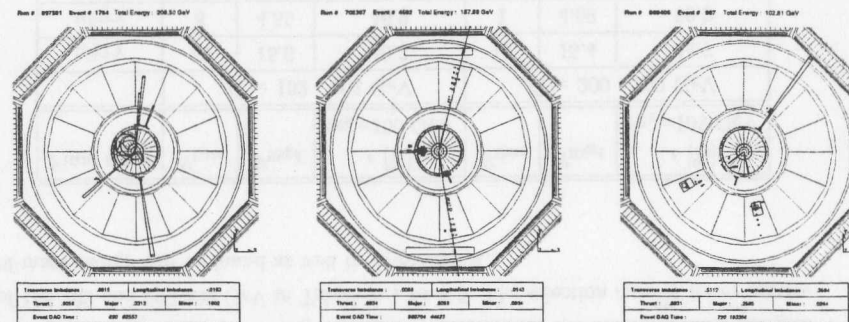


Figure 5.8: Candidate events for the $e^+e^-\gamma\gamma$, $\mu^+\mu^-\gamma\gamma$, $\tau^+\tau^-\gamma\gamma$ processes.

The $\ell^+\ell^-\gamma\gamma$ final state is characterized by the presence of two photons and a pair of same type, isolated and energetic leptons. A selection based on identified leptons with momentum greater than 3 GeV and an energy below 3 GeV in a cone of half-angle 10° around the lepton is efficient in selecting the signal events and rejecting the background.

First low multiplicity events with a photon pair and a lepton pair are preselected.

Electrons are identified as clusters in the BGO electromagnetic calorimeter as described in section 4.4.3. To increase the efficiency, we accept events with at least one identified electron.

Muons are reconstructed as explained in section 4.4.3. Also events with one muon and one minimum ionizing particle in the calorimeters are accepted, as well as events with a single muon where the second muon is missing or misidentified. Background events from cosmic rays are removed by requiring at least one hit in the scintillation counters within a ± 5 ns time window around the beam crossing time.

Tau leptons are identified as jets with one or three tracks in a 10° cone with an energy greater than 3 GeV. The energy in the $10^\circ - 30^\circ$ cone must not exceed 30% of the energy in the $0^\circ - 10^\circ$ cone around the tau direction. In order to maintain a high efficiency, events with only one identified tau lepton are also accepted.

After these selection requirements, 738 events remain in the data, while 751.3 events are expected from Standard Model processes. The result of this preselection is reported in Table 5.2. Further, the energy of the most energetic lepton is required to be less than 80 GeV to suppress double radiative di-lepton events. The energy of the second most energetic photon normalized to the beam energy, $E_{\gamma_2}/E_{\text{beam}}$, is presented in Figure 5.9 a) for the preselected events. Figure 5.9 b) shows the recoil mass against the photons after the cuts on the photon energies.

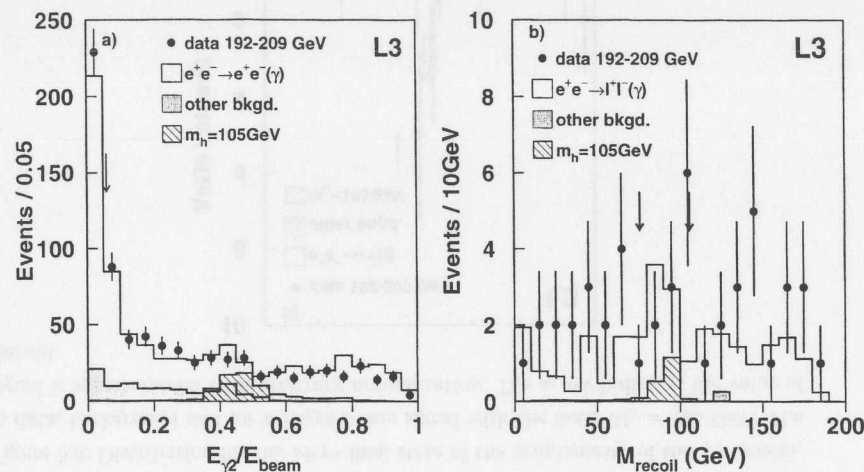


Figure 5.9: Distributions for the $\ell^+\ell^-\gamma\gamma$ final state of (a) the energy of the second most energetic photon normalized to the beam energy, for the preselected events, and (b) the recoil mass against the two photons in data, background and for a Higgs boson signal with mass $m_h = 105$ GeV and arbitrary normalization. The arrows indicate the value of the cuts.

The final selection requirement imposes the recoil mass to be consistent with the Z mass, $|M_{\text{recoil}} - M_Z| < 15$ GeV.

At centre-of-mass energies below $\sqrt{s}=202$ GeV the presence of two identified leptons is enforced, requiring their invariant mass to be between 81 and 101 GeV, relaxing the selection criterion on the recoil mass.

The number of events selected in data and expected from background processes is presented in Table 5.2. Seven events are observed in the data, with 8.0 ± 2.8 expected from background Monte Carlo, mainly from the $e^+e^- \rightarrow \ell^+\ell^-(\gamma)$ processes. Three

candidate events are shown in Figure 5.8. The signal efficiency in the lepton channel varies from 31% for a Higgs boson mass of 100 GeV produced at $\sqrt{s} = 192$ GeV to 43% for a Higgs boson with the mass $m_h = 110$ GeV produced at $\sqrt{s} = 208$ GeV.

| | N_{Data} | N_{Bkgd} | $e^+e^-(\gamma)$ | $\mu^+\mu^-(\gamma)$ | $\tau^+\tau^-(\gamma)$ | 4f |
|--------------|-------------------|-------------------|------------------|----------------------|------------------------|-------|
| Preselection | 738 | 751.3 | 541.7 | 46.2 | 50.4 | 113.0 |
| Selection | 7 | 8.0 ± 2.8 | 4.2 | 1.8 | 2.0 | 0.0 |

Table 5.2: Number of events observed in data, by the $\ell^+\ell^-\gamma\gamma$ selection, N_{Data} , compared with the Standard Model expectations, N_{Bkgd} . The breakdown in different processes is given.

5.5 Summary of the event selection

The results of all the selections are presented in Table 5.3. The total number of selected events in the data is 44, to be compared to 48.1 expected from the Standard Model processes. In conclusion, no excess indicating the production of a Higgs boson decaying into photons is observed in the data.

All selection cuts for the single channels are listed for the centre-of-mass energies of 192-202 and 200-209 GeV in Tables A.1 to A.5. The selection cuts at lower centre-of-mass energy can be found as well in Appendix A.

| Final state | N_{Data} | N_{Bkgd} | ϵ [%] | | N_{Data} | N_{Bkgd} | ϵ [%] | |
|----------------------------|-------------------|-------------------|----------------------------|---------------|-------------------|-------------------|----------------------------|--|
| | | | $m_h=100$ GeV | $m_h=105$ GeV | | | | |
| | | | $\sqrt{s} = 192 - 202$ GeV | | | | $\sqrt{s} = 200 - 209$ GeV | |
| $q\bar{q}\gamma\gamma$ | 10 | 15.6 | 40.3 | | 18 | 15.4 | 44.7 | |
| $\nu\bar{\nu}\gamma\gamma$ | 8 | 4.55 | 46.9 | | 1 | 4.59 | 50.2 | |
| $e^+e^-\gamma\gamma$ | 1 | 0.7 | 39.1 | | 2 | 2.6 | 45.6 | |
| $\mu^+\mu^-\gamma\gamma$ | 2 | 0.7 | 32.3 | | 0 | 1.1 | 46.2 | |
| $\tau^+\tau^-\gamma\gamma$ | 0 | 0.7 | 20.3 | | 2 | 2.15 | 31.1 | |

Table 5.3: Number of events observed in data, N_{Data} , compared with the Standard Model expectations, N_{Bkgd} and the efficiency for each final state at centre-of-mass energies $\sqrt{s} = 192 - 202$ GeV and $\sqrt{s} = 200 - 209$ GeV.

5.6 Systematic uncertainties

Several potential sources of systematic uncertainty on the number of signal and background events were investigated. These include the photon identification, photon isolation criteria, and the simulation of the energy and angular resolution of the photons.

Systematic effects on the signal efficiency are quantified with respect to variations of the signal efficiency ($m_h = 105$ GeV) at the working point, ϵ , defined as:

$$\Delta\epsilon_{\text{relative}} = \frac{\epsilon' - \epsilon}{\epsilon},$$

where ϵ' is the new signal efficiency determined from a given systematic variation. The dominant source of error for the signal efficiency is the signal Monte Carlo statistics, typically below 2%. The systematic uncertainty introduced by the photon identification criteria is studied and quantified using a sample of Bhabha scattering events, where one of the two electrons is tagged, and the other one is used to estimate the efficiency of the identification. The difference in the efficiency extracted from data and Monte Carlo simulations provides a systematic error of less than 0.6%. The energy and angle of the photons are well measured and lead to a systematic error on the efficiency smaller than 0.1%. The systematic error on the photon energy scale is estimated to be 1% for the Z return photons of 83 GeV at $\sqrt{s} = 206.6$ GeV. A variation of $\pm 2\%$ of the energy scale related quantities in the selection does not yield a sizable effect on the efficiency. The resulting systematic uncertainty on the di-photon mass is 300 MeV at a mass of 105 GeV. All of the combined systematic uncertainties are less than the statistical uncertainty due to the limited size of the simulated event sample.

Variations in the expected background events are also studied. The main contributions to the uncertainty assigned to the background arise from the finite Monte Carlo statistics (4%) and the background normalization for hadronic events with photons (7%), as estimated from a comparison between the KK2F and PYTHIA Monte Carlo predictions.

The systematic uncertainty on the integrated luminosity is 0.3% resulting in little effect on the limits.

In conclusion, an overall systematic error of 8% on the number of expected background events and 2% on the number of expected signal events is estimated and incorporated into the final result (the upper limits on the branching fraction for the Higgs boson decay into two photons) presented in Chapter 6. The effect of the systematic error is small. A variation within 200 MeV has been found in data and simulation with respect to the mass limit derivation without taking into account the systematic error.

Chapter 6

Results

6.1 Interpretation

The strategy of the Higgs search is to build a confidence level based on the reconstructed di-photon invariant mass of the individual analyses assuming that we understand the background and have a reliable estimate of the signal from Monte Carlo simulation. This confidence level is then calculated for our observed data with the hypothesis that the predicted signal is present in the data. If the confidence level excludes such an assumption, then we rule out that value of the branching fraction $\text{BR}(h \rightarrow \gamma\gamma)$ with some level of confidence. A scan over the Higgs mass is done recalculating this confidence level for the many different mass values that are kinematically allowed and which have not been ruled out previously. At each scanned mass value a scan over the $\text{BR}(h \rightarrow \gamma\gamma)$ is done in 0.01 steps. The confidence level used to quantify the likelihood of the hypothesis of a Higgs signal being present in the data will be described in the following. We use a frequentistic approach to estimate the confidence level, CL. It is defined in such a way that if $\text{CL} = 95\%$, then there is only a 5% probability of the signal actually being present in the data. In this way, we speak of a 95% exclusion of a certain $\text{BR}(h \rightarrow \gamma\gamma)$. Two different methods to calculate the confidence level have been used. Both methods take as input the reconstructed di-photon invariant mass distribution of the combined results of all the search channels. Each bin of this spectrum is treated as an independent, uncorrelated, mini-analysis with its own characteristic signal, background and number of observed events.

No excess with respect to the expected number of events from the background has been observed in the analysis. The result has therefore been used to derive an exclusion limit. The methods used to calculate the confidence level for the exclusion are described in the following.

6.1.1 Bayesian approach

In the Bayesian approach the probability for the presence of a signal with an expected number of events s' that is greater than the expected number of events from the signal hypothesis s is calculated, given the outcome of n observed events in the experiment [128],

$$P(s' > s|n) = \int_s^\infty f(s'|n) ds'. \quad (6.1)$$

With the help of Bayes' theorem this expression is written in terms of the known probabilities $P(n|s')$.

$$f(s'|n) = \frac{P(n|s')f(s')}{P(n)} = \frac{P(n|s')f(s')}{\int_0^\infty P(n|s')f(s') ds'}.$$

All s' are assumed to have the same a priori probability, i.e. $f(s') = \text{const}$. From this assumption follows that

$$f(s'|n) = \frac{P(n|s')}{\int_0^\infty P(n|s') ds'}. \quad (6.3)$$

Equation (6.2) inserted in Eq. (6.1) gives

$$P(s' > s|n) = \frac{\int_s^\infty P(n|s') ds'}{\int_0^\infty P(n|s') ds'}. \quad (6.4)$$

The signal hypothesis is said to be excluded at a confidence level of CL if

$$1 - P(s' > s|n) = 1 - \frac{\int_s^\infty P(n|s') ds'}{\int_0^\infty P(n|s') ds'} \geq CL$$

The number of events observed in a single channel experiment is Poisson distributed. The probability to observe n events in an experiment with an expected background of b events and an expected signal of s' events is

$$P(n|s') = \frac{\exp^{-(s'+b)}(s'+b)^n}{n!}$$

The method to derive the confidence level in a single channel experiment described above can be generalized to a multichannel experiment. In an experiment with N independent channels the probability to see n events if there exists a signal with an expected number of events s' is

$$P(n|s') = \prod_{i=1}^N \frac{\exp^{-(s'_i + b_i)}(s'_i + b_i)^{n_i}}{n_i!},$$

where n_i is the number of observed events in channel i , b_i and s_i are the expected number of events in channel i from background and signal events respectively, and

$$p_i = \frac{s_i}{\sum_{i=1}^N s_i}$$

is the fraction of the total number of expected signal events that is expected in channel i .

When combining results from different centre-of-mass energies, each final state at each centre-of-mass energy has been treated as a separate channel.

6.1.2 Frequentistic approach

The observed data are used to test two hypotheses: the background-only (b) hypothesis, which assumes that no Higgs boson is present in the mass range which is investigated, the data receiving contributions from the Standard Model processes only, and the signal+background (s+b) hypothesis, where the Higgs boson is assumed to be produced according to the model under consideration.

A test-statistic (or estimator) X is constructed, in order to allow a classification of the experimental results between the two situations: b-like, or s+b-like. The value of the test-statistic measured in the data, X^{Obs} , is compared to the distributions of the same test-statistic corresponding to the two hypothesis, X_b and X_{s+b} , obtained on the basis of a large number of Monte Carlo simulations of the real experiment.

The confidence in the signal+background hypothesis is given by the probability that the estimator is smaller than the value observed in an experiment under the assumption that the signal+background hypothesis is true:

$$CL_{s+b} = P(X < X^{Obs} | s+b) = \int_0^{X^{Obs}} f(X' | s+b) dX'.$$

Similarly, the confidence in the background-only hypothesis is defined as the probability that X is less than the value observed under the assumption that the background-only hypothesis is true:

$$CL_b = P(X < X^{Obs} | b) = \int_0^{X^{Obs}} f(X' | b) dX'.$$

The signal hypothesis is said to be excluded at a confidence level CL if

$$1 - CL_s = 1 - \frac{CL_{s+b}}{CL_b} \geq CL.$$

As already mentioned, the probability density functions for X used to define the confidences CL_{s+b} and CL_b can, in the general case, not be derived analytically. They are obtained using Monte Carlo sampling from the distributions of the discriminating variables for signal and background events. The reconstructed Higgs mass can be used as a discriminating variable.

There are several methods to construct the test-statistic. The L3 experiment uses the Bayesian probability defined by Eq. 6.3.

Another method uses the ratio of the likelihood for signal+background to the likelihood for background only,

$$Q = \frac{\mathcal{L}_{s+b}}{\mathcal{L}_b},$$

to rank the results between the two hypothesis. For convenience, the following quantity is actually used,

$$-2 \ln Q = 2s - 2 \sum_i n_i \ln(1 - s_i/b_i),$$

which corresponds to the $\Delta\chi^2$ between the two hypothesis in the limit of high statistics. This test-statistics has been adopted by the LEP Higgs working group to combine the data from the four LEP experiments, as it will be discussed later. It maximizes the probability of rejecting a false hypothesis at a given confidence level, and makes use of the information available in a search in the most efficient way, similarly to the way the principle of maximum likelihood gives the most efficient estimators of parameters in a measurement. An example of a test-statistic $-2\ln Q$ as a function of the Higgs boson mass is shown in Figure 6.1.

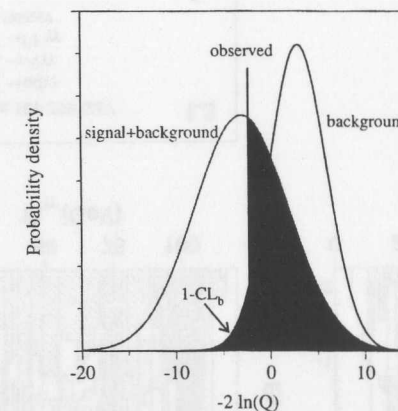


Figure 6.1: An example of the probability density function of $-2\ln Q$ for background, b, and signal+background, s+b, Monte Carlo experiments. The observed value of $-2\ln Q$ which corresponds to the data is indicated by a vertical line. The dark shaded area is a measure of the compatibility with the b hypothesis, $1-CL_b$, and the light shaded area is a measure of the compatibility with the s+b hypothesis, CL_{s+b} .

The b-only Monte Carlo simulations can also be used to calculate an expected confidence level in the absence of a signal based purely on the Monte Carlo prediction for background. The confidence level computed in this way indicates the sensitivity of the analysis. There are commonly two ways used to quote the expected confidence level. The average CL is just the overall average of the confidence level distribution. The median CL is the confidence level where the distribution is divided into two equally large portions, indicating that one would expect in 50% of the experiments a lower and in 50% a higher confidence level. As the latter is precisely defined independent of the shape of the confidence level distribution, we will use in the following the median expected CL. The same distribution can be used to extract the probability that the observed confidence level is consistent with the background only hypothesis which is a strong indication for the presence of a signal.

The Monte Carlo simulations to estimate the number of signal and background events take into account the centre-of-mass energy, the integrated luminosity of the data sample, the cross sections and decay branching fractions for the signal and background processes, the selection efficiencies, the experimental resolutions and the systematic errors.

If one wishes to account for an uncertainty on the number of accepted background events, we can smear each value of b_i used in the Monte Carlo trials. The smearing can be accomplished by randomly sampling a Gaussian with a width corresponding to the relative size of the systematic error. The number of background events in that bin during that trial is then rescaled by this random amount. Similarly, to estimate the effects of a systematic error on the number of signal events, one can use an independent smearing of the values s_i used in the Monte Carlo trials. The statistical error can be dealt with by taking into account the fluctuations on the predicted number of background and signal events due to the Poisson fluctuations on the original number of generated events. These Poisson fluctuations can then be properly introduced into b_i and s_i during the Monte Carlo trials used to calculate the confidence level.

6.2 Results

The events passing all the hZ cuts are used to set an upper limit on the di-photon branching fraction for a particle having the Standard Model Higgs boson production rate. We use the reconstructed di-photon invariant mass as final discriminant variable. The distributions of di-photon masses for the hZ search candidates in the year 2000 data are shown in Figure 6.2 a), together with the simulation of the Standard Model backgrounds and a Higgs signal with $m_h = 105$ GeV. The distribution of the di-photon masses for the hZ search candidates in the data from all L3 search energies,

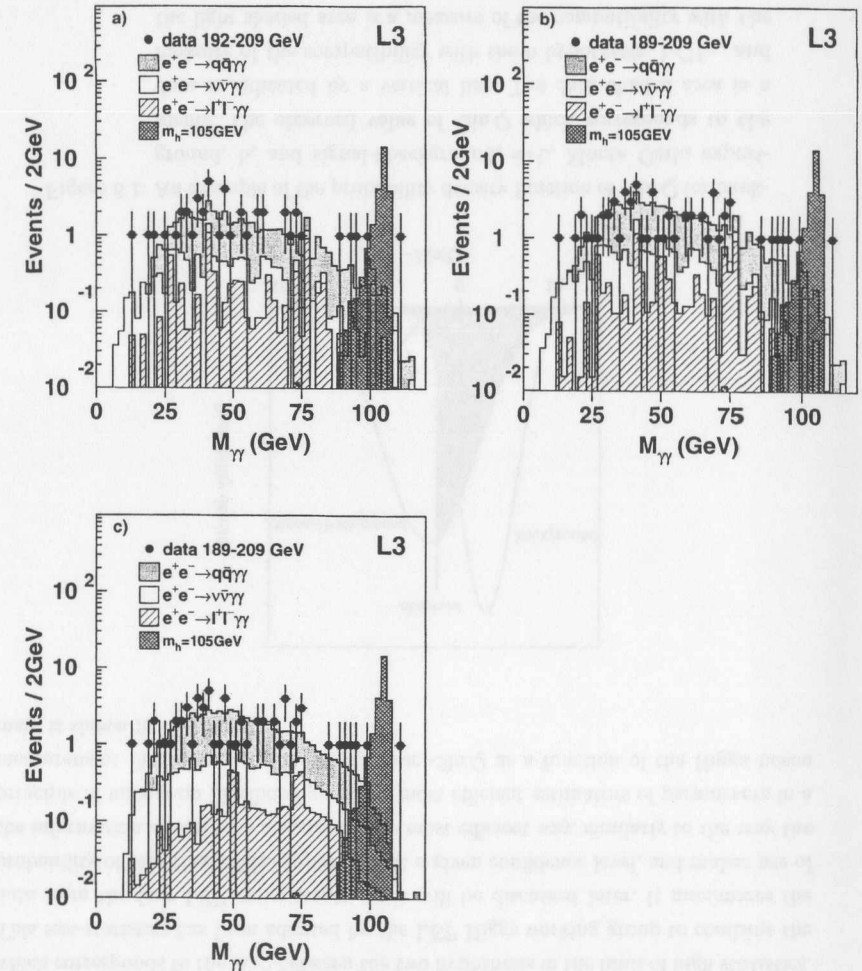


Figure 6.2: Distributions of the reconstructed di-photon invariant mass for all final states combined, after the final selection. Data collected at a) $\sqrt{s} = 192 - 209$ GeV, b) and c) $\sqrt{s} = 189 - 209$ GeV are shown together with the background and a Higgs boson signal with mass $m_h = 105$ GeV, for a Standard Model cross section and a $BR(h \rightarrow \gamma\gamma) = 1$. Backgrounds in c) were smoothed using the KEYS program [129].

namely 189 - 209 GeV is also given in Figure 6.2 b). These distributions are well described by the Standard Model processes. The latter distribution is also shown in Figure 6.2 c). The backgrounds in this graph were smoothed using the KEYS program [129] described in Appendix B, in order to avoid numerical problems which can arise in some bins due to low Monte Carlo statistics.

The final distributions are combined using the technique described in section 6.1 for the $hZ \rightarrow q\bar{q}\gamma\gamma$, $\nu\bar{\nu}\gamma\gamma$ and $\ell^+\ell^-\gamma\gamma$, with $\ell = e, \mu, \tau$. A scan in the Higgs masses is performed from 50 GeV to 120 GeV in steps of 1 GeV, the order of the mass resolution. Monte Carlo samples were generated using PYTHIA for Higgs masses between 50 and 80 GeV in steps of 10 GeV, and between 80 to 120 GeV in steps of 5 GeV. In order to compute the signal and background confidence level at arbitrary masses it was necessary to perform an interpolation between the mass points where Monte Carlo simulation results are available. The method used is based on the linear interpolation of the inverse of the cumulative distribution functions and it is described in Appendix C [130]. The region below 50 GeV is less interesting for this work as it was excluded by previous L3 Higgs searches using the hadronic final state [131].

At each mass point a scan over the $BR(h \rightarrow \gamma\gamma)$ in steps of 0.01 is done, and for each point the confidence level for the signal exclusion is calculated. The value of the $BR(h \rightarrow \gamma\gamma)$, at each mass point, for which the confidence level is 95%, is kept.

Figure 6.3 (left) shows the 95% confidence level upper limit for the di-photon branching fraction obtained in this way, when the Standard Model hZ production cross section is assumed at each centre-of-mass energy and combining all the candidate events. The statistical method used to extract these results is the likelihood log ratio, $-2\ln Q$. A comparison to the results obtained using the L3 statistical method is shown in Figure 6.3 (right). Since the two methods use different test-statistics, the resulting exclusion limits are expected to show some differences, especially in the vicinity of candidate events. One can see that the two sets of results agree within 15% in $BR(h \rightarrow \gamma\gamma)$.

The limits on the $BR(h \rightarrow \gamma\gamma)$ are used to rule out Higgs bosons in certain non-minimal models. Before concentrating on calculating a Higgs boson exclusion it is interesting to look at the confidence level for the background-only hypothesis, $1-CL_b$. This quantity is the most likely to show evidence of a Higgs signal discovery and it is shown in Figure 6.4. There is no indication for new physics in this graph; the candidates passing the cuts for all three topologies are consistent with the Standard Model processes over a wide range. The low value of $1-CL_b$ in the mass range around 75 GeV is due to the excess of candidate events in this mass region in the data collected at $\sqrt{s}=189$ GeV. This excess is most likely due to a statistical fluctuation, since it is not confirmed at any higher centre-of-mass energy. This region is now more excluded

then with the 189 GeV data alone, see Figures 6.3 and B.2. Nevertheless, there are no values of the $M_{\gamma\gamma}$ where CL_b comes close to the level required for a discovery of new phenomena. A $5\text{-}\sigma$ significance leading to $1-CL_b = 5.7 \cdot 10^{-7}$ value is required for the claim of a signal in the presence of background.

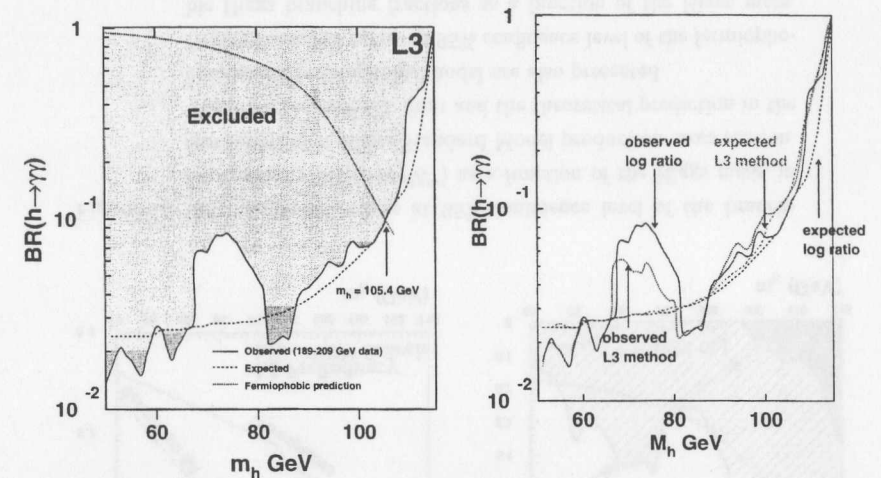


Figure 6.3: (left) Excluded values at 95% confidence level of the branching fractions $BR(h \rightarrow \gamma\gamma)$ as a function of the Higgs mass, in the assumption of the Standard Model production cross section. The expected 95% confidence level limit and the theoretical prediction are also presented.

(right) Comparison of the result obtained with two statistical methods described in the text.

After the CL_b has been examined and no evidence of a Higgs boson signal is present in the data, the only thing left to do is to exclude the Higgs boson. Also shown in Figure 6.3 is the $h \rightarrow \gamma\gamma$ branching fraction in the Standard Model computed with the HDECAY program [43] and excluding all the fermionic couplings. A 95% confidence level lower mass limit for such a benchmark fermiophobic Higgs boson is set at 105.4 GeV, where the predicted branching fraction crosses the upper limit curve. The median limit one would expect to obtain in an ensemble of experiments in the absence of a

signal is 105.3 GeV.

To conclude, it is worthwhile to recall the results presented in Figure 2.16. At the value of the mass limit, the preferred decay mode of the fermiophobic Higgs is into a WW^* pair, and so there is not much to be gained going at higher centre-of-mass energies for the search of a fermiophobic Higgs boson in the two photon decay mode alone at a e^+e^- collider. However, since $h\gamma\gamma$ has a very clean signature, it still remains a powerful channel for the search of a fermiophobic (but also of the Standard Model) Higgs boson in $\bar{p}p$ or pp collisions, at the Tevatron and LHC.

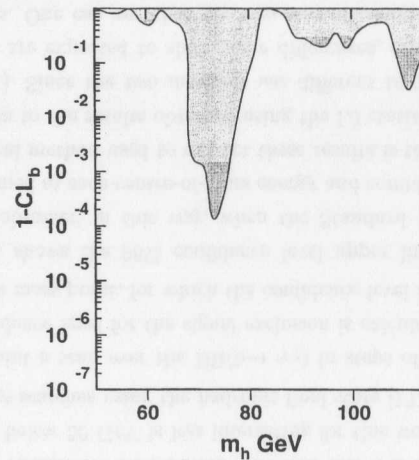


Figure 6.4: Distribution of $1-CL_b$ for all L3 data in the $h \rightarrow \gamma\gamma$ search.

6.3 Results of the $h \rightarrow WW^*$ channel and combination with $h \rightarrow \gamma\gamma$

As seen in Figure 2.17, for Higgs masses greater than about 100 GeV the di-photon branching fraction decreases rapidly, while the $h \rightarrow WW^*$ decay mode, with one gauge boson being virtual, becomes dominant. This motivates a search in the $h \rightarrow WW^*$ channel. The L3 Collaboration has looked for a fermiophobic Higgs boson in this decay mode in the data collect at $\sqrt{s}=192\text{-}209$ GeV [132].

Since the Higgs boson is produced in association with the Z, there are nine possible final states which result from the decays of the Z and W gauge bosons. The L3

Collaboration has developed analyses for the following ones, which corresponds to 85% of the total branching ratio of $hZ \rightarrow WW^* \bar{f}f$: $qqqq(qq)$, $qq\ell\nu(qq)$, $qqqq(\nu\nu)$, $qq\ell\nu(\nu\nu)$, and $qqqq(\ell\ell)$, where the decay of the Z is given in parentheses.

No signal has been found in the data with respect to the expectations from the Standard Model processes. These negative search results are used to set upper limits on the branching fractions for the Higgs decay into a WW^* pair, assuming a Standard Model production rate for the Higgs boson. The excluded region in the $(BR(hZ \rightarrow WW^* \bar{f}f), m_h)$ plane is shown in Figure 6.5 (left), together with the predictions of the benchmark fermiophobic model.

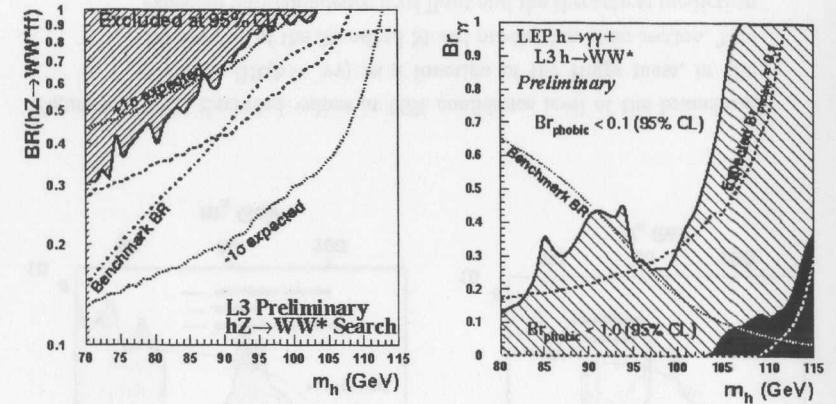


Figure 6.5: (left) Excluded values at 95% confidence level of the branching fractions $BR(h \rightarrow WW^*)$ as a function of the Higgs mass, in the assumption of the Standard Model production cross section. The expected 95% CL limit and the theoretical prediction in the benchmark fermiophobic model are also presented.

(right) Excluded values at 95% confidence level of the fermiophobic Higgs branching fractions as a function of the Higgs mass, combining LEP $h \rightarrow \gamma\gamma$ and L3 $h \rightarrow WW^*$ searches (from Ref. [132]).

In order to increase the sensitivity of the fermiophobic Higgs search, the di-photon branching fractions can be combined with the $h \rightarrow WW^*$ decay mode. The total Higgs branching fraction to pairs of gauge bosons in a general fermiophobic search can be

6.3. RESULTS OF THE $H \rightarrow WW^*$ CHANNEL AND COMBINATION WITH $H \rightarrow \gamma\gamma$

parameterised as

$$BR_{\text{phobic}} = BR(h \rightarrow \gamma\gamma) + BR(h \rightarrow WW),$$

with $BR(h \rightarrow \gamma\gamma)/BR_{\text{phobic}} = BR_{\gamma\gamma}$ being the fraction of fermiophobic decays into a photon pair. The 95% CL excluded BR_{phobic} values are determined by a scan in the $(BR_{\gamma\gamma}, m_h)$ plane. The result of this combination is shown in Figure 6.5 (right) together with the benchmark values of $BR_{\gamma\gamma}$. The point where this curve crosses the $BR_{\text{phobic}} = 1$ gives the model-dependent limit. It yields an expected limit of 111.2 GeV and an observed limit of 106.4 GeV.



Figure 6.5: (left) $BR(h \rightarrow \gamma\gamma)$ vs m_h and (right) BR_{phobic} vs m_h . The right plot shows the 95% CL excluded region (shaded) and the model-dependent limit (crossing point of the curve and $BR_{\text{phobic}} = 1$).

| Channel | Observed | Expected |
|--------------------------|-----------|-----------|
| $BR_{\text{phobic}} < 1$ | 106.4 GeV | 111.2 GeV |
| $BR_{\text{phobic}} > 1$ | 106.4 GeV | 111.2 GeV |
| $BR_{\text{phobic}} = 1$ | 106.4 GeV | 111.2 GeV |
| $BR_{\text{phobic}} < 1$ | 106.4 GeV | 111.2 GeV |
| $BR_{\text{phobic}} > 1$ | 106.4 GeV | 111.2 GeV |

Chapter 7

Outlook

The L3 detector is not the only place where a photonic Higgs boson has been searched for. The four experiments at the LEP collider have all been used to search for the Higgs boson through the decay into two photons.

After the closure of LEP the search will continue at other collider facilities. There are at the moment searches performed using the detectors at the Tevatron collider at Fermilab and preparations have started for the searches that will take place at the Large Hadron Collider that is presently being constructed at CERN.

7.1 ALEPH, DELPHI and OPAL

The results of the search for a Higgs boson decaying into two photons presented in this thesis are confirmed by the searches performed at the other experiments at LEP. The ALEPH Collaboration concentrates on the di-photon system, performing a global analysis, while the other Collaborations, DELPHI and OPAL, carry out similar analyses as L3 does, selecting separately each of the search channels. The observed and expected mass limits for a fermiophobic Higgs boson decaying into two photons obtained by the four collaborations are listed in Table 7.1.

The mass limits obtained are sensitive to the limited sizes of the collected data samples. By combining the data collected by the four experiments, an integrated luminosity four times the amount collected by one of the detectors alone can be achieved. Such a combined analysis has been carried out by the LEP working group for Higgs boson searches [136]. The information provided by each LEP experiment as input to the combination is the distribution of the reconstructed Higgs boson mass, m_h . For each bin of these distributions, the experiments provide the number of selected data events, n_i , the expected background rate, b_i , and the expected signal, $s_i(m_h, BR)$. The statistical procedure adopted for the combination of the data and the definitions of the test-statistic to rank the experimental results between the b-only and s+b hypothesis,

| Detector | Observed limit | Expected limit |
|----------------|-------------------|-------------------|
| ALEPH [133] | 104.4 GeV | 104.6 GeV |
| DELPHI [134] | 103.6 GeV | 105.1 GeV |
| L3 [99] | 104.1 (105.4) GeV | 104.9 (105.3) GeV |
| OPAL [135] | 104.8 GeV | 105.2 GeV |
| Combined [136] | 108.2 GeV | 109.0 GeV |

Table 7.1: The observed and expected mass limits for a fermiophobic Higgs boson from the searches performed at the four detectors at the LEP collider, and the limits obtained when combining the results of the four experiments. All limits are given at 95% confidence level. All results are preliminary and are taken from Ref. [136]. The numbers given in parentheses are the final results of L3 presented in this thesis (see section 6.4).

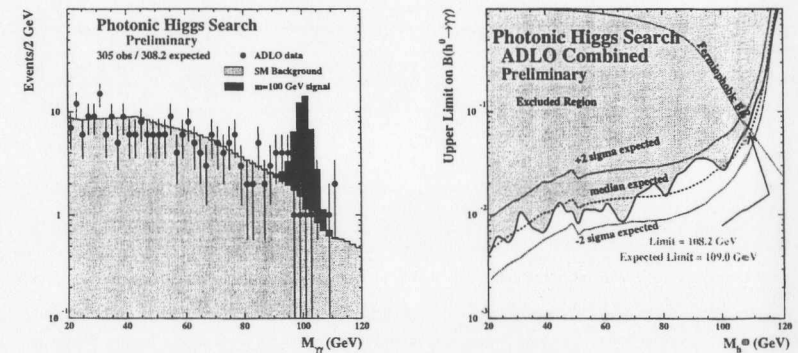


Figure 7.1: The distribution of the di-photon invariant mass (left) and the observed and expected upper limits of the $BR(h \rightarrow \gamma\gamma)$ as a function on the Higgs mass, with the assumption of a Standard Model production cross section and combining the results of the four detectors at the LEP collider [136]. The limits are given at 95% confidence level (right).

the quantity $-2\ln Q$, as well as the confidence levels CL_s , CL_{s+b} and CL_b are the ones described in section 6.2.

The result of the combined analysis excludes the existence of a fermiophobic Higgs boson with mass lower than 108.2 GeV at 95% confidence level (see Figure 7.1).

7.1.1 Other searches by DELPHI

DELPHI is searching for a fermiophobic Higgs boson in the framework of the general 2HDM of type I, combining both production mechanisms, $e^+e^- \rightarrow hZ$ and $e^+e^- \rightarrow hA$ [137]. As mentioned in section 3.2.1., these processes have complementary cross sections, proportional to $\sin^2 \delta$ and $\cos^2 \delta$, respectively. The high δ region is studied by analysing the Higgs-strahlung process, and this constituted the main subject of this thesis. For small values of $\sin^2 \delta$ the Higgs-strahlung cross-section vanishes, and so the small δ region is constrained by the associated hA production. The combination of both processes leads to an interpretation of the results as a function of m_h and m_A .

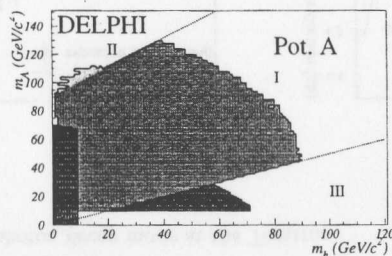


Figure 7.2: 95% confidence level excluded region in the (m_h, m_A) plane, combining the Higgs-strahlung and the associated production processes, in the framework of potential A (see section 2.6.1), valid for all δ values. Region I corresponds to the $h \rightarrow \gamma\gamma$ and $A \rightarrow b\bar{b}$ decay modes. Region II corresponds to $A \rightarrow hZ$ and region III corresponds to $h \rightarrow AA$ and $A \rightarrow b\bar{b}$. The dark area at low masses shows the limit from the total Z width. (from Ref. [137])

The dominant decay modes for $m_h < M_Z$ are $h \rightarrow AA$ (if $m_h > 2m_A$) and $h \rightarrow \gamma\gamma$. For $m_h > M_Z$, the decays of h into other boson pairs can be important: $h \rightarrow Z\gamma$ for the very small δ region, or $h \rightarrow WW^*$ for large δ values.

The decay modes of the A bosons are: $A \rightarrow b\bar{b}$, $A \rightarrow hZ$, above the hZ threshold, and $A \rightarrow W^\pm H^\mp$, when kinematically allowed. In the region of very low δ values, below 10^{-3} rad, and if $m_A < M_Z + m_h$, the A total width is very small and A can leave the detector before decaying.

The excluded region at 95% confidence level in the (m_h, m_A) plane, at all δ values, are shown in Figure 7.2, for one solution of the 2HDM potential. Region I in this figure corresponds to the decay modes $h \rightarrow \gamma\gamma$ and $A \rightarrow b\bar{b}$ or A long-lived. Region II corresponds to $A \rightarrow hZ$ and $A \rightarrow h\gamma\gamma$. Region III corresponds to $h \rightarrow AA$ and $A \rightarrow b\bar{b}$. The band of low values of m_A and m_h masses is excluded by the Z invisible width measurement.

7.2 The Tevatron at Fermilab

The Tevatron collider at the Fermi National Accelerator Laboratory near Chicago, is a proton antiproton collider. Two general purpose detectors, called CDF and D0, are collecting data at this machine.

During run I of the Tevatron in 1992-1996 the D0 detector collected about 100 pb^{-1} of data at $\sqrt{s} = 1.8 \text{ TeV}$. These data were searched for a bosonic Higgs having standard model couplings to vector bosons but zero couplings to fermions in the $\gamma\gamma jj$ final state. For the Standard Model Higgs boson the main production process at the Tevatron is gluon-gluon fusion via a top quark loop. Because of the absence of Higgs-fermion couplings, it will not be possible to produce the fermiophobic Higgs by gluon fusion, and neither in associations with top pairs. Therefore two processes remain, the associated production with vector bosons [138], where an off-mass-shell W or Z boson is produced and radiates a Higgs boson, Figure 7.3, and vector boson fusion [89] with the latter giving less number of events [46].

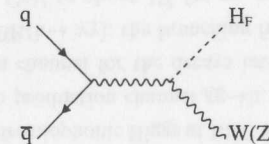


Figure 7.3: The main production mechanism of a fermiophobic Higgs at the Tevatron.

The D0 collaboration found four candidates which passed the selection requirements, with an expected background of 6.0 ± 2.1 events. In summary, the existence of a

fermiophobic Higgs boson was excluded by the D0 data at 95% confidence level up to a mass of 81.4 GeV [139], assuming Standard Model couplings between the Higgs and the vector bosons. Their result is shown in Figure 7.4.

Run IIa of the Tevatron is currently under way. During this run the D0 detector will collect approximately 2 fb^{-1} of data at $\sqrt{s} = 2 \text{ TeV}$. Landsberg and Matchev [140] have evaluated the prospects for detecting a non-standard light Higgs boson with a significant branching fraction into two photons, in the Run II of the Tevatron. The expected Run II limits on the branching fraction $h \rightarrow \gamma\gamma$ as a function of the Higgs mass are presented in Figure 7.5. As seen from this figure, the reach for a fermiophobic Higgs is about 115 GeV in Run IIa and about 125 GeV in Run IIb. This is an improvement over the final reach from LEP of 108 GeV. This study suggests that a signal of two photons combined with a jet or two jets is an effective method to search for a Higgs boson in the two photon decay mode at the Tevatron.

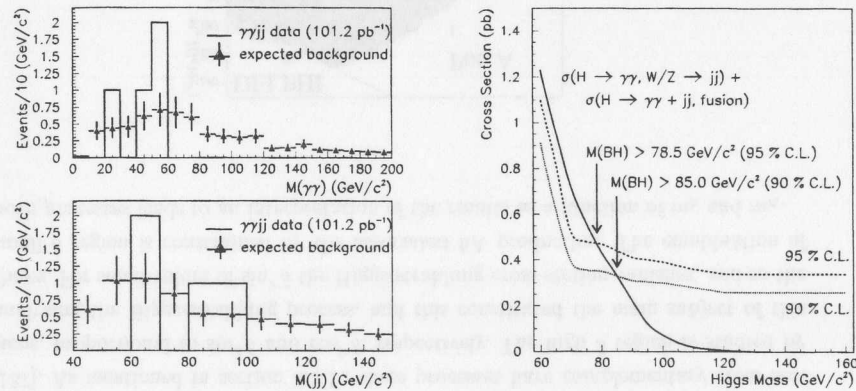


Figure 7.4: D0 results on the fermiophobic Higgs search. Graph on the left: The data and expected background for (up) the di-photon mass and (down) the di-jet mass distributions. Graph on the right: 95% confidence level cross section upper limits, dashed curve; the dotted curve represents the 90% confidence level exclusion contour, and the solid curve represents the bosonic Higgs cross section with $h \rightarrow \gamma\gamma$ and $W/Z \rightarrow jj$ branching fractions taken into account.

7.3 The Large Hadron Collider at CERN

The Large Hadron Collider (LHC) is a proton proton accelerator that is presently being built at CERN. The new collider will have a centre-of-mass energy of 14 TeV and the first particle collisions are scheduled to take place around 2007. Two general purpose detectors are being constructed at the LHC, ATLAS and CMS.

The phenomenology of a fermiophobic Higgs at LHC was studied by Akeroyd in Ref. [141]. Such a particle has no production channel $gg \rightarrow h$, but would give a clear signal in the associated production channel for the decays into two photons. It can have a sizeable branching fraction $\text{BR}(h \rightarrow \gamma\gamma)$: the branching fraction for these decays varies between 20% for $m_h = 100 \text{ GeV}$ to about 1% for $m_h = 130 \text{ GeV}$. At higher masses, there will be little difference between the signal for the Standard Model Higgs and the signal for the fermiophobic Higgs. It follows that the discovery of the fermiophobic Higgs will be very difficult in this channel for $m_h > 130 \text{ GeV}$.

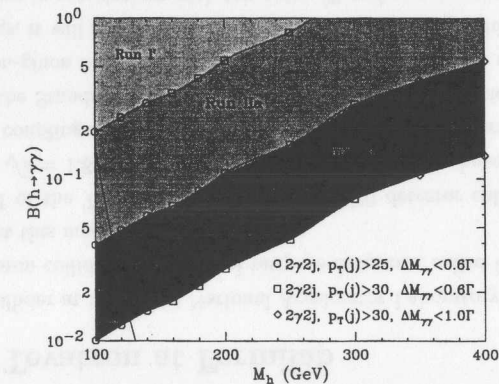


Figure 7.5: The predicted 95% confidence level limit on the branching fraction $h \rightarrow \gamma\gamma$, with 0.1, 2.0 and 30 fb^{-1} , as a function of the Higgs mass. The solid line is the prediction for the branching fraction of a bosonic Higgs.

Chapter 8

Conclusions

This thesis presents the results of the search for a Higgs boson decaying into two photons carried out with the data from e^+e^- interactions at centre-of-mass energies up to 209 GeV, collected by the L3 detector at LEP. At these energies the main Higgs production mechanism is the Higgs-Strahlung process, $e^+e^- \rightarrow hZ$. All the possible final states arising from the various decay modes of the Z boson have been analyzed. The main conclusion of this thesis is that no evidence of the production of a Higgs particle decaying into two photons is observed in the data. The negative search result is translated in upper limits on the branching fraction for the Higgs boson decay into two photons.

As a benchmark for exclusion of Higgs bosons in fermiophobic models, a scalar particle h is considered, produced in $e^+e^- \rightarrow hZ$ with Standard Model production cross section and with the partial width for $h \rightarrow \gamma\gamma$ given by the Standard Model, but with the fermionic coupling set to zero. Hence, assuming a Standard Model production rate, a lower limit on the mass of a fermiophobic Higgs is set at

$$m_h > 105.4 \text{ GeV at } 95\% \text{ confidence level,}$$

with a median limit expected from background only of $m_h^{\text{exp}} > 105.3 \text{ GeV}$. These numbers are the final L3 results for the fermiophobic Higgs search in the two photon decay mode, and are currently published [143]. They include the results at the lower centre-of-mass energy of 189 GeV published previously [142]. These results significantly improve the limits obtained at LEPI and exclude the benchmark fermiophobic model up to a mass of 105 GeV.

The results presented in this work are comparable to those obtained by the other three LEP experiments. They also do not observe an indication for the Higgs production and derive mass limits on a fermiophobic Higgs boson.

The combined data from all four LEP experiments are consistent with Standard Model backgrounds as well. The 95% confidence level lower limit from the combined

LEP searches on the fermiophobic Higgs mass is set at 108.2 GeV.

Unfortunately, at the end of the LEP2 program, the Higgs boson, the fundamental part of the electroweak theory, has not been found but stringent new limits have been established on its mass. In conclusion, since the Higgs boson appears to be heavier, its discovery will have to await the results of present experiments at Fermilab, or of the future experiments at the Large Hadron Collider at CERN.

Appendix A

Summary of the selection cuts

| Channel | Cut | 189 GeV | 192-202 GeV | 200-209 GeV | |
|---|----------------------------------|-------------------------|-------------|-------------|--------|
| hZ → $\gamma\gamma qq$ | N_{track} | > 6 | > 6 | > 6 | |
| | N_{cluster} | > 12 | > 15 | > 15 | |
| | E_{vis}/\sqrt{s} | > 0.5 | > 0.5 | > 0.5 | |
| | $ E_{\parallel} /E_{\text{vis}}$ | < 0.4 | < 0.4 | < 0.4 | |
| | $ E_{\perp} /E_{\text{vis}}$ | < 0.4 | < 0.4 | < 0.4 | |
| | $E_{30^\circ}/E_{\text{vis}}$ | < 0.5 | < 0.5 | < 0.5 | |
| | N_{γ} | > 1 | > 1 | > 1 | |
| | $E^{10^\circ, \gamma}$ | > 2.5 | > 1.5 | > 2.5 | |
| | $E^{20^\circ, \gamma}$ | > 4.5 | > 3.5 | > 4.5 | |
| | $\angle(\gamma, \gamma)$ [°] | > 50 | > 50 | > 50 | |
| | $\angle(\gamma, \text{jet})$ [°] | > 25 | > 25 | > 25 | |
| | E_{γ_1} [GeV] | > 10 | > 10 | > 10 | |
| | E_{γ_2} [GeV] | > 6 | > 6 | > 6 | |
| | $ \Delta M_{\text{recoil}} $ | < 10 | < 15 | < 15 | |
| | γ_{ID} | E_9/E_{25} | > 0.95 | > 0.95 | > 0.95 |
| | | E_{bump} [GeV] | > 1 | > 1 | > 1 |
| | | χ_{em}^2 | < 10 | < 10 | < 10 |
| $E_{\text{HCAL}}/E_{\text{bump}}$ | | < 0.2 | < 0.2 | < 0.2 | |
| $ \phi_{\text{BGO}} - \phi_{\text{TEC}} $ [rad] | | > 0.05 | > 0.05 | > 0.05 | |

Table A.1: The selection cuts used in the analysis.

| Channel | Cut | 189 GeV | 192-202 GeV | 200-209 GeV |
|---------------------------|---|----------|-------------|-------------|
| hZ → $\gamma\gamma\mu\mu$ | N_{track} | < 1 | < 1 | < 1 |
| | N_{cluster} | < 6 | < 6 | > 6 |
| | $E_{\text{vis}} - E_{\gamma}$ [GeV] | < 10 | < 10 | < 10 |
| | E_{HCAL} [GeV] | < 20 | < 20 | < 20 |
| | E_{LUMI} [GeV] | < 10 | < 10 | < 10 |
| | E_{ALR} [GeV] | < 10 | < 10 | < 10 |
| | E_{SPACAL} [GeV] | < 7 | < 7 | < 7 |
| | N_{μ} | < 1 | < 1 | < 1 |
| | N_{scint} | ≥ 1 | ≥ 1 | ≥ 1 |
| | N_{γ} | > 1 | > 1 | > 1 |
| | $\angle(\gamma, \gamma)$ [°] | > 50 | > 50 | > 50 |
| | acoplanarity [°] | > 3 | > 3 | > 3 |
| | $ p_{\perp} $ [GeV] | > 2 | > 2 | > 2 |
| | $\cos\theta_{\text{miss}}$ | > 0.966 | > 0.966 | > 0.966 |
| | E_{γ_1} [GeV] | > 10 | > 10 | > 10 |
| | E_{γ_2} [GeV] | > 6 | > 6 | > 6 |
| | $ \Delta M_{\text{recoil}} $ | < 10 | < 15 | < 15 |
| γ_{ID} | E_9/E_{25} | > 0.95 | > 0.95 | > 0.95 |
| | E_{bump} [GeV] | > 1 | > 1 | > 1 |
| | χ_{em}^2 | < 10 | < 10 | < 10 |
| | $E_{\text{HCAL}}/E_{\text{bump}}$ | < 0.2 | < 0.2 | < 0.2 |
| | $ \phi_{\text{BGO}} - \phi_{\text{TEC}} $ [rad] | > 0.05 | > 0.05 | > 0.05 |

Table A.2: The selection cuts used in the analysis.

| Channel | Cut | 189 GeV | 192-202 GeV | 200-209 GeV |
|---|---|--------------|-------------|-------------|
| $hZ \rightarrow \gamma\gamma e^+e^-$ | N_{track} | < 6 | < 6 | < 6 |
| | N_{cluster} | < 15 | < 15 | < 15 |
| | E_{vis}/\sqrt{s} | > 0.2 | > 0.2 | > 0.2 |
| | N_γ | > 1 | > 1 | > 1 |
| | $\angle(\gamma, \gamma)$ [°] | > 50 | > 50 | > 50 |
| | $\angle(\gamma, \text{electron})$ | > 25 | > 25 | > 25 |
| | [°] | | | |
| | $E^{20^\circ, \gamma}$ | > 4.5 | > 4.5 | > 4.5 |
| | N_e | > 0 | > 0 | > 0 |
| | E_e [GeV] | < 80 | < 80 | < 80 |
| | E_{γ_1} [GeV] | > 10 | > 10 | > 10 |
| | E_{γ_2} [GeV] | > 6 | > 6 | > 6 |
| | $ \Delta M_{\text{recoil}} $ | < 10 | < 15 | < 15 |
| | γ_{ID} | E_9/E_{25} | > 0.95 | > 0.95 |
| E_{bump} [GeV] | | > 1 | > 1 | > 1 |
| χ_{em}^2 | | < 10 | < 10 | < 10 |
| $E_{\text{HCAL}}/E_{\text{bump}}$ | | < 0.2 | < 0.2 | < 0.2 |
| $ \phi_{\text{BGO}} - \phi_{\text{TEC}} $ | | > 0.05 | > 0.05 | > 0.05 |
| [rad] | | | | |
| e_{ID} | E_9/E_{25} | > 0.95 | > 0.95 | > 0.95 |
| | E_{bump} [GeV] | > 3 | > 3 | > 3 |
| | χ_{em}^2 | < 10 | < 10 | < 10 |
| | $E_{\text{HCAL}}/E_{\text{bump}}$ | < 0.2 | < 0.2 | < 0.2 |
| | $ \phi_{\text{BGO}} - \phi_{\text{TEC}} $ | < 0.05 | < 0.05 | < 0.05 |
| [rad] | | | | |

Table A.3: The selection cuts used in the analysis.

| Channel | Cut | 189 GeV | 192-202 GeV | 200-209 GeV | |
|---|---|-------------------------|-------------|-------------|--------|
| $hZ \rightarrow \gamma\gamma\mu^+\mu^-$ | N_{track} | < 6 | < 6 | < 6 | |
| | N_{cluster} | < 15 | < 15 | < 15 | |
| | E_{vis}/\sqrt{s} | > 0.2 | > 0.2 | > 0.2 | |
| | N_γ | > 1 | > 1 | > 1 | |
| | $\angle(\gamma, \gamma)$ [°] | > 50 | > 50 | > 50 | |
| | $\angle(\gamma, \text{muon})$ [°] | > 25 | > 25 | > 25 | |
| | $E^{20^\circ, \gamma}$ | > 4.5 | > 4.5 | > 4.5 | |
| | N_μ | > 0 | > 0 | > 0 | |
| | E_μ [GeV] | < 80 | < 80 | < 80 | |
| | E_{γ_1} [GeV] | > 10 | > 10 | > 10 | |
| | E_{γ_2} [GeV] | > 6 | > 6 | > 6 | |
| | $ \Delta M_{\text{recoil}} $ | < 10 | < 15 | < 15 | |
| | γ_{ID} | E_9/E_{25} | > 0.95 | > 0.95 | > 0.95 |
| | | E_{bump} [GeV] | > 1 | > 1 | > 1 |
| χ_{em}^2 | | < 10 | < 10 | < 10 | |
| $E_{\text{HCAL}}/E_{\text{bump}}$ | | < 0.2 | < 0.2 | < 0.2 | |
| $ \phi_{\text{BGO}} - \phi_{\text{TEC}} $ | | > 0.05 | > 0.05 | > 0.05 | |
| [rad] | | | | | |
| μ_{ID} | $\text{DCA}_{\text{trans}}$ [mm] | < 300 | < 300 | < 300 | |
| | DCA_{long} [mm] | < 400 | < 400 | < 400 | |
| | $N_{\text{F}_{\text{seg}}} + N_{\text{F}_{\text{seg}}}$ | ≥ 2 | ≥ 2 | ≥ 2 | |
| | P_μ [GeV] | > 3 | > 3 | > 3 | |

Table A.4: The selection cuts used in the analysis.

| Channel | Cut | 189 GeV | 192-202 GeV | 200-209 GeV | |
|---|--|-----------------------------------|-------------|-------------|--------|
| hZ → $\gamma\gamma\tau^+\tau^-$ | N_{track} | < 6 | < 6 | < 6 | |
| | N_{cluster} | < 15 | < 15 | < 15 | |
| | E_{vis}/\sqrt{s} | > 0.2 | > 0.2 | > 0.2 | |
| | N_γ | > 1 | > 1 | > 1 | |
| | $\angle(\gamma, \gamma)$ [°] | > 50 | > 50 | > 50 | |
| | $\angle(\gamma, \text{tau})$ [°] | > 25 | > 25 | > 25 | |
| | $E^{20^\circ, \gamma}$ | > 4.5 | > 4.5 | > 4.5 | |
| | N_τ | > 0 | > 0 | > 0 | |
| | E_τ [GeV] | < 80 | < 80 | < 80 | |
| | E_{γ_1} [GeV] | > 10 | > 10 | > 10 | |
| | E_{γ_2} [GeV] | > 6 | > 6 | > 6 | |
| | $ \Delta M_{\text{recoil}} $ | < 10 | < 15 | < 15 | |
| | γ_{ID} | E_9/E_{25} | > 0.95 | > 0.95 | > 0.95 |
| | | E_{bump} [GeV] | > 1 | > 1 | > 1 |
| | | χ_{em}^2 | < 10 | < 10 | < 10 |
| | | $E_{\text{HCAL}}/E_{\text{bump}}$ | < 0.2 | < 0.2 | < 0.2 |
| $ \phi_{\text{BGO}} - \phi_{\text{TEC}} $ | | > 0.05 | > 0.05 | > 0.05 | |
| [rad] | | | | | |
| τ_{ID} | $N_{\text{Track}}^{10^\circ}$ | 1 - 3 | 1 - 3 | 1 - 3 | |
| | $\frac{E_{\text{Track}}^{10^\circ-30^\circ}}{E_{\text{Track}}^{0^\circ-10^\circ}}$ | < 0.3 | < 0.3 | < 0.3 | |
| | E_τ | > 3 | > 3 | > 3 | |

Table A.5: The selection cuts used in the analysis.

Appendix B

Results at the centre-of-mass energy of $\sqrt{s} = 189$ GeV

The selection of the data collected at the lower centre-of-mass energy $\sqrt{s} = 189$ GeV [142] follows similar criteria to the ones described in chapter 6, with the exception that for the leptonic channel we require two identified leptons in the event. The cut on the di-lepton invariant mass replaces the cut on the recoil mass against the photons. The number of events selected in data and expected from background processes is presented in Table B.1 for the hadronic channel, in Table B.2 for the neutrino channel and in Table B.3 for the leptonic channel. The reconstructed di-photon invariant mass is shown in Figure B.1 for all Z final states combined. Figure B.2 shows the measured upper limits on the BR(h → $\gamma\gamma$) as a function of the Higgs mass assuming a Standard Model rate for the Zh production, along with the expected limits as calculated from a large sample of Monte Carlo experiments. The theoretical prediction is also shown for a fermiophobic Higgs boson as calculated with the HDECAY program. The observed limit for BR(h → $\gamma\gamma$) = 1 is 98 GeV. The lower limit on the mass of a fermiophobic Higgs boson is set at

$$M_h > 94.9 \text{ GeV at 95\% confidence level.}$$

The expected mass limit is 95.1 GeV.

| | Data | Σ Bkg. | $q\bar{q}(\gamma)$ | WW | Ze^+e^- | ZZ |
|--------------|------|---------------|--------------------|--------|-----------|-------|
| Preselection | 8146 | 8221.7 | 5745.9 | 2309.8 | 58.2 | 109.8 |
| Selection | 10 | 16.2 | 16.0 | 0.0 | 0.1 | 0.1 |

Table B.1: Number of events expected from Standard Model processes compared to the observed number of events, after the preselection and selection steps, for the $q\bar{q}\gamma\gamma$ final state.

| | Data | $\nu\bar{\nu}(\gamma)$ |
|-----------|------|------------------------|
| Selection | 3 | 4.3 |

Table B.2: Number of events expected from the Standard Model process $e^+e^- \rightarrow \nu\bar{\nu}(\gamma)$ compared to the observed number of events, for the $\nu\bar{\nu}\gamma\gamma$ final state.

| | Data | Σ Bkg. | $e^+e^-(\gamma)$ | $\mu^+\mu^-(\gamma)$ | $\tau^+\tau^-(\gamma)$ | 4 fermion |
|--------------|------|---------------|------------------|----------------------|------------------------|-----------|
| Preselection | 86 | 93.8 | 66.4 | 14.1 | 9.9 | 3.4 |
| Selection | 5 | 2.5 | 1.1 | 0.7 | 0.7 | 0.0 |

Table B.3: Number of events expected from Standard Model processes compared to the observed number of events, after the preselection and selection steps, for the $\ell^+\ell^-\gamma\gamma$ final state.

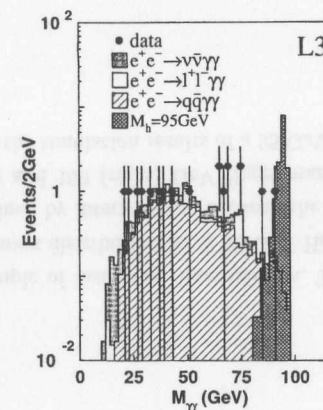


Figure B.1: The distribution of the reconstructed di-photon invariant mass for all Z final states combined, after the final selection, in data at $\sqrt{s} = 189$ GeV, background and for a Higgs boson signal with the mass $M_h = 95$ GeV. The signal, assuming a Standard Model cross section and a $BR(h \rightarrow \gamma\gamma) = 1$, is superimposed and normalized to the integrated luminosity.

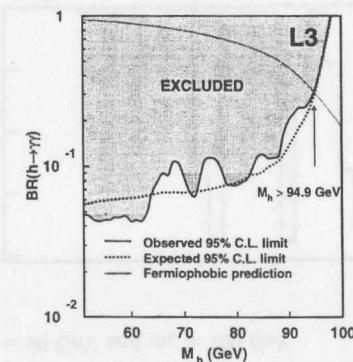


Figure B.2: Excluded values of the $BR(h \rightarrow \gamma\gamma)$ as a function of the Higgs mass, with the assumption of a Standard Model production cross section, for 189 GeV data. The expected 95% confidence level limit and the theoretical prediction are also presented.

Appendix C

Linear interpolation of histograms

The method proposed by A.L. Read in Ref. [130] is based on the linear interpolation of the inverses of the cumulative distribution functions. The cumulative distribution functions of two distribution functions $f_1(x)$ and $f_2(x)$ for the observable x are:

$$F_{1,2}(x) = \int_{-\infty}^x f_{1,2}(x') dx'.$$

The goal is to obtain a new probability distribution function $\bar{f}(x)$ with the corresponding cumulative distribution function

$$\bar{F}(x) = \int_{-\infty}^x \bar{f}(x') dx'.$$

The first step of the interpolation procedure is to find x_1 and x_2 where the cumulative distributions F_1 and F_2 are equal for a given cumulative probability y ,

$$F_1(x_1) = F_2(x_2) = y. \quad (\text{C.1})$$

The cumulative probability for the new distribution \bar{F} is set to the same value y at a linearly interpolated position x ,

$$\bar{F}(x) = y, \quad (\text{C.2})$$

$$x = ax_1 + bx_2. \quad (\text{C.3})$$

The constants a and b express the interpolation distance between the extreme values of the relevant parameter for the two existing distributions and satisfy $a + b = 1$.

The probability distribution function $\bar{f}(x)$ is obtained by inverting the cumulative distributions in Eqs. (C.1) and (C.2), substituting these results in Eq. (C.3),

$$\bar{F}^{-1}(y) = aF_1^{-1}(y) + bF_2^{-1}(y),$$

deriving this with respect to y and solving for the interpolated probability distribution function $\bar{f}(x)$,

$$\bar{f}(x) = \frac{f_1(x_1)f_2(x_2)}{af_2(x_2) + bf_1(x_1)}.$$

Figure C.1 shows how well the interpolation procedure describes the reconstructed invariant mass distribution of a hypothetical Higgs boson with mass $m_h = 95$ GeV, decaying in the $Zh \rightarrow q\bar{q}\gamma\gamma$ channel at centre-of-mass energy of $\sqrt{s} = 206.6$ GeV based on simulations at $m_h = 90$ GeV and $m_h = 100$ GeV.

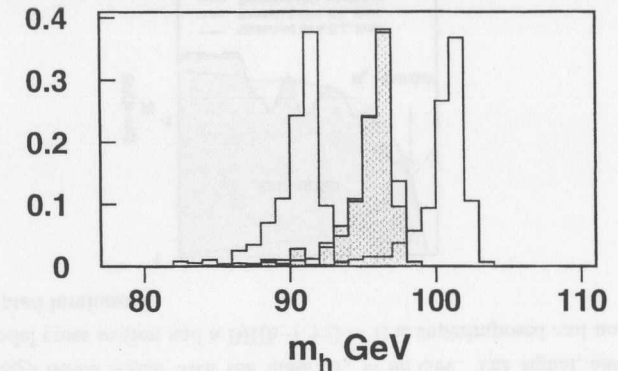


Figure C.1: Example of histogram interpolation. The reconstructed invariant mass distribution for a 95 GeV Higgs (solid line) has been obtained by interpolation between the simulation results for 90 (left) and 100 (right) GeV Higgs masses and is superimposed with the simulation results of a 95 GeV Higgs particle (middle).

Appendix D

Background smoothing

The parameterisation of discriminant variable distributions is a crucial step in the limit setting procedure. In the calculation of confidence levels using the likelihood ratio as an estimator, it is desirable to have continuous functions to parameterise the distributions of discriminating variables. In order to produce continuous estimates $\hat{f}(x)$ of the parent distribution from the empirical probability density function $f(x)$, several techniques have been developed. The basic idea of the KEYS program [129] is that it constructs a smooth shape by placing a Gaussian Kernel of probability at each event. By summing over these kernels a smooth shape is obtained. The performance of the smoothing program is presented in Figure D.1 and the standard output of the program is shown in Figure D.2.

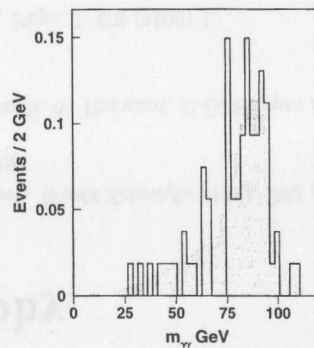


Figure D.1: The performance of the smoothing program on the reconstructed Higgs mass distribution: the line is the original distribution, and the shaded area is the smoothed histogram.

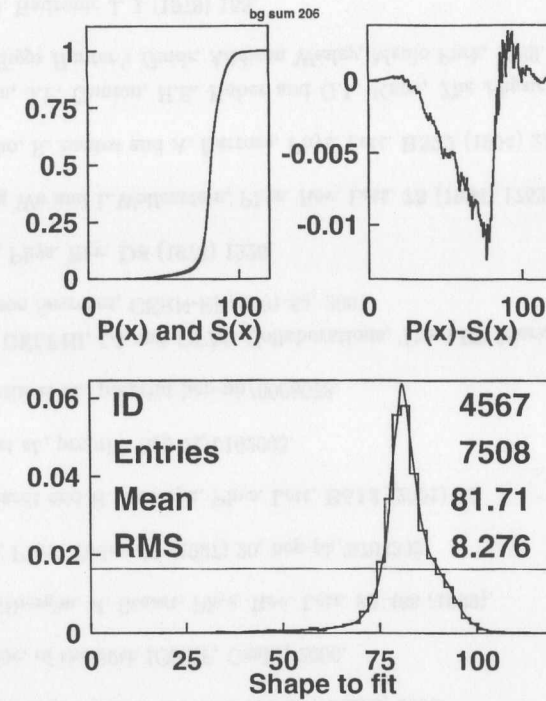


Figure D.2: The standard output of the KEYS program.

The top left plot shows the cumulative distribution of the KEYS shape and the data. The top right plot shows the difference between the two cumulative distributions, the maximum of which is used in the calculation of the Kolmogorov-Smirnov test. The bottom plot shows the shape produced by KEYS overlapped on a histogram of the original data.

Bibliography

- [1] G. 'tHooft, *Singapore, World Scientific (1994) 684 p. (Advanced Series in Mathematical Physics, 19).*
- [2] C.S. Wu, E. Ambler, R.W. Hayward, D.D. Hoppes and R.P. Hudson, *Phys. Rev.* **105** (1957) 1413.
- [3] C. Caso *et al.*, *Eur. Phys. J.* **C3** (1998) 1.
- [4] S.M. Berman and A. Srilin, *Ann. Phys. (NY)* **20** (1962) 20.
- [5] T. Kinoshita, *Phys. Rev. Lett.* **2** (1959) 477.
- [6] T. van Ritbergen and R. G. Stuart, *Phys. Rev. Lett.* **82** (1999) 488.
- [7] Particle Data Group, Review of Particle Physics, D.E. Groom *et al.*, *Eur. Phys. J.* **C15** (2000) 1; updates of the Review of Particle Physics are available on website: <http://pdg.lbl.gov>.
- [8] S.L. Glashow, *Nucl. Phys.* **B22** (1961) 22.
- [9] S. Weinberg, *Phys. Rev. Lett.* **19** (1967) 1264; A. Salam, Proc. 8th Nobel Symposium, (1968), ed. N. Svart.
- [10] G. 'tHooft, *Nucl. Phys.* **B33** (1971) 173.
- [11] G. 'tHooft, *Nucl. Phys.* **B35** (1971) 167.
- [12] P.W. Higgs, *Phys. Rev. Lett.* **13** (1964) 508.
- [13] F. Englert and R. Brout, *Phys. Rev. Lett.* **13** (1964) 321.
- [14] S. L. Glashow, J. Iliopoulos and L. Maiani, *Phys. Rev.* **D2** (1970) 1285.
- [15] N. Cabibbo, L. Maiani, G. Parisi and R. Petronzio, *Nucl. Phys.* **B158** (1979) 295; M. Lindner, *Z. Phys.* **C31** (1986) 295; M. Sher, *Phys. Rev.* **D179** (1989) 273; M. Lindner, M. Sher and H.W. Zaglauer, *Phys. Lett.* **B228** (1989) 139.
- [16] M. Sher, *Phys. Lett.* **B317** (1993) 159; C. Ford, D.R.T. Jones, P.W. Stephenson and M.B. Einhorn, *Nucl. Phys.* **B395** (1993) 17; G. Altarelli and I. Isidori, *Phys. Lett.* **B337** (1994) 141; J.A. Casas, J.R. Espinosa and M. Quiros, *Phys. Lett.* **B342** (1995) 171.
- [17] T. Hambye and K. Riesselmann, *Phys. Rev.* **D55** (1997) 7255; H. Dreiner, hep-ph/9902347.
- [18] J. Ellis and D. Ross, hep-ph/0012067.
- [19] B.W. Lee, C. Quigg and G.B. Thacker, *Phys. Rev. Lett.* **38** (1977) 883; *Phys. Rev.* **D16** (1977) 1519.
- [20] A. Gurtu, Proc. of the 30th ICHEP, Osaka, 2000.
- [21] LEP Electroweak Working Group, CERN-EP/2001-098; M. Grünewald, *Phys. Rep.* **322** (1999) 125-346.
- [22] D. Chakraborty, Proc. of the 30th ICHEP, Osaka, 2000.
- [23] J. Yu, Proc. of the 30th ICHEP, Osaka, 2000.
- [24] T. van Ritbergen, R. Stuart, *Phys. Rev. Lett.* **82** 488 (1999).
- [25] C. Quigg, *Phys. Today* **50** (1997) 20, hep-ph/9704332.
- [26] H. Burkhardt and B. Pietrzyk, *Phys. Lett.* **B513** (2001) 46.
- [27] J.Z. Bai *et al.*, preprint hep-ex/0102003.
- [28] A.D. Martin *et al.*, preprint hep-ph/0008078.
- [29] ALEPH, DELPHI, L3 and OPAL Collaborations, The LEP Working Group for Higgs Boson Searches, CERN-EP/2001-55, 2001.
- [30] T.D. Lee, *Phys. Rev.* **D8** (1973) 1226.
- [31] Yue-Liang Wu and L. Wolfenstein, *Phys. Rev. Lett.* **73** (1994) 1762.
- [32] J. Velhinho, R. Santos and A. Barroso, *Phys. Lett.* **B322** (1994) 213.
- [33] S. Dawson, J.F. Gunion, H.E. Haber and G.L. Kane, *The Physics of the Higgs Bosons: Higgs Hunter's Guide*, Addison Wesley, Menlo Park, 1989.
- [34] H. Georgi, *Hadronic J.* **1** (1978) 155.
- [35] J.A. Grifols and A. Mendez, *Phys. Rev.* **D22** (1980) 1725.

- [36] M. Sher, *Singapore, World Scientific (1993) 44 p. (Advanced Series on Directions in High Energy Physics, 13)*.
- [37] P. Ferrari and D. Zer-Zion, OPAL Collaboration, OPAL Phys. Note PN475, July, 2001; M. Bluj, M. Boonekamp, J. Hoffman and P. Zalewski, DELPHI Collaboration, DELPHI 2001-068 CONF 496, July, 2001.
- [38] L. Resnick, M.K. Sundareshan, P.J.S. Watson, Phys. Rev. **D8** (1973) 172.
- [39] E. Braaten, J.P. Leveille, Phys. Rev. **D22** (1980) 715; N. Sakai, Phys. Rev. **D22** (1980) 2220; T. Inami, T. Kubota, Nucl. Phys. **B179** (1981) 171; M. Drees, K. Hikasa, Phys. Lett. **B240** (1990) 455; S.G. Gorishny, A.L. Kataev, S.A. Larin and L.R. Surguladze, Mod. Phys. Lett. **5** (1990) 2703; A.L. Kataev, V.T. Kim, Mod. Phys. Lett. **A9** (1994) 1309; L.R. Surguladze, Phys. Lett. **B341** (1994) 61.
- [40] G. Altarelli, T. Sjöstrand, F. Zwirner, *Physics at LEP2*, CERN 96-01, Vol. 1.
- [41] M. Spira, A. Djouadi, D. Graudenz, P.M. Zerwas, Nucl. Phys. **B453** (1995) 17.
- [42] S. Dawson, J.F. Gunion, H.E. Haber and G.L. Kane, *The Physics of the Higgs Bosons: Higgs Hunter's Guide*, Addison Wesley, Menlo Park, 1989.
- [43] A. Djouadi, J. Kalinowski and M. Spira, Comp. Phys. Comm. **108** (1998) 56.
- [44] H.E. Haber, G.L. Kane and T. Sterling, Nucl. Phys. **B161** (1979) 493.
- [45] V. Barger, N.G. Deshpande, J.L. Hewett and T.G. Rizzo, preprint OITS-499, hep-ph/9211234; J.L. Basdevant, E.L. Berger, D. Dicus, C. Kao and S. Willenbrock, Phys. Lett. **B313** (1993) 402; A.G. Akeroyd, Phys. Lett. **B368** (1996) 89; A. Barroso, L. Brucher and R. Santos, Phys. Rev. **D60** (1999) 035005; L. Brucher and R. Santos, Eur. Phys. J. **C12** (2000) 87.
- [46] A. Stange, W. Marciano and S. Willenbrock, Phys. Rev. **D49** (1994) 1354.
- [47] J.F. Gunion, R. Vega and J. Wudka, Phys. Rev. **D42** (1990) 1673; P. Bamert and Z. Kunszt, Phys. Lett. **B306** (1993) 335.
- [48] A.G. Akeroyd, Phys. Lett. **B353** (1995) 519.
- [49] B. Dobrescu, preprint FERMILAB-PUB-99/234-T, hep-ph/9908391; B. Dobrescu, G. Landsberg and K. Matchev, preprint FERMILAB-PUB-99/324-T.
- [50] L. Hall and C. Kolda, Phys. Lett. **B459** (1999) 213; H. Cheng, B. Dobrescu and C. T. Hill, preprint FERMILAB-PUB-99/358-T, hep-ph/9912343.

- [51] M.C. Gonzalez-Garcia, S.M. Lietti and S.F. Novaes, Phys. Rev. **D57** (1998) 7045; M.C. Gonzalez-Garcia, Int. J. Mod. Phys. **A** (1999) 1, hep-ph/9902321.
- [52] R. Martinez, J.-Alexis Rodriguez and M. Vargas, hep-ph/0004135.
- [53] G. t'Hooft and M. Veltman, Nucl. Phys. **B153** (1979) 365; G. Passarino and M. Veltman, Nucl. Phys. **B160** (1979) 151.
- [54] H. Georgi and M. Machacek, Nucl. Phys. **B262** (1985) 463.
- [55] P. Bamert and Z. Kunszt, Phys. Lett. **B306** (1993) 335.
- [56] W. Buchmüller and D. Wyler, Nucl. Phys. **B268** (1986) 621; C.J.C. Burgess and H.J. Schnitzer, Nucl. Phys. **B228** (1983) 424; C.N. Leung, S.T. Love and S. Rao, Z. Phys. **C31** (1986) 433. A. de Rujula, M.B. Gavela, P. Hernandez and E. Masso, Nucl. Phys. **B384** (1992) 3.
- [57] S. Weinberg, Physica **A96** (1979) 327; H. Georgi, *Weak Interactions and Modern Particle Theory*, Benjamin/Cummings, Menlo Park, 1984.
- [58] K. Hagiwara, S. Ishihara, R. Szalapski and D. Zeppenfeld, Phys. Lett. **B283** (1992) 353; K. Hagiwara, S. Ishihara, R. Szalapski and D. Zeppenfeld, Phys. Rev. **D48** (1993) 2182.
- [59] K. Hagiwara, R. Szalapski and D. Zeppenfeld, Phys. Lett. **B318** (1993) 155.
- [60] K. Hagiwara and M.L. Stong, Z. Phys. **62** (1994) 99; B. Grzadowski and J. Wudka, Phys. Lett. **B364** (1995) 49; G.J. Gounaris, F.M. Renard and N.D. Vlachos, Nucl. Phys. **B459** (1996) 51; W. Killian, M. Krämer and P.M. Zerwas, Phys. Lett. **B381** (1996) 243; S.M. Lietti, S.F. Novaes and R. Rosenfeld, Phys. Rev. **D54** (1996) 3266.
- [61] F. de Campos, M.C. Gonzales-Garcia and S.F. Novaes, Phys. Rev. Lett. **79** (1997) 5213; F. de Campos, M.C. Gonzales-Garcia, S.M. Lietti, S.F. Novaes and R. Rosenfeld, Phys. Lett. **B435** (1998) 407.
- [62] G.J. Gounaris, J. Layssac and F.M. Renard, Z. Phys. **69** (1996) 505; G.J. Gounaris and F.M. Renard, Z. Phys. **69** (1996) 513.
- [63] M. Acciari *et al.*, Phys. Lett. **B489** (2000) 102.
- [64] J.D. Wells, Phys. Rev. **D56** (1997) 1504.
- [65] C.T. Hill, Phys. Lett. **B266** (1991) 419; C.T. Hill, Phys. Lett. **B345** (1995) 483.

- [66] P. Janot, "The HZHA generator", in "Physics at LEP2", Eds. G. Altarelli, T. Sjöstrand and F. Zwirner, CERN 96-01 (1996) Vol.2, 309.
- [67] M. Skrzypek, S. Jadach, W. Placzek and Z. Wąs, *Comp. Phys. Comm.* **94** (1996) 216; M. Skrzypek, S. Jadach, M. Martinez, W. Placzek and Z. Wąs, *Phys. Lett.* **B372** (1996) 289.
- [68] F.A. Berends, R. Kleiss and R. Pittau, *Nucl. Phys.* **B424** (1994) 308; *Nucl. Phys.* **B426** (1994) 344; *Nucl. Phys. (Proc. Suppl.)* **B37** (1994) 163; R. Kleiss and R. Pittau, *Comp. Phys. Comm.* **83** (1994) 141; R. Pittau, *Phys. Lett.* **B335** (1994) 490.
- [69] G. Marchesini and B. Webber, *Nucl. Phys.* **B310** (1988) 461; I.G. Knowles, *Nucl. Phys.* **B310** (1988) 571; G. Marchesini *et al.*, *Comp. Phys. Comm.* **67** (1992) 465.
- [70] G. Montagna, O. Nicosini and F. Piccinini, *Comp. Phys. Comm.* **98** (1996) 206.
- [71] G. Montagna, M. Moretti, O. Nicosini and F. Piccinini, *Nucl. Phys.* **B541** (1999) 31.
- [72] S. Jadach, B.F.L. Ward and Z. Wąs, *Comp. Phys. Comm.* **79** (1994) 503.
- [73] S. Jadach, B.F.L. Ward and Z. Wąs, Preprint hep-ph/9912214.
- [74] T. Sjöstrand, CERN-TH/7112/93 (1993), revised August 1995; T. Sjöstrand, *Comp. Phys. Comm.* **82** (1994) 74.
- [75] R. Engel, *Z. Phys. C* **66** (1995) 203; R. Engel, J. Ranft and S. Roesler, *Phys. Rev. D* **52** (1995) 1459.
- [76] F.A. Berends, P.H. Daverfeldt and R. Kleiss, *Nucl. Phys. B* **253** (1985) 441.
- [77] J.A.M. Vermaseren, J. Smith and G. Grammer Jr., *Phys. Rev. D* **19** (1979) 137; J.A.M. Vermaseren, *Nucl. Phys. B* **229** (1983) 347.
- [78] S. Jadach *et al.*, *Phys. Lett. B* **390** (1997) 298.
- [79] D. Karlen, *Nucl. Phys. B* **289** (1987) 23.
- [80] F.A. Berends, R. Pittau and R. Kleiss, *Comp. Phys. Comm.* **85** (1995) 437.
- [81] M. Acciarri *et al.*, *Phys. Lett. B* **479** (2000) 101.
- [82] M. Acciarri *et al.*, *Phys. Lett. B* **519** (2001) 33; M. Acciarri *et al.*, CERN-EP/2001-073, Preprint hep-ex/0111012 (2001).

- [83] M. Acciarri *et al.*, *Phys. Lett. B* **496** (2000) 19.
- [84] M. Acciarri *et al.*, *Phys. Lett. B* **497** (2001) 23.
- [85] M. Acciarri *et al.*, *Phys. Lett. B* **487** (2000) 229.
- [86] J. Ellis, M.K. Gaillard and D.V. Nanopoulos, *Nucl. Phys.* **B106** (1976) 292; B.L. Ioffe and V.A. Khoze, *Sov. J. Part. Nucl.* **9** (1978) 50; B.W. Lee, C. Quigg and H.B. Thacker, *Phys. Rev. D* **16** (1977) 1519.
- [87] V. Barger, K. Cheung, A. Djouadi, B.A. Kniehl and P. Zerwas, *Phys. Rev. D* **49** (1994) 79.
- [88] D.R.T. Jones and S.T. Petcov, *Phys. Lett. B* **84** (1979) 440.
- [89] R.N. Cahn and S. Dawson, *Phys. Lett. B* **136** (1984) 96.
- [90] G.L. Kane, W.W. Repko and W.B. Rolnick, *Phys. Lett. B* **148** (1984) 367.
- [91] G. Altarelli, B. Mele and F. Pitolli, *Nucl. Phys.* **B287** (1987) 205; W. Kilian, M. Krämer and P.M. Zerwas, *Phys. Lett. B* **373** (1996) 135.
- [92] G. Altarelli, T. Sjöstrand and F. Zwirner, *Physics at LEP2*, CERN 96-01, Vol. 1.
- [93] S. Komamiya, *Phys. Rev. D* **38** (1988) 2158.
- [94] LEP Design Report, vol.1, CERN-LEP/TH/83-29 (1983); LEP Design Report, vol.2, CERN-LEP 84-01 (1984); LEP Design Report, vol.3, CERN-AC 96-01 (1996).
- [95] L. Arnaudon, *Phys. Lett. B* **284** (1992) 431.
- [96] V. Bargmann, L. Michel and V.L. Telegdi, *Phys. Rev. Lett.* **10** (1959) 435.
- [97] A.A. Sokolov and I.M. Ternov, *Phys. Dokl.* **8** (1964) 1203.
- [98] A. Drees, *High Precision Measurements of the LEP Center-of-Mass Energies during 1993 and 1995 Z Resonance Scans*, Dissertation Wuppertal WUB-DIS 97-5.
- [99] B. Adeva *et al.*, *Nucl. Instr. and Meth. A* **289** (1990) 35.
- [100] M. Acciarri *et al.*, *Nucl. Instr. and Meth. A* **351** (1994) 300.
- [101] B. Beissel *et al.*, *Nucl. Instr. and Meth. A* **332** (1993) 33.
- [102] K. Deiters *et al.*, *Nucl. Instr. and Meth. A* **323** (1992) 162.
- [103] G. Alkhozov *et al.*, L3 note 1862 (1995). D. Prokofiev *et al.*, L3 note 1895 (1995).

- [104] B. Adeva *et al.*, Nucl. Instr. and Meth. **A265** (1988) 252.
- [105] L3 BGO Collaboration, L3 Note 1712 (1995).
- [106] G. Basti *et al.*, Nucl. Instr. and Meth. **A374** (1996) 293.
- [107] I.C. Brock *et al.*, Nucl. Instr. and Meth. **A381** (1996) 236.
- [108] O. Adriani *et al.*, Nucl. Instr. and Meth. **A302** (1991) 53.
- [109] U. Uwer, L3 note 1400 (1993); L3 note 2003 (1996).
- [110] G. Chiefari *et al.*, Nucl. Instr. and Meth. **A277** (1989) 187; S. Lanzano *et al.*, Nucl. Instr. and Meth. **A289** (1990) 335; A. Adam *et al.*, Nucl. Instr. and Meth. **A383** (1996) 342.
- [111] The L3 Forward-Backward Muon Group, L3 Note 1984 (1996).
- [112] P. Bene *et al.*, Nucl. Instr. and Meth. **A306** (1991) 150; Y. Bertsch *et al.*, Nucl. Instr. and Meth. **A340** (1994) 309; C. Dionisi *et al.*, Nucl. Instr. and Meth. **A336** (1993) 78.
- [113] R. Bizzarri *et al.*, Nucl. Instr. and Meth. **A283** (1989) 799; R. Bizzarri *et al.*, Nucl. Instr. and Meth. **A317** (1992) 463; R. Bagnaia, R. Bizzarri, F. Cesaroni, S. Gentile and G. Lunadei, Nucl. Instr. and Meth. **A323** (1992) 528; R. Bagnaia, R. Bizzarri, F. Cesaroni, S. Gentile and T. Hebbeker, Nucl. Instr. and Meth. **A324** (1993) 101.
- [114] P. Bene *et al.*, Nucl. Instr. and Meth. **A306** (1991) 150.
- [115] T. Dai and M. Fukushima, L3 note 669 (1989).
- [116] G. Carlino *et al.*, L3 note 1951 (1996).
- [117] S.P. Beingsner *et al.*, Nucl. Instr. and Meth. **A340** (1994) 322.
- [118] C. Dionisi *et al.*, Nucl. Instr. and Meth. **A336** (1993) 78.
- [119] R. Brun *et al.*, Preprint CERN DD/EE/84-1, (1984), revised 1987.
- [120] CN/ASD Group and J. Zoll/ECP., Zebra Users Guide, Program Library Q100, CERN, 1993.
- [121] H. Fesefeldt, RWTH Aachen Report PITHA 85/02 (1985).
- [122] S. Banerjee and F. Bruyant, L3 Note 748 (1990); J. Swain and L. Taylor, preprint NUB-3065, Northeastern University Boston (1993).

- [123] W. Bartel *et al.*, Z. Phys. **C33** (1986) 235; S. Bethke *et al.*, Phys. Lett. **B213** (1988) 235.
- [124] T. Sjöstrand, Comp. Phys. Comm. **28** (1983) 227.
- [125] S. Catani, Yu.L. Dokshitzer, M. Olsom, G. Turnock and B.R. Webber, Phys. Lett. **B269** (1991) 432; S. Bethke *et al.*, Nucl. Phys. **B 370** (1992) 310 and references therein.
- [126] H.J. Daum *et al.*, Z. Phys. **C8** (1981) 167.
- [127] S. Brandt, Ch. Peyron, R. Sosnowski and A. Wroblewski, Phys. Lett. **12** (1964) 57; E. Falvi, Phys. Rev. Lett. **39** (1977) 1587.
- [128] V.F. Obraztsov, Nucl. Instr. and Meth. **A316** (1992) 388.
- [129] K.S. Cranmer, ALEPH 99-144 PHYSIC 99-056 (1999).
- [130] A.L. Read, Nucl. Instr. and Meth. **A425** (1999) 357.
- [131] O. Adriani *et al.*, Phys. Lett. **B292** (1992) 472; M. Acciarri *et al.*, Phys. Lett. **B388** (1996) 409.
- [132] J. Mans, talk presented at Seventh Topical Seminar on the Legacy of LEP and SLC, Siena, October, 2001.
- [133] D. Decamp *et al.*, Nucl. Instr. and Meth. **A294** (1990) 127.
- [134] P. Aarnio *et al.*, Nucl. Instr. and Meth. **A303** (1991) 233.
- [135] K. Ahmet *et al.*, Nucl. Instr. and Meth. **A305** (1991) 275.
- [136] ALEPH, DELPHI, L3 and OPAL Collaborations, The LEP Higgs Working Group, LHWG Note 2001-08, Preprint hep-ex/0107035 (2001).
- [137] DELPHI Collaboration, DELPHI 2000-082 CONF 381, July, 2000.
- [138] S.L. Glashow, D.V. Nanopoulos and A. Yildiz, Phys. Rev. **D18** (1978) 1724.
- [139] B. Abbott *et al.*, Phys. Rev. Lett. **82** (1999) 2244.
- [140] G. Landsberg and K.T. Matchev, FERMILAB-PUB-00/003-T, hep-ex/0001007.
- [141] A.G. Akeroyd, J. Phys. **G24** (1998) 1983.
- [142] A. Rosca, L3 Note 2595 (2000); M. Acciarri *et al.*, Phys. Lett. **B489** (2000) 115.
- [143] A. Rosca, L3 Note 2673 (2001); Preprint CERN-EP/2002-010; P. Achard *et al.*, accepted for publication in Phys. Lett. **B**.

Acknowledgments

I would like to thank my advisor Prof. Thomas Hebbeker for giving me the opportunity to work on this interesting subject. He provided me with the freedom I needed to achieve the results presented here, and in the same time he gave me his support whenever necessary. I have profited a lot from his experience and helpful discussions.

I am grateful to Marta Felcini for a pleasant collaboration and her patience in answering my questions. I would also like to express my gratitude to all my colleagues from the Higgs group, in particular to Pablo Garcia-Abia, Juan Alcaraz, Ghita Rahal-Callot, Andre Holzner, Wolfgang Lohmann and Chris Tully.

A special thank you to my colleagues from the L3 DESY Zeuthen group who always offered me pleasant working environment when I came to Zeuthen as a guest.

Lebenslauf

| | |
|-------------|---|
| Name: | Aura Rosca |
| 1985 - 1989 | Studium Universität Bukarest |
| 1989 - 1991 | Lehrerin Gymnasium |
| 1991 - 1993 | Wissenschaftliche Mitarbeiterin an IFIN-HH, Bukarest |
| 1994 - 1997 | Fellow INFN-LNF, Frascati |
| 1998 - 2001 | Wissenschaftliche Mitarbeiterin an der Humboldt-Universität zu Berlin, Prof. Hebbeker, Institut für Physik |

Erklärung

Hiermit erkläre ich, die Dissertation selbständig und ohne unerlaubte Hilfe angefertigt zu haben.

Ich habe mich anderwärts nicht um einen Doktorgrad beworben und besitze einen entsprechenden Doktorgrad nicht.

Ich erkläre die Kenntnisnahme der dem Verfahren zugrunde liegende Promotionsordnung der Mathematisch-Naturwissenschaftlichen Fakultät I der Humboldt-Universität zu Berlin.

Aura Rosca

Ученый

М. П.

Всего в документе содержится 10 страниц. В документе содержится информация о деятельности организации за период с 1 января 2000 года по 31 декабря 2000 года. В документе содержится информация о деятельности организации за период с 1 января 2001 года по 31 декабря 2001 года. В документе содержится информация о деятельности организации за период с 1 января 2002 года по 31 декабря 2002 года.

Всего в документе содержится 10 страниц. В документе содержится информация о деятельности организации за период с 1 января 2000 года по 31 декабря 2000 года.

Всего в документе содержится 10 страниц.